Development of metal oxide-based gas sensors for the detection of biomarkers in rice aging

Jinyong Xu

THESE DE DOCTORAT DE L'ETABLISSEMENT UNIVERSITE BOURGOGNE FRANCHE-COMTE PREPAREE A l'UNIVERSITE DE TECHNOLOGIE DE BELFORT-MONTBELIARD

Ecole doctorale n^{o} 37

Sciences Physiques pour l'Ingénieur et Microtechniques - SPIM

Doctorat de Sciences pour l'Ingénieur

Par

Mr. XU Jinyong

Development of Metal Oxide-based Gas Sensors for the Detection of Biomarkers in Rice Aging

Thèse présentée et soutenue à UTBM Site de Sévenans, le 23 mai 2024

Composition du Jury :

Mr. SCHNEIDER Raphaël	Professeur, Université de Lorraine	Rapporteur
Mr. TULLIANI Jean-Marc	Professeur, Politecnico di Torino	Rapporteur
Mr. GROSDIDIER Thierry	Professeur, Université de Lorraine	Examinateur (Président)
Ms. TOMA Filofteia-Laura	Engineer Scientist, Fraunhofer Institute for Materials and Beam technology IWS	Examinatrice
Mr. DENG Sihao	Maitre de conférences-HDR, UTBM	Directeur de thèse
Mr. LIAO Hanlin	Professeur, UTBM	Codirecteur de thèse
Mr. ZHANG Chao	Professeur, Yangzhou University	Codirecteur de thèse

Acknowledgements

My PhD thesis was carried out at the University of Technology of Belfort-Montbéliard (UTBM), in collaboration with Yangzhou University, with the financial support from the China Scholarship Council (CSC).

First and foremost, I would like to express my gratitude to the president and all members of the defense committee. Specific thanks to Prof. Raphaël Schneider and Prof. Jean-Marc Tulliani for their patience and time in reviewing my thesis and providing invaluable comments that are highly beneficial for my future research. I sincerely appreciate their efforts.

I extend my heartfelt thanks to my director, Dr. Sihao Deng, and co-directors, Prof. Hanlin Liao and Chao Zhang, for their immense help and encouragement throughout my PhD journey. I am especially grateful to Prof. Hanlin Liao for his unwavering support, guidance, and encouragement during my work and life in France. It has been an honor to work with such esteemed individuals.

Many thanks to the members of our ICB-LERMPS laboratory: Mr. Zhoukun Shi, Mr. Wenbo Li, Mrs. Xinge Jiang, Mr. Yingjie Li, and others, for their assistance with my PhD work. I also extend my gratitude to Mr. Kaichun Xu and Mr. Xiaoxi He at Yangzhou University for their help and support in gas-sensing investigations and theoretical simulations of the developed metal oxides.

Finally, I would like to thank my beloved family for their unwavering support and concern. Without their encouragement, support, and love, I would not have successfully completed my PhD.

General Introduction

For a long time, the storage of cereals like rice has been a strategic task to ensure the food supply. However, rice is one of the most challenging grains to store. Typically, stored at room temperature for six months to one year or at high temperature (>50 ℃) for 1-3 months, rice undergoes an aging process, leading to its quality deterioration. After aging, several macroscopic characteristics of rice are changed. For example, in terms of color, the surface luster of aged rice gradually decreases and becomes darker. With the aging process, unpleasant odors are generated. Additionally, the accumulation of fatty acids contributes to an increase in the acidity of rice. Starch cells also become hardened, and water absorption rates decrease. Although aged rice has not experienced mold or insect infestation, its nutritional value and edible quality have seriously declined. Therefore, the development of a convenient and efficient device for inspecting rice quality is of great importance for ensuring food security and promoting agricultural development. Since rice is rich in nutrients including proteins, carbohydrates, and lipids, these nutrients deteriorate with the aging process, generating various volatile organic compounds (VOCs), such as aldehydes, alcohols, ketones, etc., contributing to different odors. Consequently, odor is an important indicator of the different aging stages of rice. With the development of artificial olfactory systems and sensor technology, semiconducting metal oxide-based gas sensors have been developed for detecting characteristic biomarkers in rice aging. Nevertheless, the reliability of utilizing a single gas sensor to determine the rice quality needs to be further enhanced, so sensor arrays for the inspection of mixed odors, namely electronic nose (E-nose), have been developed. Due to the diversity, complexity, and low concentration of VOCs in rice aging, E-nose generally faces bottlenecks including high working temperatures, insufficient detection limits, and poor selectivity.

In order to address the above limitations, efforts should be focused on the aspect of the incorporation of oxygen vacancies to significantly elevate the gas-sensing performance, represented by the reduction of working temperature and the improvement of response, of metal oxide-based gas sensors. Specifically, the incorporation of oxygen vacancies is principally accompanied by a series of changes in physicochemical properties such as the bond breaking and remodeling, lattice distortion, and shifting of Fermi levels. Notably, the existence of highly concentrated oxygen vacancies can effectively decrease the bandgap of metal oxides, requiring less energy for electron excitation to the conduction band, ultimately resulting in a significant decrease in working temperatures. Furthermore, the incorporation of oxygen vacancies also induces the stable lattice structure to enter a metastable state due to the loss of oxygen atoms, thus increasing the adsorption activity and electron transfer efficiency

of metal oxides, displaying the improvement of the sensor response. Accordingly, incorporating oxygen vacancies helps to improve the gas-sensing performance of metal oxide-based gas sensors in the analysis of biomarkers in rice aging. To explore and develop this research field, a thorough investigation of metal oxides with varying concentrations of oxygen vacancies, fabricated by different routes, for the detection of VOCs in rice aging was performed. This thesis is chiefly organized into five chapters, as follows:

Chapter 1 provides a brief introduction to rice aging, and introduces the characteristics of VOCs that greatly contribute to rice aroma profiles. Meanwhile, the working principles and applications of an E-nose device as a reliable measurement in the inspection of rice quality based on the variation of aroma profiles are summarized. Then, the comparisons between E-nose and traditional instrumental methods, such as sensory evaluation, physical and chemical indicators, and instrumental analysis, are made. Finally, based on the discussions on the challenges and future trends of an E-nose system for the detection of rice quality, the objectives of this thesis are declared.

Chapter 2 characterizes the intrinsic properties, such as microstructure, morphology, phase composition, and chemical state, of the obtained metal oxides using the corresponding equipment. The gas-sensing devices and their operational parameters used in detecting standard gases and rice samples are introduced. Then, the gas-sensing attributes (i.e., response, selectivity, speed, stability, etc.) of metal oxides towards gas molecules are analyzed, providing an assessment of the gas-sensing performance of the developed gas sensors.

Chapter 3 synthesizes non-stoichiometric $W_{18}O_{49}$ hierarchical nanostructures through a simple hydrothermal method utilizing WCl_6 as the metal source and methanol as the solvent, and investigates the role of Ru incorporation on the microstructure evolution and gas-sensing properties of urchin-like $W_{18}O_{49}$ for the detection of nonanal, one of the medium-chain aldehydes generated in rice aging. Finally, two types of rice (japonica rice and indica rice) stored at different temperatures (25, 50, and 75 ℃) are utilized to verify the practicability of the 1.0%Ru-loaded $W_{18}O_{49}$-based gas sensor.

Chapter 4 regulates electronic structures and surface chemical states of CeO_2 nanowires, synthesized through a one-step hydrothermal route utilizing $CeCl_3$ as the metal source and deionized water as the solvent, and subsequently annealed under different controlled atmospheres (air, Ar, and 5%H_2+95%Ar). Then, the influence of post-treatment on microstructure evolution and gas-sensing performance of CeO_{2-x} for the detection of linalool, one of the alcohols generated by the further breakdown of aldehydes in rice aging, is investigated. Finally, two varieties of rice (japonica rice and indica rice) stored for various periods (1, 3, 5, 7, 15, and 30 days) are employed for the practicability of the sample annealed under the environment (5%H_2+95%Ar) with

strong reducibility.

Chapter 5 modulates the heterostructure configuration and oxygen vacancy in $ZnO/ZnSnO_3$ through solution precursor plasma spray (SPPS) utilizing $Zn(NO_3)_2$ and $SnCl_4$ with a molar ratio of 1:1 as the metal sources and the deionized water as the solvent. Then, the impacts of hydrogen flow on the microstructure evolution and gas-sensing properties of $ZnO/ZnSnO_3$ heterojunctions for the detection of 2-undecanone, one of the ketones derived from the oxidative degradation of unsaturated fatty acids in rice aging, are investigated. At last, the practical experiments of the developed gas sensor directly fabricated with the hydrogen flow of 3 L/min are verified by two kinds of rice (indica rice and japonica rice) stored for different periods (1, 3, 5, 7, 15, and 30 days).

Finally, the conclusions and perspectives for future work are presented.

Content

List of Figures

List of Tables

Chapter 1 Background

1.1 Rice aging

Rice, being a widely cultivated grain and one of the most important staple foods, is consumed by more than half of the world's population [1, 2], particularly in Asia, Africa, and South American regions. As a dominant source of carbohydrates, rice plays a significant role in providing basic energy and essential nutrients for consumers [3]. Therefore, rice quality is directly related to human health. Currently, the global grain output stands at 2.82 billion tons, leading to a substantial increase in grain crop reserves. However, during market circulation, varying storage conditions (i.e., temperature, pressure, humidity, etc.) can cause rice quality to deteriorate [4].

During storage or circulation, rice undergoes changes in sensory quality, chemical compositions, and physicochemical properties [5], contributing to various flavors, colors, and compositions [6, 7], collectively known as the aging process [8, 9]. Compared to fresh rice, aged rice exhibits different characteristics, including sensory quality such as hardness, viscosity, and aroma [7, 10-11], pasting properties [12, 13], physicochemical compositions [14], and even hygienic issues [1]. Among these characteristics, the aroma profiles of rice, which consist of various volatile organic compounds (VOCs), are key criteria for assessing rice quality and internal properties, with their content indicating the degree of aging [15, 16]. Changes in rice aroma profiles directly affect sensory quality, as the content of these compounds is associated with alternations in nutritional compositions and culinary quality, ultimately influencing consumer acceptance or rejection. Baietto and Wilson observed a strong correlation between flavor and rice quality, attributing it to the varied scents that align with consumer preferences [17]. Consequently, there is an urgent need for fast, reliable, and useful technology to monitor the aging process and evaluate rice quality based on changes in aroma contents. Moreover, by utilizing those aroma analyses, rice-producing enterprises can employ suitable techniques, such as high hydrostatic pressure [18, 19], and superheating [20], to effectively preserve rice quality. Nevertheless, the evaluation of rice quality still predominantly relies on individual preference, assessed primarily through visual examination and subjective satisfaction [21]. Therefore, the research and development of new instrumental methods for evaluating the aging process are crucial for inspecting rice quality, and remain a significant concern for agricultural industrials and consumers.

As a feasible and effective device, the electronic nose (E-nose), also known as an odor scanner, consists of an array of gas sensors, signal preprocessing algorithms, and

pattern recognition methods. By utilizing specific sensors with high responsiveness to measured volatiles and employing appropriate pattern recognition methods, the E-nose rapidly identifies aroma profiles in samples [22, 23]. Manufactured with the capability to serve as a detection tool, the E-nose holds promise for determining the VOCs generated during the aging of stored rice. E-nose devices effectively classify gas mixtures related to the physiology, chemical, and physicochemical performance of the product, distinguishing key components responsible for rice aging from a large number of VOCs [24]. Since its inception in 1982, E-nose technology has undergone significant advancements and continuous improvement, spanning from technological enhancements to breakthroughs in the market [25]. Numerous studies investigating the application of E-nose devices for agricultural food quality inspection have been conducted. They are extensively used across various domains, including dairy [26], forestry [27], medical and pharmaceutical fields [28, 29]. Furthermore, an investigation conducted by Rahimzadeh et al. revealed that the rice aging process could be effectively characterized using an E-nose device equipped with seven commercial metal oxide semiconductor (MOS)-based gas sensors [30]. Utilizing appropriate pattern recognition methods and artificial neural networks, this E-nose system accurately classifies the storage time of rice samples. They also conclude that this detection system could serve as an effective method for monitoring the aging process of rice.

Rice aging significantly impacts its end-use quality by exhibiting off-flavor sensory qualities. Consequently, monitoring the characteristic VOCs that affect rice quality plays a crucial role in enhancing the market share of rice and fostering the rapid development of the agricultural economy. To date, numerous scholars and researchers have conducted extensive experiments to identify the most abundant characteristic compounds, assessing the degree of rice aging using various E-nose devices coupled with advanced analysis methods. In this chapter, the typical VOCs and their content changes during the aging process of stored rice are first introduced. Aside from that, the utilization of E-nose equipment for determining these VOCs, such as 2-acetyl-1-pyrroline, aldehydes, heterocyclic compounds, alcohols, phenols, and ketones, is summarized, and the drawbacks of E-nose technology employed in analyzing rice quality are also highlighted. Furthermore, a comparison between E-nose and other traditional instrumental evaluation methods (i.e., gas-chromatography (GC), mass spectrometry (MS), high-performance liquid chromatography (HPLC), etc.) is provided. Finally, the challenges and future research trends related to the application of E-nose devices for rice quality inspection are discussed.

1.2 VOCs in rice aging

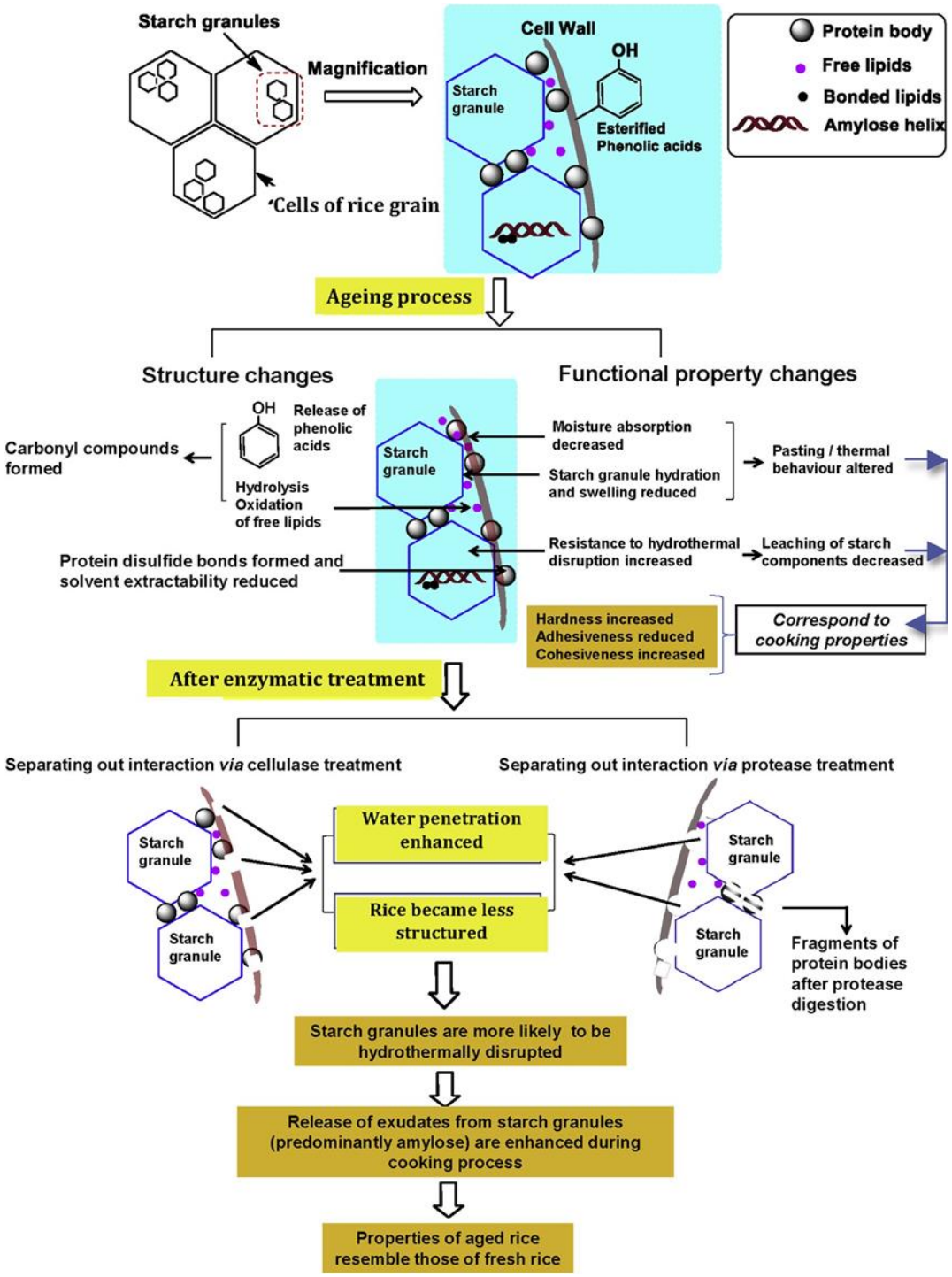

Fig. 1.1 Schematic illustration of rice aging at cellular and molecular level [6].

Rice is rich in protein (8%), lipids (1.5%), carbohydrates (75%), and other nutrient substances. Due to changes in external storage conditions and the activities of enzymes, these nutrients undergo degradation [31]. Extensive investigations have revealed that lipids undergo the most significant changes in the aging process, followed by proteins

and carbohydrates. The transformations in lipids are primarily attributed to hydrolysis and oxidation processes [32]. Hydrolysis results in the production of free fatty acids and the development of a rancid taste. Meanwhile, oxidation initially converts unsaturated fatty acids into hydroperoxides, and subsequently forms carbonyl compounds like aldehydes and ketones [33]. While the content of proteins in rice remains constant during storage, there are changes in its physicochemical properties. Chemical bond alterations, peptide modifications, and changes in protein solubility contribute to a decrease in protein solubility and a corresponding reduction in rice viscosity during storage [34]. The color and aroma of rice undergo significant changes, leading to a considerable decrease in its commercial value. Fresh rice exhibits a bright, translucent, and glossy appearance, while aged rice becomes darker and may exhibit increased chalkiness. The aroma of fresh rice is delicate, whereas aged rice emits a rancid flavor due to the deterioration. It is reported that the existence of aldehydes is a predominant factor contributing to the formation of off-flavors during storage, with some sulfide and furan compounds being associated with rice aging [35]. Furthermore, the sensory quality of aged rice undergoes a series of changes, primarily characterized by increased hardness and diminished palatability. These alterations collectively contribute to a decline in rice quality.

During the aging process, the nutritional components and sensory qualities of rice undergo deterioration, leading to the generation of numerous VOCs. These VOCs comprise chemical compositions derived from the combination of rice samples and flavor. As demonstrated in Fig. 1.1, rice aging is a complicated process, causing structural changes in rice that contribute to the formation of characteristic VOCs. These changes in functional properties also affect rice pasting, thermal, and cooking characteristics. Due to their instability, nutrient substances such as carbohydrates, lipids, and proteins decompose into over 300 types of VOCs during aging, contributing to different rice aroma profiles [2, 18, 36]. Tab. 1.1 outlines the major VOCs formed through the hydrolysis or oxidation of nutrients in rice aging. Representative VOCs generated during rice aging include alcohols, aldehydes, heterocyclic compounds, acids, etc. During storage or processing, lipid oxidation is a critical pathway for the formation of off-flavor compounds, with aldehydes serving as characteristic VOCs in rice aging. Hexanal and octanal, termed to be indicators for lipid oxidation in black rice, are also noteworthy in this context. Generally, once storage conditions including temperature and humidity are suitable, microorganisms proliferate rapidly, leading to the production of mycotoxins by molds during their metabolic processes. This microbial activity contributes to a significant increase in the concentration of certain VOCs (i.e., acids, aldehydes, nitrogen heterocyclic compounds, etc.), ultimately leading to the formation of undesirable odors [38].

Tab. 1.1 VOCs generated in rice aging.

Sources	VOCs	Ref.
Carbohydrates	Alcohols, aldehydes, ketones, carboxylic acid	[37]
Lipids	Aldehydes, acids	[38]
Proteins	Ammonia, hydrogen sulfide, ethyl mercaptan	[18]

Moreover, environmental circumstances, including vacuum level, temperature, and moisture, play a significant role in the rice aging process. Liu et al. utilized principal component analysis to explore changes in the volatile content of three rice varieties stored under 90% relative humidity at varying vacuum levels (0, 0.5, 0.7, and 0.9 kg/cm^2) [39]. They observed a correlation between the concentration of VOCs and vacuum level during rice aging. Additionally, storage temperature and duration are crucial factors affecting the rate of rice quality deterioration. Prolonged storage at elevated temperatures contributes to a decline in nutritive substances and culinary quality, and an increase in unpleasant odors [40]. Choi et al. identified volatiles in black rice stored at temperatures of 25 and 35 ℃, respectively [41]. They found that samples stored at 25 ℃ for 6 months did not exhibit significant increases, while those stored at 35 ℃ for 1 month showed a significant rise in content. This was primarily attributed to the effective inhibition of enzyme catalytic reactions at low temperatures, resulting in a slower deterioration rate of rice aroma profiles. Generally, storing rice at lower temperatures is more suitable for preserving desirable aroma profiles. Furthermore, Champagne et al. reported a significant increase in the aroma profiles of paddy rice when stored at high moisture levels for 48 hours [42]. They emphasized that the optimum moisture range for maintaining rice aroma quality during storage fell between 17% and 21%. Above all, changes in external storage conditions have a significant impact on various aspects of rice quality, encompassing nutritional components, eating quality, appearance, etc. These changes seriously affect the purchase intention of individual consumers and do not conform to the green and healthy life concept. The aging process diminishes both the edible and commercial value of rice. Consequently, the detection of rice aging holds important practical significance, enabling timely interventions to maintain and enhance rice quality for consumers.

Identifying and discriminating the most abundant representative VOCs that contribute to aroma profiles is crucial in assessing rice quality during storage. Due to complex chemical reactions among various VOCs and numerous influencing factors such as genetics, planting, processing and storage, rice aging is quite a complex process [43]. Quality analysis of aged rice predominantly relies on the comprehensive assessment of diverse characteristic VOCs rather than focusing on just one or two varieties [44]. Tab. 1.2 summarizes several rice varieties and their major VOCs

identified throughout the aging process, as determined by various instrumental measurements. In general, VOCs consist of multiple chemical components derived from the aging of rice during storage. Each type of rice possesses distinctive aroma profiles manifested in the form of a gas mixture. Aldehydes, alcohols, ketones, and heterocyclic compounds emerge as the most representative compounds among the identified VOCs. These characteristic VOCs in rice aging include aromatic, oxygen-containing, sulfur, and nitrogen groups. The intensity of the aromatic group in rice is closely associated with unsaturated bonds and alkane chain length.

1.3 Application of E-nose for inspecting rice quality

Thorough discrimination of VOCs plays a significant role in the evaluation of rice quality. The emergence of the E-nose offers a novel approach to assessing rice quality. Designed to simulate the human olfactory system, the E-nose is an "intelligent" device [22, 52]. Its origin dates back to the pioneering work of Persaud and Dodd, who employed a sensor array consisting of three SnO_2-based gas sensors to simulate the mammalian olfactory system [53]. They successfully analyzed 21 types of VOCs, including amyl acetate, ethanol, ether, valeric acid, lemon oil, and vanillin isobutyrate. Since then, E-nose has been continuously used to explore the types and concentrations of simple organic or inorganic gases, determine the varieties and origins of tobacco, coffee, and wine, and monitor air quality.

Commercially available E-nose was introduced in 1993, and recent advancements have focused on achieving cost-effective and non-destructive testing. Using odor-sensing materials, E-nose devices can classify changes in VOCs among different rice varieties based on their unique aroma patterns. Comprising various data processing methods and predictive models, E-nose devices hold significant potential for applications in rice quality inspection [54]. Depending on the working principle, sensor arrays can be classified into MOS, conductive polymer, solid electrolyte, and photoionization [55, 56]. Tab. 1.3 demonstrates common models of E-nose devices applied for rice quality assessment, with mature products including the Fox series from Alpha MOS Company in France and the PEN series from Airsense Company in Germany. E-nose equipment mainly consists of an array of sensors and an integrated data analysis algorithm, similar to the working principle of traditional analytical methods. MOS-based sensor arrays are the most commonly used, and the principal component analysis (PCA) method is frequently employed for accurately analyzing the results obtained from sensor responses.

Tab. 1.2 Typical VOCs identified in the aging of different rice varieties.

Sample	Type	Special VOCs	Main VOCs	Method	Condition	Ref.
Japonica rice	74	nonanal, hexanal, heptanal, 2,4-decadienal, 1-octen-3-ol, 2-nonanaol, 1-heptanol, 6,10-dimethy-5, 2-heptanone	aldehydes, alcohols ketones, heterocycles, esters, alkanes, alkenes, arenes	SPME-GC/MS	Hydrostatic high pressure pretreatment	[45]
Jasmine rice	71	nonanal, 2-nonenal, 1-octen-3-ol, 1-octanol, 2-octen-2-one, 2-heptanone				
Basmati rice	88	2-undecaone, 2-heptanone, 1-octen-3-ol, linalool, nonanal, pentanal, nonane, dodecane, allylcyclohexane, 7-tetradecene, 1-(1H-Pyrrol-2-yl) ethanone, ethyl hexanoate, methyl 2-aminobenzoate, 2-pentylfuran	ketones, alcohols, aldehydes, alkanes, alkenes, heterocycles, esters, furans	HS-SPME-GC/MS	Long-term storage	[46]
White rice	59	hexanal, nonanal, 2-nonanone, ethanol, 1-hexanol, ethyl hexadecanoate, 2-pentylfuran, 1,4-xylene, toluene, 4-vinyl-2-methoxyphenol	aldehydes, ketones, alcohols, esters, furans, hydrocarbons, phenols, and lactones	GC-MS	Fermentation	[47]
Brown rice	68	nonanal, benzaldehyde, 2-heptanone, 3-octen-2-one, 1-octen-3-ol, 1-octanol, methyl hexadecanoate, hexadecane, 2-pentylfuran, benzothiazole				
Indica rice	-	hexanal, 1-hexanol, nonanal, 2-nonenal, benzyl alcohol, guaiacol, 2-octenal	aldehydes, alcohols, phenols	HS-SPME-GC-FID	Temperatures	[48]
Black rice	54	nonanal, hexanal, 2-undecanone, 2-heptanone, 1-octen-3-ol, methyl hexanoate, methyl myristate, (3E)-3-ethyl-2-methyl-1,3-hexadiene, phenol, guaiacol	aldehydes, ketones, alcohols, acids, esters, olefins	HS-SPME-GC/MS	Milling and long-term storage	[41]
White rice	29	heptane, 1-octen-3-ol, hexanal, 2-undecaone, isopropyl formate, ethylbenzene, phenylacetaldehyde, dimethyl trisulfide	alkanes, alcohols, aldehydes, ketones, furans, esters, phenols	GC-MS	Temperature	[49]
African rice	41	nonanal, hexanal, linalool, 1-octen-3-ol, 2-decanone, (E)-2-octenal, 2-pentylfuran, acetophenone, 2-heptanone, limonene	aldehydes, alcohols, ketones, furans, phenols	GC/MS	Temperature	[50]
Aromatic rice	79	nonanal, hexanal, 2-undecanone, pentadecane, 3-methylundecan, 1-octen-3-ol, 2-pentylfuran, n-hexadecanoic acid methyl ester, 3,4-dimethoxytoluene	Aldehydes, ketones, alkanes, alcohols furans, acids, toluenes, 2-AP	SPME-GC/MS	Temperature	[51]

Note: HS, head space; SPME, solid phase micro-extraction; GC, gas-chromatography; MS, mass spectrometry; FID, flame ionized detector.

Tab. 1.3 Application of E-nose device for rice quality assessment.

Sample	Sensor	Model	Number	Analysis	Ref.
Jasmine rice	MOS	FOX 3000	12	PCA, LDA, SVM. PLS	[57]
Brown rice	MOS	FOX 300	12	PCA	[58]
	CP	Cyranose-320	32	PCA, CDA	[59]
	MOS	PEN 3	10	PCA, KNN, PNN, SVM	[60]
Jasmine rice	MOS	-	8	PCA, SVM, BP	[61]
Indica rice	MOS	PEN 3	10	PCA, LDA	[62]
	MOS	-	10	PCA, LLE, SVM, KNN	[63]
Japonica rice	MOS, MOSFET	-	23	PCA	[64]
Domsiah rice	MOS	-	7	PCA, BP, RBF, LVQ	[30]
Milled rice	MOS	FOX 2.0	18	PCA	[65]

Note: MOS, metal oxide semiconductor; CP, conductive polymer; MOSFET, metal-oxide-semiconductor field-effect transistor; PCA, principal component analysis; KNN, k-nearest neighbor; PNN, probabilistic neural network; SVM, support vector machine; CDA, canonical discriminant analysis, LDA, linear discriminant analysis; PLS, partial least squares; BP, back propagation; LLE, locally linear embedding; RBF, radial basis function; LVQ, learning vector quantization.

1.3.1 Working principle

In the realm of rice quality, VOCs possess a unique characteristic that makes them valuable for both quality deterioration assessment and identification. Consequently, E-nose equipment can be extensively employed in evaluating changes in rice quality by identifying the characteristic VOCs [66]. The critical component of an E-nose device is its detection unit composed of sensor arrays [67]. In this regard, characteristic VOCs adsorb onto the surface of the sensing materials, where they undergo a reaction, causing changes in the electrical signal. The types and concentrations of characteristic VOCs generated during rice aging process are then obtained based on the analysis of these electrical signals.

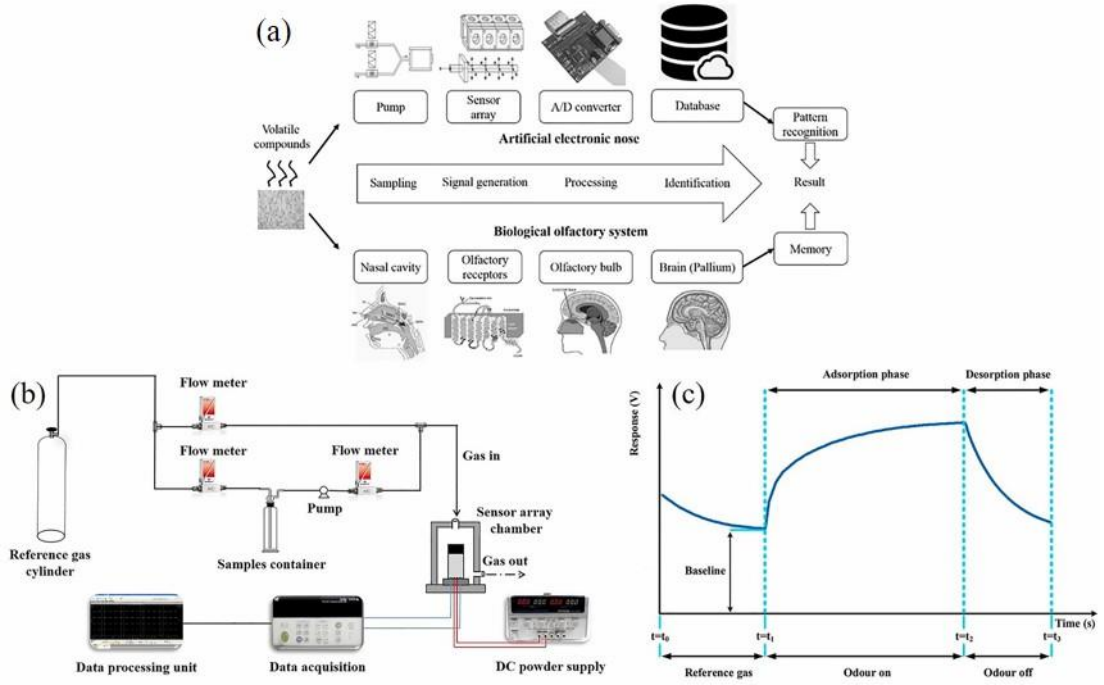

Fig. 1.2 Schematic diagram of E-nose devices for rice quality inspection. (a) Working principle of an artificial E-nose and its biological counterpart [68, 72], (b) typical apparatus of an E-nose detection system, (c) working cycles of the individual sensor in the detection process [30].

Fig. 1.2 depicts a schematic illustration of an E-nose device for rice quality inspection. The E-nose is comprised of three major components, namely the sample handling for collecting volatile compounds, the detection unit composed of chemical sensor arrays, and the data processing system integrated with a signal processing device [68, 69]. The working principle involves electron exchange between the rice aroma and the sensing materials. Subsequently, the sensor response is influenced by changes in the types and concentrations of VOCs, which are then processed by the signal processing system. This process is pivotal for developing highly sensitive gas-sensing materials towards the measured gas mixtures. Ultimately, through the utilization of appropriate pattern recognition methods (i.e., PCA, PLS, LDA, etc.) and artificial neural networks (i.e., BP, RBF, LVQ, etc.), databases are established for the rapid assessment of rice aroma flavor substances. After calibration, E-nose equipment can effectively identify the aroma during rice aging, leading to the accurate discrimination of rice samples with high precision [70-72].

Tab. 1.4 Analysis of VOCs contributed to rice aroma profiles [73].

Main VOCs	Special VOC	Formula	Odor
alkanes	3-methylundecane	$C_{12}H_{26}$	cooked vegetable flavor, floral aroma
	5-methyltridecane	$C_{14}H_{30}$	cooked vegetable flavor, floral aroma, popcorn scent
	tetradecane	$C_{14}H_{30}$	floral aroma
	pentadecane	$C_{15}H_{32}$	grass odor
alcohols	1-octen-3-ol	$C_8H_{16}O$	mushroom fragrance
	linalool	$C_{10}H_{18}O$	citrus blossom fragrance, sweet scent
	isoamyl alcohol	$C_5H_{12}O$	fruity flavor
	1-hexanol	$C_6H_{14}O$	scent of apples
	heptan-1-ol	$C_7H_{16}O$	sweet and nutty taste
	1-nonanol	$C_9H_{20}O$	rose wax and fruity aroma
	decan-1-ol	$C_{10}H_{22}O$	sweet, floral, and fruity aromas
	2-methylbutan-1-ol	$C_5H_{12}O$	floral scents
	2-ethyl-1-hexanol	$C_8H_{18}O$	fragrant tender leaves
	benzyl alcohol	C_7H_8O	sweet taste
aldehydes	isovaleraldehyde	$C_5H_{10}O$	malt flavor
	hexanal	$C_6H_{12}O$	fragrant and fruity aroma
	valeraldehyde	$C_5H_{10}O$	woody and fruity
	octanal	$C_8H_{16}O$	citrus
	heptanal	$C_7H_{14}O$	fruity aroma
	nonanal	$C_9H_{18}O$	rose and citrus fragrance
	decanal	$C_{10}H_{20}O$	sweet, citrus and floral aromas
	benzaldehyde	C_7H_6O	bitter almond and cherry fragrance
	phenylacetaldehyde	C_8H_8O	cooked vegetable flavor
	furfural	$C_5H_4O_2$	bitter almond flavor
	(2E)-2-octenal	$C_8H_{14}O$	nutty taste
	(2E)-2-nonenal	$C_9H_{16}O$	fragrances of fat, butter, beans, cucumber, and wood
	CIS-4-heptenal	$C_7H_{12}O$	milk fragrance
	(2E,4E)-deca-2,4-dienal	$C_{10}H_{16}O$	fat and waxy odor
	vanillin	$C_8H_8O_3$	vanilla flavor
	isovanillin	$C_8H_8O_3$	popcorn flavor
ketones	6-methylhept-5-en-2-one	$C_8H_{14}O$	lemon fragrance
	6,10-dimethyl-5,9-undecadien-2-one	$C_{13}H_{22}O$	floral fragrance
	3-octen-2-one	$C_8H_{14}O$	orange flavor, herbal fragrance
	3-nonen-2-one	$C_9H_{16}O$	herbal and floral fragrance
	2-butanone	C_4H_8O	acrid odor
	2-heptanone	$C_7H_{14}O$	pear fragrance

	2-decanone	$C_{10}H_{20}O$	peach fragrance
	2-octanone	$C_8H_{16}O$	milk, cheese, mushroom fragrance
	3-octanone	$C_8H_{16}O$	herbal and floral fragrance
	2-undecanone	$C_{11}H_{22}O$	cooked vegetable flavor
	butane-2,3-dione	$C_4H_6O_2$	fresh scent
	(+/-)-camphor	$C_{10}H_{16}O$	grass odor
esters	hexyl formate	$C_7H_{14}O_2$	fresh scent
	methyl acetate	$C_3H_6O_2$	clear and sweet fragrance
	ethyl acetate	$C_4H_8O_2$	fruity aroma
	butyl acetate	$C_6H_{12}O_2$	fruity aroma
	butyl propanoate	$C_7H_{14}O_2$	fruity aroma
acids	1-hexanoic acid	$C_6H_{12}O_2$	tart flavor
	n-heptanoic acid	$C_7H_{14}O_2$	
	octanoic acid	$C_8H_{16}O_2$	
others	indole	C_8H_7N	tar fragrance
	guaiacol	$C_7H_8O_2$	smoky flavor
	4-hydroxy-3-methoxystyrene	$C_9H_{10}O_2$	putty, spicy, and clove like aromas
	2-AP	C_6H_9NO	popcorn fragrance
	2-butylfuran	$C_8H_{12}O$	nut roasted aroma

1.3.2 VOCs detection

As a rapid and non-destructive assessment technology, E-nose holds the potential to make substantial contributions to the field of rice quality assessment and identification. This section mainly concentrates on recent advances in E-nose for quality evaluation and determination of rice samples. Tab. 1.4 illustrates the characteristic VOCs, such as alkanes, alcohols, aldehydes, ketones, esters, acids and others, identified in the process of rice aging. Based on this, the analysis of specific compounds including 2-acetyl-1-pyrroline (2-AP), aldehydes, heterocyclic compounds, alcohols, and ketones possesses a specific purpose in inspecting rice quality during storage and processing.

1.3.2.1 2-AP

Nowadays, 2-AP, is considered to be the dominant odorant that greatly contributes to rice aroma profiles, with a unique odor similar to nuts and popcorn [36, 74, 75]. It has a low odor threshold of 0.1 ng/g in water and 0.02-0.04 ng/L in air [76] and contributes a popcorn-like aroma to rice, recognized as the most characteristic VOC for distinguishing aromatic rice from non-aromatic varieties. It was suggested that rice aroma intensity mainly depended on the 2-AP content which varied among rice cultivars. 2-AP content was reported to be 0.3-347 ng/g in Basmati rice. The differences in content derived from differences in samples varieties, processing, storage, harvest,

and evaluation methods. Despite the ultra-low content of 2-AP in rice, it still can be easily perceived by the human olfactory system. Meanwhile, rice aroma profiles are believed to be closely related to the changes in 2-AP content among different rice varieties. It is reported that the 2-AP content is 100-760 and 0.2-2746 μg/kg in two kinds of aromatic rice, respectively [77]. However, with the prolonging of storage time, the 2-AP content experiences a significant decrease [78], which is a crucial factor contributing to the deterioration of rice aroma profiles. Simultaneously, even rice of the same variety grown under the same conditions may have a significant difference in 2-AP content caused by differences in harvest data and postharvest handling.

As a polar compound, the volatilization of 2-AP in rice aging is inevitable. Therefore, the E-nose can be available for the identification and discrimination of 2-AP. This enables the monitoring of the rice aging process and the assessment of its quality. Udomkun et al. explored the feasibility of utilizing an E-nose device equipped with 12 MOS-based gas sensors to classify Pathumthani 1 rice mixed with Khaw Dok Mali 105 variety at different ratios based on changes in the rice aroma profiles during storage for 5 months [79]. The PCA method was employed to analyze the sensor responses obtained from the detection units. The results revealed that this evaluation method exhibited good discrimination of mixed rice samples during storage. Moreover, they reported a significant decrease in the content of 2-AP over the storage period, which was consistent with the conclusions drawn by Norkaew et al [78]. Nevertheless, even under the same cultivated conditions, the 2-AP content in the same rice variety exhibits significant variation. This is mainly attributed to different processing methods used to maintain rice quality during storage, which plays a crucial role in the changes in rice aroma profiles [80]. The influence of the cooling processing method on changes in 2-AP concentration in cooked rice during storage was investigated by Ma et al [81]. The parameters concerning cooling rates used in their work were set to 0.19, 1.27, 1.74, and 2.88 ℃/min, respectively. They utilized a GC-based E-nose device to investigate the aroma profiles and their differences in rice aging. Additionally, the relationships between rice aroma profiles and sensor array responses were analyzed using two pattern recognition methods (PCA and PLS). The results from the E-nose showed that the cooling rate significantly affected the volatilization of the aroma compounds, with a higher cooling rate extending the retention of rice aroma profiles. PCA results highlighted the substantial contribution of 2-AP to rice aroma profiles, while PLS analysis revealed that 2-AP had a significantly positive effect on sensory evaluation at lower cooling rates. Accordingly, based on these investigations, it is evident that an E-nose device, by monitoring changes in 2-AP content, can effectively assess the rice aging process and accurately determine its quality.

2-AP is considered to be the most characteristic VOC contributing to rice aroma profiles, and its content serves as a standard for distinguishing aromatic rice from non-aromatic ones [18, 82]. However, due to its instability, 2-AP can be lost or regenerated during the feature extraction stage in rice quality inspection [83, 84], which has a substantial impact on the results obtained from the E-nose. Furthermore, the concentration of 2-AP significantly decreases with the prolongation of storage periods. Hence, the limit of detection of gas sensor arrays remains a significant challenge for rice quality inspection based solely on the 2-AP content.

1.3.2.2 Aldehydes

Aldehydes, known to be generated by the oxidation and hydrolysis of lipids, play a dominant role in contributing to rice aroma among all categories because of their relatively low odor threshold. The levels of aldehydes in rice aging are primarily influenced by increased lipase and lipoxygenase activity [62, 85, 86]. Hexanal, one of the aldehydes, is derived from the decomposition of linoleic acid and is considered to be a major compound in rice aging. With a low odor threshold of 1.1 ng/L in air, hexanal is characterized by scents described as green, fruity, and grass (Tab. 1.4). It is acknowledged to be an indicator of rice quality deterioration, potentially leading to consumer rejection of samples [87]. Furthermore, the content of hexanal in intact rice is lower than that in broken rice, mainly due to the greater presence of surface lipids and free fatty acids [88]. Meanwhile, a higher concentration of hexanal contributes to the development of off-flavor in rice aging. Nonanal, contributing flavor of citrus, cucumber, floral, fresh, grass, soapy, fatty, has a low odor threshold of 3.1 ng/L. Octanal, with an odor threshold of 0.88 ng/L, contributes to a slightly fruity flavor. It was reported that octanal, heptanal, decanal, nonanal, 2-nonenal, and 2-heptanone were derived from oleate hydroperoxide decomposition, while hexanal and 2-pentenal were produced from linolenate hydroperoxide decomposition. Linoleate decomposition resulted in the formation of hexanal, pentanol, pentanal, 2-pentylfuran, and 2-octenal [89, 90]. Takemitsu et al. evaluated rice quality by identifying important odor-active compounds, represented by nonanal, through GC-olfactometry [22]. Tentatively identification was realized by comparing retention index and odor property with reference material. Although GC-olfactometry was useful for flavor identification of aroma-active compounds from food samples, it was not efficient for the qualitative or quantitative analysis of volatiles.

Combining the advantages of artificial olfactory systems with those of sensory description, E-nose could not only realize the detailed sensory analysis of rice odor quality, but also achieve quantitative and qualitative evaluation of volatiles. Suzuki et al. reported a significant increase in aldehydes, including pentanal and hexanal, with the prolongation of the storage period [85]. However, other researchers suggested that

the content of aldehydes exhibited a remarkable decrease during storage [15, 91]. Furthermore, the concentration of aldehydes is closely related to the storage condition. Generally, under storage conditions with high temperature and high humidity, the concentration of aldehydes dramatically increases. The concentration of aldehydes in two types of aromatic rice under different temperatures (4, 30, and 70 ℃) was investigated by Zhao et al [92]. They utilized an E-nose composed of 18 MOS-based gas sensors to discriminate aroma changes in rice samples. Through PCA analysis, the E-nose successfully identified and classified rice samples with an accuracy of 97%. Hexanal emerged as the most characteristic VOC in almost all samples, with its mass fraction changing from 5.08% to 40.94%. This change in hexanal concentration served as an indicator of rice quality deterioration. Furthermore, under high temperature and high humidity conditions, the expressions of lipase and catalase increase and decrease, respectively, accelerating the hydrolysis or oxidation of lipids. An experiment investigating the role of storage temperature and humidity on the generation of aldehydes in paddy rice was conducted by Yuan et al [35]. They accurately discriminated exclusive patterns of different aroma compounds using an E-nose detector equipped with headspace sampling equipment. This detection device included an array of 12 MOS-based gas sensors, and PCA was employed for the analysis of the obtained sensor responses. The results revealed that the concentration of aldehydes dramatically increased when rice was stored under a higher temperature (37 ℃) and a higher humidity (70%RH), leading to an obvious deterioration in rice quality.

In summary, aldehydes play a significant role as dominant volatile compounds contributing to rice aroma profiles, and their concentrations serve as an index for monitoring rice aging. Temperature is a crucial factor affecting the concentrations of aldehydes, with high temperature accelerating the oxidation rates of lipids. Nevertheless, the working temperature of an E-nose typically ranges from 200 to 400 ℃, which may have a significant influence on the concentration of aldehydes. The high working temperature poses a barrier to the application of E-nose for rice quality inspection based on changes in the contents of aldehydes.

1.3.2.3 Heterocyclic compounds

Heterocyclic compounds, such as pyrazines, furans, pyridines, pyrroles, thiazoles, thiophenes, imidazoles, etc., generated through the Maillard reaction and lipid oxidation, are also major contributors to rice aroma, especially in brown rice. Some of these compounds, including 2-ethyl-3,5-dimethylpyrazine, 2-pentylfuran, 2-methylfuran, and 2-acetyl-2-thiazoline, possess relatively low odor thresholds, making them important in the formation of exclusive aroma profiles during rice aging [93, 94]. With their unique caramel-like scents, furans are generally recognized as the most abundant heterocycles. They are generated from the dehydration of carbohydrate-based

Maillard reaction, normally contributing to caramel-like odor of heated carbohydrate [95]. Furans are also crucial biomarkers for aging discrimination, particularly for identifying and classifying long-aged rice [96]. 2-Pentylfuran, which is the most significant alkylfuran identified in rice aging, has a characteristic nutty odor in dilute concentration and a less pleasant aroma characteristic of soybeans at higher concentrations [97]. It was also reported as an odor-active compound in aromatic, non-aromatic and black rice with floral, fruity, nutty, green, almond, buttery and beany aroma [98]. Higher 2-pentylfuran content was found in aromatic rice cultivars than non-aromatic ones [99]. Additionally, pyrazines, thought to be key VOCs contributing to rice aroma profiles, can produce an unpleasant pungent odor and have a characteristic roasted nutty flavor relying upon their concentration [97].

Research indicates that the roasting process is a powerful and effective technique for maintaining rice quality, as it can increase the concentration of heterocycles while reducing the types and quantities of hydrocarbons and benzene derivatives [100]. In this regard, Shi et al. investigated the changes in VOCs in brown rice aroma profiles under various roasting times and temperatures using an E-nose coupled with 12 MOS-based gas sensors [58]. The results, shown in Fig. 1.3a, highlighted the significant role of roasting time in the volatilization and release of aroma compounds in brown rice. The PCA image (Fig. 1.3b) indicated that the contribution rate of the two principal components was up to 99.695%, signifying that VOCs significantly changed with increasing roasting times. Fig. 1.3c illustrates the changes in relative contents and varieties of aroma profiles in brown rice roasted at 120 ℃. Eleven types of VOCs were identified, with furans and pyrazines being the two dominant compounds with higher aroma profiles in brown rice. Moreover, the contents of both furans and thiophenes compounds identified at a roasting time of 15 minutes were 5 times higher than those at a roasting time set at 60 minutes, primarily due to microstructure changes in the roasted brown rice.

Heterocyclic compounds are crucial components in rice aroma profiles. An E-nose system, equipped with some appropriate pattern recognition methods, can effectively assess and accurately identify rice quality during storage based on the changes in its content. However, the analysis of the obtained results demonstrated in Fig. 1.3c suggests that an E-nose can discriminate and quantify a large group of VOCs, but it may not specifically identify individual ones. As a result, an E-nose can be employed for preliminary inspection and classification of rice quality based on representative aroma profiles generated from rice aging. This preliminary assessment can provide valuable insights into the overall quality of the rice samples, allowing for further targeted analysis if necessary.

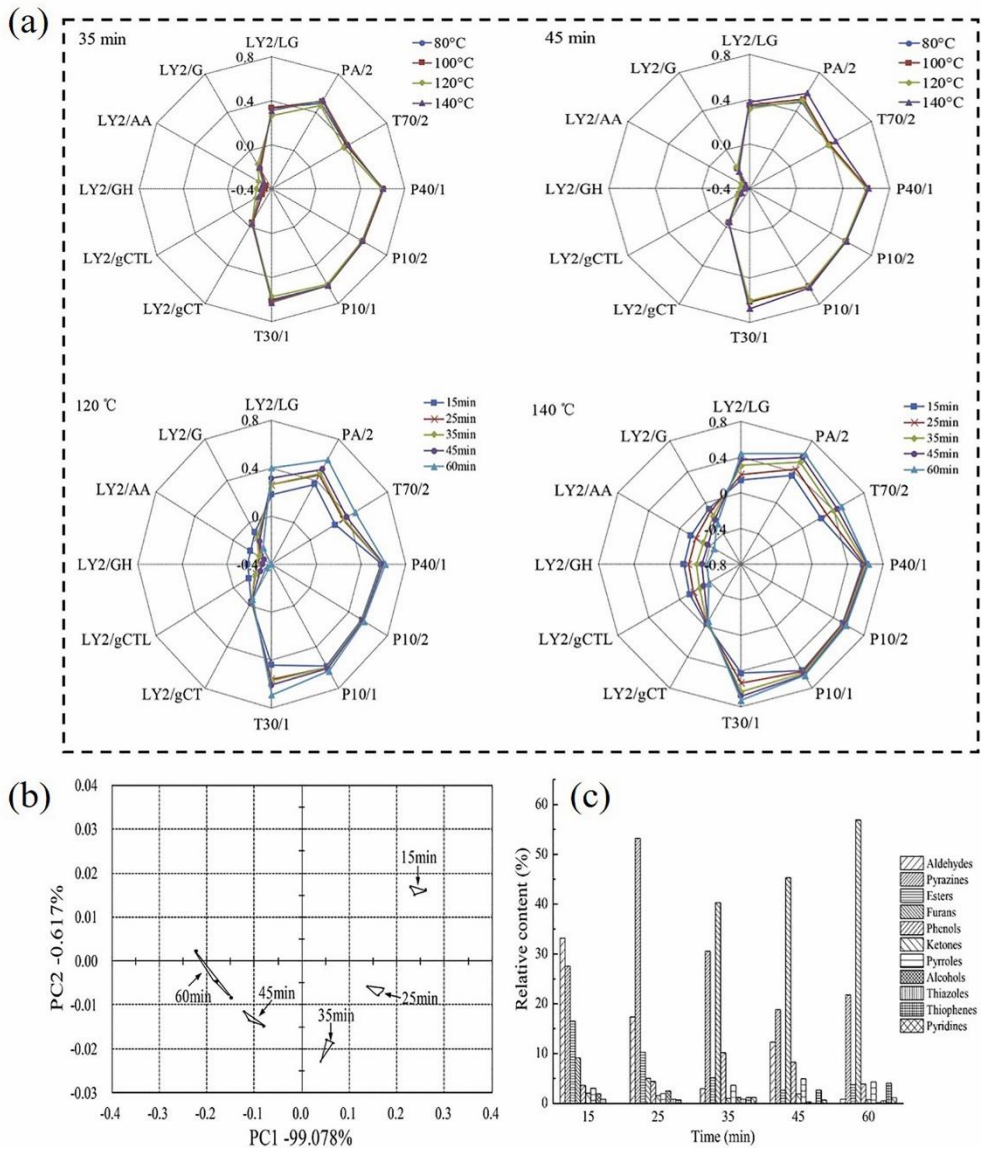

Fig. 1.3 Response obtained from the sensor array analyzed by (a) radar fingerprint chart and (b) principal component analysis, (c) changes in relative contents and aroma types [58].

1.3.2.4 Alcohols and phenols

Alcohols are considered to be one of the characteristic biomarkers formed by the hydrolysis of carbohydrates and further decomposition of aldehydes in rice aging [18, 37]. They are the second most abundant volatiles in cooked white rice, accounting for approximately 20.3%, slightly lower than aldehydes [101]. Phenols, on the other hand, are generated from the decarboxylation of fatty acids in rice [3, 102]. While some alcohols possess relatively high odor thresholds, others, along with most phenols, have relatively low odor thresholds, making a significant contribution to the volatile compounds in the aroma profiles during aging [81, 103]. Hexanol, derived from the oxidation of lipids, is one of the most abundant compounds identified in rice aging. It features sweet, herbaceous, and green odors. Higher concentrations of hexanol are also

discriminated in Basmati rice compared to non-aromatic rice varieties, indicating a potential biomarker for aromatic rice [82, 87]. In addition, research conducted by Lin et al. revealed that the concentration of hexanol first increased and then decreased in rice samples during storage over a period ranging from 1 to 10 months [38]. This fluctuation in hexanol concentration may reflect dynamic changes in the lipid oxidation process and other biochemical reactions occurring during rice aging.

It has been reported that the concentration of alcohols in aromatic rice is higher than that in non-aromatic cultivars [104, 105]. Consequently, alcohols, with their slightly sweet odor, can serve as a potential standard for classifying aromatic rice from non-aromatic ones, especially in Basmati rice. Leveraging the VOCs produced from the samples, an E-nose can effectively inspect and classify aromatic rice varieties. Kang et al. qualitatively and quantitatively discriminated VOCs in Korean rice aging using an E-nose equipped with the partial least-squares regression method [106]. They pointed out that fuel alcohols were the characteristic volatiles in aromatic rice cultivars. Similarly, Serafico and Sevilla utilized an E-nose composed of 18 MOS-based gas sensors with polarities to discriminate Philippine aromatic rice [107]. The statistics obtained from the sensor arrays were analyzed through PCA and hierarchical clustering analysis (HCA), respectively. Among them, PCA analysis showed that this detection instrument classified the samples into various varieties with an accuracy of 95%. HCA revealed that all samples were classified into one group. Moreover, sensors exhibited high-magnitude responses towards alcohols. In addition, fatty acid values are also major biomarkers indicating rice aging [72]. Li et al. comprehensively investigated changes in fatty acid contents in rice using an E-nose consisting of 10 MOS-based gas sensors [108]. PCA, LDA, and loading analysis results all revealed that saturated fatty acid values increased, whereas unsaturated fatty acid reduced in rice aging.

In this regard, different data processing methods are utilized in the classification of aromatic rice cultivars. The accuracy of identifying aromatic rice cultivars using an E-nose heavily depends on the chosen data processing methods and prediction models. . Therefore, selecting appropriate data processing techniques is crucial for achieving precise assessments of rice quality based on the characteristic biomarkers produced during rice aging. With the right methods in place, an E-nose can serve as a powerful tool for accurately evaluating rice quality.

1.3.2.5 Ketones

Ketones, like aldehydes, play a significant role in contributing to the unique aroma profiles of rice. These compounds, formed through various processes such as oxidative degradation of unsaturated fatty acids or microbial oxidation, contribute to the oveall fragrance of rice, often characterized by fruit, floral, herbal, and other pleasant aromas. For instance, 2-undecanone, 2-heptanone and 6-methyl-5-hepten-2-one, 3-octanone,

and 3-none-2-one are known to contribute to fruit, floral, and herbal aromas in rice (Tab. 1.4). Studies, such as the one conducted by Dias et al., have identified a variety of volatile compounds, including aldehydes and ketones, in aromatic rice using GC-MS [51]. These compounds represent a significant portion of the total aroma profile of rice, contributing to its characteristic fragrance. For example, aldehydes like pentanal, nonanal, octanal, and hexanal, along with ketones like 2-undecaone, 2-dodecanone, 3-octen-2-one, and 4-hydroxy-4-methyl-2-pentanone, have been found to contribute substantially to the overall aroma of aromatic rice.

The reported increase in ketone content in fragrant rice under high-temperature storage aligns with similar changes observed in volatile compounds with increased accumulated temperature [92]. This phenomenon may be attributed to thermal oxidation or degradation of fatty acids induced by the elevated temperature. Building on this observation, Shi et al. conducted a study to investigate the effects of storage temperature on ketone content in japonica rice using an E-nose system (FOX 3000, France) [109]. They observed a significant increase in volatile ketones, including 2-undecanone, hexadecane, pentadecane, among others, measured by the E-nose across three granaries subjected to temperatures ranging from 65 to 100 ℃. Analysis of the radar map indicated that the accumulated temperature led to a higher presence of volatile ketones in the rice samples. This increase in ketone content was attributed to thermal oxidation or degradation of fatty acids triggered by the rise in storage temperature, which was closely associated with microbial volatiles. These findings underscore the impact of storage conditions, particularly temperature, on the composition of volatile compounds in rice aging, highlighting the potential of E-nose technology in monitoring such changes for quality assessment and preservation purposes.

Above all, storage temperature has an essential effect on the contents of volatile ketones. High storage temperature accelerates the oxidative degradation of unsaturated fatty acids, generating high concentrations of ketones, thus contributing to the formation of unique rice aroma profiles. However, as stated in Section 1.3.2.2, E-nose systems generally suffer from bottlenecks such as high working temperatures, which can significantly increase the contents of ketones. Consequently, this bottleneck limits the use of E-nose to effectively inspect rice quality solely based on changes in ketone contents.

1.4 Comparison between E-nose and other evaluation methods

There are many conventional measurements available for assessing rice quality in the aging process, including sensory evaluation with the human nose [110, 111], physical and chemical index method [112], qualitative and quantitative analysis of

VOCs relying upon instrumental analysis methods such as GC [113], GC-MS [114, 115], near-infrared spectroscopy SDE [116], and HPLC [117, 118], etc. These traditional detection methods have been widely adopted in the analysis of rice quality, and some of them have been recognized as standard methods for assessing and evaluating rice quality due to their superior accuracy and validity [119, 120].

Sensory analysis, particularly as a smell assessment method, serves as a direct and effective means of evaluating changes in aroma profiles during the inspection of rice quality. It offers unique insights into aroma characteristics and is considered to be the most intuitive detection method. The human nose has a remarkable response, with a limit of detection for one particular molecule around 10^{-19} mol [121]. This response makes sensory evaluation a reliable tool for detecting aroma-active compounds in rice aging. Accordingly, the sensory assessment method is mainly utilized for discriminating aromatic rice from non-aromatic ones [111]. Nevertheless, sensory evaluation performed by skilled panelists is inevitably influenced by external factors, such as psychological, and environmental conditions [122]. There are significant differences in repeated evaluations and odor responses among different individuals. Sensory fatigue can also lead to low classification accuracy and limited assessment efficiency over time. In addition, sensory evaluation is highly subjective rather than quantitative analysis. Therefore, to enhance the reliability of sensory evaluation, it is crucial to train professionals, establish consistent description lexicons, and define reference standards for aroma compounds in rice. Specifically, proper training ensures that panelists can consistently identify and describe aromas, reducing variability in assessment. Besides, creating a standardized vocabulary for describing rice aromas helps ensure that evaluations are consistent and comparable across different panelists and over time. Moreover, using reference standards allows panelists to calibrate their sense of smell against known concentrations of specific aroma compounds, enhancing the accuracy and reproducibility of their evaluations. In summary, standardizing the evaluation process and improving the overall accuracy of sensory assessment can make sensory analysis a more robust tool for rice quality inspection. Despite its challenges, sensory evaluation remains indispensable for its direct and nuanced insights into the aroma profiles of rice, providing valuable information that complements instrumental analysis methods.

Physical and chemical indicators can directly and objectively reflect the changes in rice quality, making this a more in-depth research field. Various physical and chemical indices reflecting the degree of rice aging mainly include fatty acid value, viscosity, hardness, moisture, protein, and amylose contents. Among them, the free fatty acids in rice are produced by the hydrolysis or oxidation of lipids. Changes in lipids are considered to be the most obvious changes in the process of rice aging. The value of fatty acid is determined by sodium hydroxide titration with ethanol as an extraction

agent. This method needs to crush the rice samples into a fine powder to facilitate the extraction process, and then the crushed sample is mixed with ethanol to extract the free fatty acids. Subsequently, the mixture is the filtered to separate the solid residues from the liquid extract containing the fatty acids. Finally, the fatty acid content is measured by titrating the ethanol extract with a sodium hydroxide solution until a color change indicates the end point. Based on this complicated procedures, there are some problems, such as complicated operation (each needing precision and careful handling), strong subjectivity (the titration end point is often determined by a color change), a large amount of organic reagents (i.e., ethanol and sodium hydroxide), and temperature sensitivity (changes in temperature during grinding and extraction), that have a substantial impact on the fatty acid value. Given these challenges, there is a need for improved methods that can provide more reliable and consistent results with less dependency on subjective judgment and environmental conditions. Advances in automated titration systems and alternative extraction techniques could help mitigate these issues, leading to more accurate assessments of rice quality based on fatty acid values.

Instrumental analysis methods are crucial in detecting the aging process of rice by analyzing aroma compounds and establishing correlations with physical and chemical indices to reflect changes in rice quality. Despite their accuracy and comprehensive data, these detection methods face several challenges including time-consuming, complex sample pretreatment, destructive nature, expensive equipment and technical skills, and lack of on-site or online evaluation [123]. In detail, instrumental methods often require lengthy sample preparation and analysis times, making them impractical for rapid and large-scale quality inspections. Moreover, the preparation of samples can be labor-intensive and involve multiple steps, increasing the potential for errors and variability in results. Most importantly, some methods may alter or destroy the sample, making it unsuitable for further analysis or use. High costs associated with the equipment and the need for skilled operators make these methods less accessible for routine use. Currently, traditional sample pretreatment methods employed for the extraction of VOCs in rice mainly include steam distillation extraction (SDE), supercritical fluid extraction (SFE), headspace adsorption extraction (HSSE), and SPME. Among them, SDE is effective for extracting a wide range of VOCs. However, it can lead to the decomposition and generation of some VOCs during the feature extraction. Moreover, long extraction times make it impractical for large-scale inspection of rice quality in the aging process. SFE is an efficient extraction method that preserves the integrity of volatile compounds. But it require expensive equipment and skilled operators. Meanwhile, they are limited by the expensive equipment together with technical skills [124]. To address these challenges, several advancements in sample pretreatment and instrumental analysis, such as developing automated and integrated systems for streamline sample preparation

and analysis, designing portable and use-friendly devices for on-site and online evaluation, enhancing non-destructive methods for preserving samples, and implementing comprehensive training programs for operators can be pursued. By addressing these challenges, instrumental analysis methods can become more practical and widely applicable for routine quality assessments in rice aging. This will enhance the ability to monitor and maintain rice quality more effectively, ensuring better outcomes for producers and consumers alike.

These conventional methods, such as sensory evaluation, physical and chemical indices, and instrumental analysis, offer high precision and reliability in rice quality assessment. However, they come with significant drawbacks, including the need for sophisticated equipment, trained personnel, and time-consuming procedures. Consequently, there is a growing interest in developing rapid, cost-effective and non-destructive techniques to complement these traditional methods. With advancements in technology, novel sensitive and precision instruments have emerged, facilitating rapid and online inspection of rice quality. These modern approaches aim to overcome the limitations of traditional methods by offering quicker, more efficient, and non-destructive analysis. According to the above investigation, the E-nose, with its ability to mimic human olfaction and provide quick results, holds promise for routine quality control in the rice industry. The E-nose stands out as a valuable alternative to traditional detection methods due to several advantages. The E-nose simplifies the analysis process by eliminating the need for labor-intensive and complex sample preparation. Compared to traditional instruments, the E-nose offers a faster and more straightforward means of identifying rice aroma profiles. Moreover, the E-nose is adept at detecting changes in the chemical composition during rice aging, making it an effective tool for identifying different rice varieties and assessing the degree of aging based on comprehensive aroma profiles rather than solely relying on quantitative analysis of VOCs.

Above all, while conventional methods remain essential for high-precision and reliable rice quality assessment, the development and integration of rapid, cost-effective, and non-destructive techniques like the E-nose offer significant benefits. The E-nose's ability to streamline the analysis process, provide quick results, and detect subtle changes in aroma profiles makes it a valuable complement to traditional methods. As technology continues to advance, the E-nose and similar innovations hold promise for enhancing quality control and ensuring the superior quality of rice products in the industry.

1.5 Conclusions and objectives

While the development of an E-nose equipped with advanced pattern recognition methods and prediction models has shown promising results for rice quality inspection,

its application remains primarily in the laboratory stage. Several factors hinder the practical deployment of E-noses in the rice industry. The operation of MOS-based gas sensors at elevated temperatures (200-400 ℃) leads to the adsorption of VOC molecules on the sensor surface. This elevated temperature can cause the decomposition of some compounds like aldehydes, which are crucial for accurate aroma profiling. In addition, high temperature induce the thermal growth of MOS crystallites, affecting the stability and performance of the sensors over time. This can result in unreliable measurements and reduced sensor lifespan. Consequently, there is a need to develop high-performance MOS-based gas sensors that can reliably detect and monitor characteristic VOCs at low working temperatures, especially at room temperature. Lower operating temperatures would prevent the decomposition of VOCs and maintain sensor stability, thereby enhancing measurement reliability. Meanwhile, a simple sensor structure and low power consumption ultimately ensure a potential application for their utilization in high-performance gas devices for the analysis of rice quality.

In this regard, recent research suggests that the incorporation of oxygen vacancies can be extensively taken to elevate the gas-sensing performance, represented by the reduction of working temperature and the improvement of response, of MOS-based gas sensors [125-127]. The generation of oxygen vacancies with different concentrations is principally accompanied by a series of changes in physicochemical properties, e.g. bond breaking and remodeling, lattice distortion, and shifting of Fermi energy levels. Most importantly, the incorporation of oxygen vacancies can effectively decrease the bandgap of MOS materials, requiring less energy for electron excitation to the conduction band. This leads to a lower operating temperature for effective sensor performance. Moreover, oxygen vacancies create a metastable lattice structure by disrupting the stable lattice due to the loss of oxygen atoms, which enhances the adsorption activity of the sensing materials. The presence of oxygen vacancies facilitates better electron transfer efficiency, contributing to a more responsive and sensitive sensor.

Currently, literature reports that gas sensors based on metal oxides such as tungsten oxide, cerium oxide, and zinc stannate have been used as one of detection units in E-nose systems, specifically for detecting aldehydes (i.e., hexanal, octanal, nonanal, etc.) [128, 129], alcohols (1-octen-3-ol, linalool, benzyi alcohol, etc.) [130-132], and ketones (i.e., 2-butanone, 2-heptanone, 2-undecaone, etc.) [133, 134] as volatile organic compounds. However, these biomarkers, characterized by long carbon chains and large molecular structures, exist in low concentrations in the gas phase. Consequently, in the detection these characteristic biomarkers, these metal oxide-based gas sensors exhibit inadequate sensitivity, necessitating high working temperatures and resulting in high detection limits in the ppm range. With the above-mentioned strategy in mind, high-performance gas sensors based on metal oxides can be developed through the

corporation of oxygen vacancies.

Currently, there are two main ways to incorporate oxygen vacancies into MOSs. The first method involves directly incorporating oxygen vacancies during the material synthesis process by controlling the nucleation and growth stages of crystals. By adjusting parameters such as reaction temperature, time, and precursor ratio, the valence of metal ions in metal oxides can be regulated, leading to the loss of lattice oxygen. For example, Ye et al. synthesized oxygen-vacancy-rich ultrathin $W_{18}O_{49}$ nanowires up to several micrometers in length through a straightforward one-step solution-phase method employing tungsten chloride (WCl_6) as the metal source and ethanol as the solvent [135]. Characterization results revealed the concentration of oxygen vacancies in metal oxides could be precisely regulated by adjusting key reaction parameters. The second method involves post-treatment of pre-synthesized metal oxide precursors. This method typically involves at least two steps. The stoichiometric metal oxides should be first synthesized, then the obtained powders are annealed under different atmospheres (i.e., hydrogen, argon, etc.) and temperatures, which is the most widely utilized method for incorporating oxygen vacancies into MOS. For instance, Wang et al. fabricated $ZnSnO_3$ nanowires through a hydrothermal method followed by post-thermal-annealing under a hydrogen atmosphere [136]. Theoretical calculations revealed a significant decrease in the bandgap of $ZnSnO_3$ with the incorporation of oxygen vacancies. A moderated concentration of oxygen vacancies was found to provide more donor sites for carriers to occupy in the crystals. While these methods can incorporate oxygen vacancies into metal oxides, they still have some drawbacks such as slow particle growth and insufficient oxygen vacancies in the crystal structure. This makes it challenging to accurately control the concentration of oxygen vacancies and has a limited effect on improving the gas-sensing properties of MOS-based gas sensors, especially those operating at room temperature. Apart from that, novel technologies including solution precursor plasma spray and vacuum plasma spray have recently been developed for the efficient deposition of MOS-based gas-sensing coatings with highly porous structures and highly concentrated oxygen vacancies. These technologies allow precise control over the concentration of oxygen vacancies in metal oxides by adjusting key parameters like hydrogen flow and deposition pressure [137-139].

Based on the inherent characteristics of the above metal oxides, extensive literature indicates that hydrothermal, post-treatment and plasma spraying are effective and straightforward routes to incorporate oxygen vacancies into tungsten oxide, cerium oxide, and zinc stannate, respectively [140-142]. In this thesis, the aforementioned methods have been employed for the fabrication of metal oxides with newly designed structures and different concentrations of oxygen vacancies to significantly enhance their gas-sensing performance, mainly reflected in reducing the working temperature and elevating the response, towards various characteristic biomarkers generated in rice

aging. This work aims to provide a theoretical and technical foundation for the development of high-performance E-nose devices intended for large-scale inspections of rice quality throughout the aging process during storage.

References

[1] S. Choi, H. Jun, J. Bang, S.H. Chung, Y. Kim, B.S. Kim, Y. Kim, B.S. Kim, H. Kim, L.R. Beychat, J.H. Ryu. Behaviour of Aspergillus flavus and Fusarium graminearum on rice as affected by degree of milling, temperature, and relative humidity during storage. Food Microbiology, 46 (2015) 307-313. https://doi.org/10.1016/j.fm.2014.08.019.

[2] D.K. Verma, P.P. Srivastav. Bioactive compounds of rice (Oryza sativa L.): Review on paradigm and its potential benefit in human health. Trends in Food Science & Technology, 97 (2020) 355-365. https://doi.org/10.1016/j.tifs.2020.01.007.

[3] W. Tsuzuki, Y. Suzuki, S. Yamada, S. Kano, H. Ohnishi, T. Fujimoto, A. Horigane. Effect of oxygen absorber on accumulation of free fatty acids in brown rice and whole grain wheat during storage. LWT-Food Science and Technology, 58 (2014) 222-229. https://doi.org/10.1016/j.lwt.2014.02.015.

[4] X. Li, L. Wu, X. Geng, X.H. Xia, X.H. Wang, Z.J. Xu, Q. Xu. Deciphering the environmental impacts on rice quality for different rice cultivated areas. Rice, 11 (2018) 1-10. https://doi.org/10.1186/s12284-018-0198-1.

[5] A. Saikrishna, S. Dutta, V. Subramanian, J.A. Moses, C. Anandharamakrishnan. Aging of rice: A review. Journal of Cereal Science, 81 (2018) 161-170. https://doi.org/10.1016/j.jcs.2018.04.009.

[6] Z.K. Zhou, X.F. Wang, X. Si, C. Blanchard, P. Strappe. The aging mechanism of stored rice: A concept model from the past to the present. Journal of Stored Products Research, 64 (2015) 80-87. https://doi.org/10.1016/j.jspr.2015.09.004.

[7] T.A. Kaminski, A. Brackmann, L.P. da Silva, A.M. Nicoletti, B.S. Roberto. Changes in culinary, viscoamylographic and sensory characteristics during rice storage at different temperatures. Journal of Stored Products Research, 53 (2013) 37-42. https://doi.org/10.1016/j.jspr.2013.02.003.

[8] N. Thanathornvarakul, J. Anuntagool, K. Tananuwong. Aging of low and high amylose rice at elevated temperature: Mechanism and predictive modeling. Journal of Cereal Science, 70 (2016) 155-163. https://doi.org/10.1016/j.jcs.2016.06.004.

[9] Z. Zhou, K. Robards, S. Helliwell, C. Blanchard. Aging of stored rice: Changes in chemical and physical attributes. Journal of Cereal Science, 35 (2002) 65-78. https://doi.org/10.1006/jcrs.2001.0418.

[10] T. Tikapunya, R.J. Henry, H. Smyth. Evaluating the sensory properties of unpolished Australian wild rice. Food Research International, 103 (2018) 406-414. https://doi.org/10.1016/j.foodres.2017.10.037.

[11] C. Chusak, J.A.Y. Ying, J.L. Zhien, P. Pasukamonset, C.J. Henry, S. Ngamukote, S. Adisakwattana. Impact of Clitoria ternatea (butterfly pea) flower on in vitro starch

digestibility, texture and sensory attributes of cooked rice using domestic cooking methods. Food Chemistry, 295 (2019) 646-652. https://doi.org/10.1016/j.foodchem.2019.05.157.

[12] P. Wu, C.F. Li, Y.M. Bai, S.Y. Yu, X.A. Zhang. A starch molecular basis for aging-induced changes in pasting and textural properties of waxy rice. Food Chemistry, 284 (2019) 270-278. https://doi.org/10.1016/j.foodchem.2019.01.065.

[13] Y.J. Zhong, X.Y. Xiang, T.T. Chen, P. Zou, Y.F. Liu, J.P. Ye, S.J. Luo, J.Y. Wu, C.M. Liu. Accelerated aging of rice by controlled microwave treatment. Food Chemistry, 323 (2020) 126853. https://doi.org/10.1016/j.foodchem.2020.126853.

[14] C.E. Park, Y.S. Kim, K.J. Park, B.K. Kim. Changes in physicochemical characteristics of rice during storage at different temperatures. Journal of Stored Products Research, 48 (2012) 25-29. https://doi.org/10.1016/j.jspr.2011.08.005.

[15] B.B. Guan, J.W. Zhao, H.J. Jin, H. Lin. Determination of rice storage time with colorimetric sensor array. Food Analytical Methods, 10 (2017) 1054-1062. https://doi.org/10.1007/s12161-016-0664-6.

[16] T. Chen, F.H. Wu, J.J. Guo, M.Q. Ye, H. Hu, J. Guo, X.Q. Liu. Effects of glutinous rice protein components on the volatile substances and sensory properties of Chinese rice wine. Journal of the Science of Food and Agriculture, 100 (2020) 3297-3307. https://doi.org/10.1002/jsfa.10343.

[17] M. Baietto, A.D. Wilson. Electronic-nose applications for fruit identification, ripeness and quality grading. Sensors, 15 (2015) 899-931. https://doi.org/10.3390/s150100899.

[18] X.Q. Hu, L. Lu, Z.L. Guo, Z.W. Zhu. Volatile compounds, affecting factors and evaluation methods for rice aroma: A review. Trends in Food Science & Technology, 97 (2020) 136-146. https://doi.org/10.1016/j.tifs.2020.01.003.

[19] Q. Xia, Y.F. Li. Ultra-high pressure effects on color, volatile organic compounds and antioxidants of wholegrain brown rice (oryza sativa L.) during storage: A comparative study with high-intensity ultrasound and germination pretreatments. Innovative Food Science & Emerging Technologies, 45 (2018) 390-400. https://doi.org/10.1016/j.ifset.2017.12.003.

[20] H. Takemitsu, M. Amako, Y. Sako, K. Shibakusa, K. Kita, S. Kitamura, H. Inui. Analysis of volatile odor components of superheated steam-cooked rice with a less stale flavor. Food Science and Technology Research, 22 (2016) 771-778. https://doi.org/10.3136/fstr.22.771.

[21] Z.Q. Hu, H. Yang, M. Chaima, C.Y. Fang, L. Lu, X.Q. Hu, B. Du, Z.W. Zhu, J.Y. Huang. A visualization and quantification method to evaluate the water-absorbing characteristics of rice. Food Chemistry, 331 (2020) 127050. https://doi.org/10.1016/j.foodchem.2020.127050.

[22] J.W. Gardner, P.N. Bartlett. A brief history of electronic noses. Sensors and

Actuators B: Chemical, 18 (1994) 210-211. https://doi.org/10.1016/0925-4005(94)87085-3.

[23] M. Ghasemi-Varnamkhasti, M. Aghbashlo. Electronic nose and electronic mucosa as innovative instruments for real-time monitoring of food dryers. Trends in Food Science & Technology, 38 (2014) 158-166. https://doi.org/10.1016/j.tifs.2014.05.004.

[24] P. Handa, B. Singh. Electronic nose and their application in food industries. Food Science Research Journal, 7 (2016) 314-318. https://doi.org/10.15740/HAS/FSRJ/7.2/314-318.

[25] J. Majchrzak, W. Wojnowski, T. Dymerski, J. Gebicki, J. Namiesnik. Electronic noses in classification and quality control of edible oils: A review. Food Chemistry, 246 (2018) 192-201. https://doi.org/10.1016/j.foodchem.2017.11.013.

[26] M.T. Kalit, K. Markovic, S. Kalit, N. Vahcic, J. Havranek. Application of electronic nose and electronic tongue in the dairy industry. Mljekarstvo, 64 (2014) 228-244. https://doi.org/10.15567/mljekarstvo.2014.0402.

[27] A.D. Wilson. Diverse applications of electronic-nose technologies in agriculture and forestry. Sensors, 13 (2013) 2295-2348. https://doi.org/10.1007/s11633-019-1212-9.

[28] S. Dragonieri, G. Pennazza, P. Carratu, O. Resta. Electronic nose technology in respiratory diseases. Lung, 195 (2017) 157-165. https://doi.org/10.1007/s00408-017-9987-3.

[29] T. Wasilewski, D. Migon, J. Gebicki, W. Kamysz. Critical review of electronic nose and tongue instruments prospects in pharmaceutical analysis. Analytica Chimica Acta, 1077 (2019) 14-29. https://doi.org/10.1016/j.aca.2019.05.024.

[30] H. Rahimzadeh, M. Sadeghi, M. Ghasemi-Varnamkhasti, S.A. Mireei, M. Tohidi. On the feasibility of metal oxide gas sensor based electronic nose software modification to characterize rice aging during storage. Journal of Food Engineering, 245 (2019) 1-10. https://doi.org/10.1016/j.jfoodeng.2018.10.001.

[31] F.C. Lidon. Lipid, carbohydrate, and protein accumulation in Mn-treated rice. Journal of Plant Nutrition, 25 (2002) 769-780. https://doi.org/10.1081/PLN-120002958.

[32] G. Atungulu, M. Miura, E. Atungulu, Y. Satou, K. Suzuki. Activity of gaseous phase steam distilled propolis extracts on peroxidation and hydrolysis of rice lipids. Journal of Food Engineering, 80 (2007) 850-858. https://doi.org/10.1016/j.jfoodeng.2006.08.007.

[33] M.H.G. Gomes, L.E. Kurozawa. Improvement of the functional and antioxidant properties of rice protein by enzymatic hydrolysis for the microencapsulation of linseed oil. Journal of Food Engineering, 267 (2020) 109761. https://doi.org/10.1016/j.jfoodeng.2019.109761.

[34] Y.L. Liu, X.H. Li, X.L. Zhou, J. Yu, F.X. Wang, J.H. Wang. Effects of glutaminase deamidation on the structure and solubility of rice glutelin. LWT-Food Science and Technology, 44 (2011) 2205-2210. https://doi.org/10.1016/j.lwt.2011.05.011.

[35] B. Yuan, C.J. Zhao, M. Yan, D.C. Huang, D.J. McClements, Z.G. Huang, C.J. Cao. Influence of gene regulation on rice quality: Impact of storage temperature and humidity on flavor profile. Food Chemistry, 283 (2019) 141-147. https://doi.org/10.1016/j.foodchem.2019.01.042.

[36] K. Wakte, R. Zanan, V. Hinge, K. Khandagale, A. Nadaf, R. Henry. Thirty-three years of 2-acetyl-1-pyrroline, a principal basmati aroma compound in scented rice (oryza sativa L.): A status review. Journal of the Science of Food and Agriculture, 97 (2017) 384-395. https://doi.org/10.1002/jsfa.7875.

[37] D.S. Yang, K.S. Lee, O.Y. Jeong, K.J. Kim, S.J. Kays. Characterization of volatile aroma compounds in cooked black rice. Journal of Agricultural and Food Chemistry, 56 (2008) 235-240. https://doi.org/10.1021/jf072360c.

[38] H. Lin, Z.X. Man, W.C. Kang, B.B. Guan, Q.S. Chen, Z.L. Xue. A novel colorimetric sensor array based on boron-dipyrromethene dyes for monitoring the storage time of rice. Food Chemistry, 268 (2018) 300-306. https://doi.org/10.1016/j.foodchem.2018.06.097.

[39] K.L. Liu, S. Zhao, Y. Li, F.S. Chen. Analysis of volatiles in brown rice, germinated brown rice, and selenised germinated brown rice during storage at different vacuum levels. Journal of the Science of Food and Agriculture 98 (2018) 2295-2301. https://doi.org/10.1002/jsfa.8718.

[40] J. Sung, B.K. Kim, B.S. Kim, Y. Kim. Mass spectrometry-based electric nose system for assessing rice quality during storage at different temperatures. Journal of Stored Products Research, 59 (2014) 204-208. https://doi.org/10.1016/j.jspr.2014.02.009.

[41] S. Choi, H.S. Seo, K.R. Lee, S. Lee, J. Lee, J. Lee. Effect of milling and long-term storage on volatiles of black rice (Oryza sativa L.) determined by headspace solid-phase microextraction with gas chromatography-mass spectrometry. Food Chemistry, 276 (2019) 572-582. https://doi.org/10.1016/j.foodchem.2018.10.052.

[42] E.T. Champagne, J.F. Thompson, K.L. Bett-Garber, R. Mutters, J.A. Miller, E. Tan. Impact of storage of freshly harvested paddy rice on milled white rice flavor. Cereal Chemistry, 81 (2004) 444-449. https://doi.org/10.1094/CCHEM.2004.81.4.444.

[43] A. Loutfi, S. Coradeschi, G.K. Mani, P. Shankar, J.B.B. Rayappan. Electronic noses for food quality: A review. Journal of Food Engineering, 144 (2015) 103-111. https://doi.org/10.1016/j.jfoodeng.2014.07.019.

[44] Y. Zhu, H.P. Lv, W.D. Dai, L. Guo, J.F. Tan, Y. Zhang, F.L. Yu, C.Y. Shao, Q.H. Peng, Z. Lin. Separation of aroma components in Xihu Longjing tea using simultaneous distillation extraction with comprehensive two-dimensional gas

chromatography-time-of-flight mass spectrometry. Separation and Purification Technology, 164 (2016) 146-154. https://doi.org/10.1016/j.seppur.2016.03.028.

[45] Y. Deng, Y. Zhong, W.J. Yu, J. Yue, Z.M. Liu, Y.R. Zheng, Y.Y. Zhao. Effect of hydrostatic high pressure pretreatment on flavor volatile profile of cooked rice. Journal of Cereal Science, 58 (2013) 479-487. https://doi.org/10.1016/j.jcs.2013.09.010.

[46] V.R. Hinge, H.B. Patil, A.B. Nadaf. Aroma volatile analyses and 2AP characterization at various developmental stages in basmati and non-basmati scented rice (Oryza sativa L.) cultivars. Rice, 9 (2016) 38-59. https://doi.org/10.1186/s12284-016-0113-6.

[47] S.M. Lee, H.J. Lim, J.W. Chang, B.S. Hurh, Y.S. Kim. Investigation on the formations of volatile compounds, fatty acids, and γ-lactones in white and brown rice during fermentation. Food Chemistry, 269 (2018) 347-354. https://doi.org/10.1016/j.foodchem.2018.07.037.

[48] K. Kaikavoosi, T.D. Kad, R.L. Zanan, A.B. Nadaf. 2-Acetyl-1-pyrroline augmentation in scented indica rice (Oryza sativa L.) varieties through delta (1)-pyrroline-5-carboxylate synthetase (P5CS) gene transformation. Applied Biochemistry and Biotechnology, 177 (2015) 1466-1479. https://doi.org/10.1007/s12010-015-1827-4.

[49] Y. Yoshizaki, H. Yamato, K. Takamine, H. Tamaki, K. Ito, Y. Sameshima. Analysis of volatile compounds in shochu koji, sake koji, and steamed rice by gas chromatography-mass spectrometry. Journal of the Institute of Brewing, 116 (2010) 49-55. https://doi.org/10.1002/j.2050-0416.2010.tb00397.x.

[50] S. Cho, E. Nuijten, R.L. Shewfelt, S.J. Kays. Aroma chemistry of African Oryza glaberrima and Oryza sativa rice and their interspecific hybrids. Journal of the Science of Food and Agriculture, 94 (2014) 727-735. https://doi.org/10.1002/jsfa.6329.

[51] L.G. Dias, A. Hacke, S.F. Bergara, O.V. Villela, L.R.B. Mariutti, N. Bragagnolo. Identification of volatiles and odor-active compounds of aromatic rice by OSME analysis and SPME/GC-MS. Food Research International, 142 (2021) 110206. https://doi.org/10.1016/j.foodres.2021.110206.

[52] S.Q. Song, L. Yuan, X.M. Zhang, K. Hayat, H.N. Chen, F. Liu, Z.B. Xiao, Y.W. Niu. Rapid measuring and modelling flavour quality changes of oxidised chicken fat by electronic nose profiles through the partial least squares regression analysis. Food Chemistry, 141 (2013) 4278-4288. https://doi.org/10.1016/j.foodchem.2013.07.009.

[53] K. Persaud, G. Dodd. Analysis of discrimination mechanisms in the mammalian olfactory system using a model nose. Nature, 299 (1982) 352-355. https://doi.org/10.1038/299352a0.

[54] H. Cheng, Z.H. Qin, X.F. Guo, X.S. Hu, J.H. Wu. Geographical origin identification of propolis using GC-MS and electronic nose combined with principal component analysis. Food Research International, 51 (2013) 813-822. https://doi.org/10.1016/j.foodres.2013.01.053.

[55] V. Kodogiannis. Application of an electronic nose coupled with fuzzy-wavelet network for the detection of meat spoilage. Food and Bioprocess Technology, 10 (2017) 730-749. https://doi.org/10.1007/s11947-016-1851-6.

[56] M. Son, T.H. Park. The bioelectronic nose and tongue using olfactory and taste receptors: Analytical tools for food quality and safety assessment. Biotechnology Advances, 36 (2018) 371-379. https://doi.org/10.1016/j.biotechadv.2017.12.017.

[57] A. Jiarpinijnun, K. Osako, U. Siripatrawan. Visualization of volatomic profiles for early detection of fungal infection on storage Jasmine brown rice using electronic nose coupled with chemometrics. Measurement, 157 (2020) 107561. https://doi.org/10.1016/j.measurement.2020.107561.

[58] Y. Shi, L.L. Wang, Y. Fang, H.P. Wang, H.L. Tao, F. Pei, P. Li, B.C. Xu, Q.H. Hu. A comprehensive analysis of aroma compounds and microstructure changes in brown rice during roasting process. LWT-Food Science and Technology, 98 (2018) 613-621. https://doi.org/10.1016/j.lwt.2018.09.018.

[59] X.Z. Zheng, Y.B. Lan, J.M. Zhu, J. Westbrook, W.C. Hoffmann, R.E. Lacey. Rapid identification of rice samples using an electronic nose. Journal of Bionics Engineering, 6 (2009) 290-297. https://doi.org/10.1016/S1672-6529(08)60122-5.

[60] S. Xu, Z.Y. Zhou, L.H. Tian, H.Z. Lu, X.W. Luo, Y.B. Lan. Study of the similarity and recognition between volatiles of brown rice plant hoppers and rice stem based on the electronic nose. Computers and Electronics in Agriculture, 152 (2018) 19-25. https://doi.org/10.1016/j.compag.2018.06.047.

[61] K. Timsorn, Y. Lorjaroenphon, C. Wongchoosuk. Identification of adulteration in uncooked Jasmine rice by a portable low-cost artificial olfactory system. Measurement, 108 (2017) 67-76. https://doi.org/10.1016/j.measurement.2017.05.035.

[62] T. Feng, H.N. Zhuang, R. Ye, Z.Y. Jin, X.M. Xu, Z.J. Xie. Analysis of volatile compounds of Mesona Blumes gum/rice extrudates via GC-MS and electronic nose. Sensors and Actuators B: Chemical, 160 (2011) 964-973. https://doi.org/10.1016/j.snb.2011.09.013.

[63] L. Lu, S.P. Deng, Z.W. Zhu, S.Y. Tian. Classification of rice by combining electronic tongue and nose. Food Analytical Methods, 8 (2014) 1893-1902. https://doi.org/10.1007/s12161-014-0070-x.

[64] N. Sinelli, S. Benedetti, G. Bottega, M. Riva, S. Buratti. Evaluation of the optimal cooking time of rice by using FT-NIR spectroscopy and an electronic nose. Journal of Cereal Science, 44 (2006) 137-143. https://doi.org/10.1016/j.jcs.2006.05.002.

[65] S. Srivastava, G. Mishra, H.N. Mishra. Fuzzy controller based E-nose classification of Sitophilus oryzae infestation in stored rice grain. Food Chemistry, 283 (2019) 604-610. https://doi.org/10.1016/j.foodchem.2019.01.076.

[66] A. Gliszczynska-Swiglo, J. Chmielewski. Electronic nose as a tool for monitoring the authenticity of food. A review. Food Analytical Methods, 10 (2017) 1800-1816. https://doi.org/10.1007/s12161-016-0739-4.

[67] A. Sanaeifar, H. ZakiDizaji, A. Jafari, M. de la Guardia. Early detection of contamination and defect in foodstuffs by electronic nose: A review. Trends in Analytical Chemistry, 97 (2017) 257-271. https://doi.org/10.1016/j.trac.2017.09.014.

[68] M.M. Ali, N. Hashim, S. Abd Aziz, O. Lasekan. Principles and recent advances in electronic nose for quality inspection of agricultural and food products. Trends in Food Science & Technology, 99 (2020) 1-10. https://doi.org/10.1016/j.tifs.2020.02.028.

[69] S. Jiang, Y. Liu. Gas sensor for volatile compounds analysis in muscle foods: A review. Trends in Analytical Chemistry, 126 (2020) 115877. https://doi.org/10.1016/j.trac.2020.115877.

[70] A.H. Abdullah, A.H. Adom, A.Y.M. Shakaff, M.N. Ahmad, A. Zakaria, N.A. Fikri, O. Omar. An electronic nose system for aromatic rice classification. Sensor Letters, 9 (2011) 850-855. https://doi.org/10.1166/sl.2011.1629.

[71] X.G. Ying, W. Liu, G.H. Hui, J. Fu. E-nose based rapid prediction of early mouldy grain using probabilistic neural networks. Bioengineered, 6 (2015) 222-226. https://doi.org/10.1080/21655979.2015.1022304.

[72] H. Jiang, T. Liu, P.H. He, Q.S. Chen. Quantitative analysis of fatty acid value during rice storage based on olfactory visualization sensor technology. Sensors and Actuators B: Chemical, 309 (2020) 127816. https://doi.org/10.1016/j.snb.2020.127816.

[73] L.X. Han, H.B. Ren, L. Meng. Flavor substances in rice: Formation and change. Chinese Agricultural Science Bulletin, 38 (2022) 126-134. https://doi.org/10.11924/j.issn.1000-6850.casb2022-0166.

[74] W. Routray, K. Rayaguru. 2-Acetyl-1-pyrroline: A key aroma component of aromatic rice and other food products. Food Reviews International, 34 (2018) 539-565. https://doi.org/10.1080/87559129.2017.1347672.

[75] N.E. Okpalaa, Z.W. Moa, M.Y. Duana, X.R. Tanga. The genetics and biosynthesis of 2-acetyl-1-pyrroline in fragrant rice. Plant Physiology and Biochemistry, 135 (2019) 272-276. https://doi.org/10.1016/j.plaphy.2018.12.012.

[76] P. Schieberle. Primary odorants in popcorn. Journal of Agricultural and Food Chemistry, 39 (1991) 1141-1144. https://doi.org/10.1021/jf00006a030.

[77] X. Wei, D.D. Handoko, L. Pather, L. Methven, J.S. Elmore. Evaluation of 2-acetyl-

1-pyrroline in foods, with an emphasis on rice flavor. Food Chemistry, 232 (2017) 531-544. https://doi.org/10.1016/j.foodchem.2017.04.005.

[78] O. Norkaew, P. Boontakham, K. Dumri, A.N.L. Noenplab, P. Sookwong, S. Mahatheeranont. Effect of post-harvest treatment on bioactive phytochemicals of Thai black rice. Food Chemistry, 217 (2017) 98-105. https://doi.org/10.1016/j.foodchem.2016.08.084.

[79] P. Udomkun, B. Innawong, K. Niruntasuk. The feasibility of using an electronic nose to identify adulteration of Pathumthani 1 in Khaw Dok Mail 105 rice during storage. Journal of Food Measurement and Characterization, 12 (2018) 2515-2523. https://doi.org/10.1007/s11694-018-9868-3.

[80] L. Yu, M.S. Turner, M. Fitzgerald, J.R. Stokes, J. Witt. Review of the effects of different processing technologies on cooked and convenience rice quality. Trends in Food Science & Technology, 59 (2017) 124-138. https://doi.org/10.1016/j.tifs.2016.11.009.

[81] R.R. Ma, Y.Q. Tian, L. Chen, Z.Y. Jin. Impact of cooling rates on the flavor of cooked rice during storage. Food Bioscience, 35 (2020) 100563. https://doi.org/10.1016/j.fbio.2020.100563.

[82] S.V. Mathure, N. Jawali, R.J. Thengane, A.B. Nadaf. Comparative quantitative analysis of headspace volatiles and their association with BADH2 marker in non-basmati scented, basmati and non-scented rice (Oryza sativa L.) cultivars in India. Food Chemistry, 142 (2014) 383-391. https://doi.org/10.1016/j.foodchem.2013.07.066.

[83] S. Mahatheeranont, S. Keawsa-ard, K. Dumri. Quantification of the rice aroma compound. 2-Acetyl-1-pyrroline, in uncooked Khao Dawk Mali 105 brown rice. Journal of Agricultural and Food Chemistry, 49 (2001) 773-779. https://doi.org/10.1021/jf000885y.

[84] H. Hopfer, F. Jodari, F. Negre-Zakharov, P.L. Wylie, S.E. Ebeler. HS-SPME-GC-MS/MS method for the rapid and sensitive quantitation of 2-acetyl-1-pyrroline in single rice kernels. Journal of Agricultural and Food Chemistry, 64 (2016) 4114-4120. https://doi.org/10.1021/acs.jafc.6b00703.

[85] Y. Suzuki, K. Ise, C.Y. Li, I. Honda, Y. Iwai, U. Matsukura. Volatile components in stored rice Oryza sativa (L.) of varieties with and without lipxygenase-3 in seeds. Journal of Agricultural and Food Chemistry, 47 (1999) 1119-1124. https://doi.org/10.1021/jf980967a.

[86] C.J. Zhao, J.Q. Xie, L. Li, C.J. Cao. Comparative transcriptomic analysis in the paddy rice under storage and identification of differentially regulated genes in response to high temperature and humidity. Journal of Agricultural and Food Chemistry, 65 (2017) 8145-8153. https://doi.org/10.1021/acs.jafc.7b03901.

[87] Y.R. Wang, J. Ha. Determination of hexanal in rice using an automated dynamic

headspace sampler coupled to a gas chromatograph-mass spectrometer. Journal of Chromatographic Science, 51 (2012) 446-452. https://doi.org/10.1093/chromsci/bms161.

[88] D.S. Yang, K.S. Lee, S.J. Kays. Characterization and discrimination of premium-quality, waxy, and black-pigmented rice based on odor-active compounds. Journal of the Science of Food and Agriculture, 90 (2010) 2595-2601. https://doi.org/10.1002/jsfa.4126.

[89] M.A. Monsoor, A. Proctor. Volatile component analysis of commercially milled head and broken rice. Journal of Food Science, 69 (2004) C632-C636. https://doi.org/10.1111/j.1365-2621.2004.tb09911.x.

[90] Q.X. Hu, C.Y. Fang, W.X. Zhang, L. Lu, Z.L. Guo, S.M. Li, M.X. Chen. Change in volatiles, soluble sugars and fatty acids of glutinous rice, japonica rice and indica rice during storage. LWT-Food Science and Technology, 174 (2023) 114416. https://doi.org/10.1016/j.lwt.2022.114416.

[91] C.P. Yi, H. Zhu, L.T. Tong, S.M. Zhou, R.H. Yang, M. Niu. Volatile profiles of fresh rice noodles fermented with pure and mixed cultures. Food Research International, 119 (2019) 152-160. https://doi.org/10.1016/j.foodres.2019.01.044.

[92] Q.Y. Zhao, L. Yousaf, Y. Xue, Q. Shen. Changes in flavor of fragrant rice during storage under different conditions. Journal of the Science of Food and Agriculture, 100 (2020) 3435-3444. https://doi.org/10.1002/jsfa.10379.

[93] D.S. Yang, R. Shewfelt, K. Lee, S.J. Kays. Comparison of odor-active compounds from six distinctly different rice flavor types. Journal of Agricultural and Food Chemistry, 56 (2008) 2780-2787. https://doi.org/10.1021/jf072685t.

[94] J.C.T. Concepcion, S. Ouk, A. Riedel, M. Calingacion, D. Zhao, M. Ouk, M.J. Garson, M.A. Fitzgerald. Quality evaluation, fatty acid analysis and untargeted profiling of volatiles in Cambodian rice. Food Chemistry, 240 (2018) 1014-1021. https://doi.org/10.1016/j.foodchem.2017.08.019.

[95] A.R. Monforte, D. Jacobson, A.C. Silva Ferreira. Chemiomics: Network reconstruction and kinetics of Port wine aging. Journal of Agricultural and Food Chemistry, 63 (2015) 2576-2581. https://doi.org/10.1021/jf5055084.

[96] N. Wang, S. Chen, Z.M. Zhou. Age-dependent characterization of volatile organic compounds and age discrimination in Chinese rice wine using an untargeted GC/MS-based metabolomic approach. Food Chemistry, 325 (2020) 126900. https://doi.org/10.1016/j.foodchem.2020.126900.

[97] Z. Zeng, H. Zhang, J.Y. Chen, T. Zhang, R. Matsunaga. Direct extraction of volatiles of rice during cooling using solid-phase microextraction. Cereal Chemistry, 84 (2007) 423-427. https://doi.org/10.1094/CCHEM-84-5-0423.

[98] D.K. Verma, P.P Srivastav. A paradigm of volatile aroma compounds in rice and their product with extraction and identification methods: A comprehensive review.

Food Research International, 130 (2020) 108924. https://doi.org/10.1016/j.foodres.2019.108924.

[99] C.C. Grimm, E.T. Champagne, S.W. Lloyd, M. Easson, B. Condon, A. McClung. Analysis of 2-acetyl-1-pyrroline in rice by HSSE/GC/MS. Cereal Chemistry, 88 (2011) 271-277. https://doi.org/10.1094/CCHEM-09-10-0136.

[100] K.S. Youn, H.S. Chung. Optimization of the roasting temperature and time for preparation of coffee-like maize beverage using the response surface methodology. LWT-Food Science and Technology, 46 (2012) 305-310. https://doi.org/10.1016/j.lwt.2011.09.014.

[101] Z.C. Zheng, C. Zhang, K.W. Liu, Q.Q. Liu. Volatile Organic Compounds, Evaluation Methods and Processing Properties for Cooked Rice Flavor. Rice, 15 (2022) 53. https://doi.org/10.1186/s12284-022-00602-3.

[102] J.J. Liang, Y.Q. Lin, S.B. Wu, C. Liu, M. Lei, C. Zeng. Enhancing the quality of bio-oil and selectivity of phenols compounds from pyrolysis of anaerobic digested rice straw. Bioresource Technology, 2015 (2015) 220-223. https://doi.org/10.1016/j.biortech.2015.01.056.

[103] Y.W. Niu, Z.M. Yao, Z.B. Xiao, G.Y. Zhu, J.C. Zhu, J.Y. Chen. Sensory evaluation of the synergism among ester odorants in light aroma-type liquor by odor threshold, aroma intensity and flash GC electronic nose. Food Research International, 113 (2018) 102-114. https://doi.org/10.1016/j.foodres.2018.01.018.

[104] R.J. Bryant, A.M. Mcclung. Volatile profiles of aromatic and non-aromatic rice cultivars using SPME/GC-MS. Food Chemistry, 124 (2011) 501-513. https://doi.org/10.1016/j.foodchem.2010.06.061.

[105] S. Sansenya, Y. Hua, S. Chumanee. The correlation between 2-Acetyl-1-pyrroline content, biological compounds and molecular characterization to the aroma intensities of Thai local rice. Journal of Oleo Science, 67 (2018) 893-904. https://doi.org/10.5650/jos.ess17238.

[106] B.S. Kang, J.E. Lee, H.J. Park. Qualitative and quantitative prediction of volatile compounds from initial amino acid profiles in Korean rice wine (makgeolli) model. Journal of Food Science, 79 (2014) 1106-1116. https://doi.org/10.1111/1750-3841.12489.

[107] M. Serafico, F. Sevilla. Differentiation of Philippine aromatic rice varieties using electronic nose. Sensors & Transducers, 28 (2018) 19-25.

[108] G.L. Li, X.Y. Zheng, D.M. Huang, X. Chen, F.B. Meng, M. Lin. Effect of Co-60 gamma-irradiation on physicochemical properties of adlay during storage period. International Journal of Food Engineering, 15 (2019) 1-11. https://doi.org/10.1515/ijfe-2018-0329.

[109] J.Y. Shi, T. Zhang, S.F. Geng, F.Q. Liang, T.T. Wang. Effect of accumulated temperature on flavour and microbial diversity of japonica rice during storage.

Journal of Stored Products Research, 92 (2021) 101779. https://doi.org/10.1016/j.jspr.2021.101779.

[110]M. Limpawattana, R.L. Shewfelt. Flavor lexicon for sensory descriptive profiling of different rice types. Journal of Food Science, 75 (2010) 199-205. https://doi.org/10.1111/j.1750-3841.2010.01577.x.

[111]L. Lu, C.Y. Fang, Z.Q. Hu, X.Q. Hu, Z.W. Zhu. Grade classification model tandem BpNN method with multi-metal sensor for rice eating quality evaluation. Sensors and Actuators B: Chemical, 281 (2019) 22-27. https://doi.org/10.1016/j.snb.2018.10.062.

[112]T.F. Chen, C.L. Chen. Analysing the freshness of intact rice grains by colour determination of peroxidase activity. Journal of the Science of Food and Agriculture, 83 (2003) 1214-1218. https://doi.org/10.1002/jsfa.1528.

[113]S. Gu, W. Chen, Z.H. Wang, Y.J. Huo. Rapid detection of Aspergillus spp. infection levels on milled rice by headspace-gas chromatography ion-mobility spectrometry (HS-GC-IMS) and E-nose. LWT-Food Science and Technology, 132 (2020) 109758. https://doi.org/10.1016/j.lwt.2020.109758.

[114]L.H. Xie, S.Q. Tang, X.J. Wei, G.A. Jiao, Z.H. Sheng, P.S. Hu. An optimized analysis of 2-acetyl-1-pyrroline content diversity in the core collection of aromatic rice germplasm (Oryza sativa L.). Cereal Chemistry, 96 (2019) 698-707. https://doi.org/10.1002/cche.10166.

[115]J.F. Peng, Y. Yang, Y.P. Zhou, C.H. Hocart, H. Zhao, Y.W. Hu, F. Zhang. Headspace solid-phase microextraction coupled to gas chromatography-mass spectrometry with selected ion monitoring for the determination of four food flavoring compounds and its application in identifying artificially scented rice. Food Chemistry, 313 (2020) 126136. https://doi.org/10.1016/j.foodchem.2019.126136.

[116]P.S. Sampaio, A. Castanho, A.S. Almeida, J. Oliveira, C. Brites. Identification of rice flour types with near-infrared spectroscopy associated with PLS-DA and SVM methods. European Food Research and Technology, 246 (2020) 527-537. https://doi.org/10.1007/s00217-019-03419-5.

[117]K. Seebunrueng, P. Phosiri, R. Apitanagotinon, S. Srijaranai. A new environment-friendly supramolecular solvent-based liquid phase microextraction coupled to high performance liquid chromatography for simultaneous determination of six phenoxy acid herbicides in water and rice samples. Microchemical Journal, 152 (2020) 104418. https://doi.org/10.1016/j.microc.2019.104418.

[118]N. Hussain, D.W. Sun, H.B. Pu. Classical and emerging non-destructive technologies for safety and quality evaluation of cereals: A review of recent applications. Trends in Food Science & Technology, 91 (2019) 598-608. https://doi.org/10.1016/j.tifs.2019.07.018.

[119]S. Lohumi, S. Lee, H. Lee, B.K. Cho. A review of vibrational spectroscopic techniques for the detection of food authenticity and adulteration. Trends in Food Science & Technology, 46 (2013) 85-98. https://doi.org/10.1016/j.tifs.2015.08.003.

[120]M.C. Custodio, R.P. Cuevas, J. Ynion, A.G. Laborte, M.L. Velasco, M. Demont. Rice quality: How is it defined by consumers, industry, food scientists, and geneticists? Trends in Food Science & Technology, 92 (2019) 122-137. https://doi.org/10.1016/j.tifs.2019.07.039.

[121]K. Wilkie, M. Wootton, J.E. Paton. Sensory testing of Australian fragrant, imported fragrant, and non-fragrant rice aroma. International Journal of Food Properties, 7 (2004) 27-36. https://doi.org/10.1081/JFP-120022493.

[122]N. Bhattacharyya, S. Seth, B. Tudu, P. Tamuly, A. Jana, D. Ghosh, R. Bandyopadhyay, M. Bhuyan. Monitoring of black tea fermentation process using electronic nose. Journal of Food Engineering, 80 (2007) 1146-1156. https://doi.org/10.1016/j.jfoodeng.2006.09.006.

[123]M. Peris, L. Escuder-Gilabert. Electronic noses and tongues to assess food authenticity and adulteration. Trends in Food Science & Technology, 58 (2016) 40-54. https://doi.org/10.1016/j.tifs.2016.10.014.

[124]M. Mohd Ali, N. Hashim, S.K. Bejo, R. Shamsudin. Laser-induced back-scattering imaging for classification of seeded and seedless watermelons. Computers and Electronics in Agriculture, 140 (2017) 311-316. https://doi.org/10.1016/j.compag.2017.06.010.

[125]A. Naldoni, M. Allieta, S. Santangelo, M. Marelli, F. Fabbri, S. Cappelli, C.L. Bianchi, R. Psaro, V. Dal Santo. Effect of nature and location of defects on bandgap narrowing in black TiO_2 nanoparticles. Journal of the American Chemical Society, 134 (2012) 7600-7603. https://doi.org/10.1021/ja3012676.

[126]W.J. Ding, D.D. Liu, J.J. Liu, J.T. Zhang. Oxygen defects in nanostructured metal-oxide gas sensors: Recent advances and challenges. Chinese Journal of Chemistry, 38 (2020) 1832-1846. https://doi.org/10.1002/cjoc.202000341.

[127]K.A. Adegoke, N.W. Maxakato. Porous metal oxide electrocatalytic nanomaterials for energy conversion: Oxygen defects and selection techniques. Coordination Chemistry Reviews, 457 (2022) 214389. https://doi.org/10.1016/j.ccr.2021.214389.

[128]S.Q. Song, X.M. Zhang, K. Hayat, C.S. Jia, S.G. Xia, F. Zhong, Z.B. Xiao, H.X. Tian, Y.W. Niu. Correlating chemical parameters of controlled oxidation tallow to gas chromatography-mass spectrometry profiles and e-nose responses using partial least squares regression analysis. Sensors and Actuators B: Chemical, 147 (2010) 660-668. https://doi.org/10.1016/j.snb.2010.03.055.

[129]W.M. Cao, L. Lin, Y.W. Niu, Z.B. Xiao, X.Z Fang. Characterization of aroma volatiles in camellia seed oils (camellia oleifera abel.) by HS-SPME/GC/MS and

electronic nose combined with multivariate analysis. Food Science and Technology Research, 22 (2016) 497-505. https://doi.org/10.3136/fstr.22.497.

[130]K.L.A. Kumar, S. Durgajanani, B.G. Jeyaprakash, J.B.B. Rayappan. Nanostructured ceria thin film for ethanol and trimethylamine sensing. Sensors and Actuators B: Chemical, 177 (2013) 19-26. https://doi.org/10.1016/j.snb.2012.10.107.

[131]G. Neri, A. Bonavita, G. Rizzo, S. Galvagno, S. Capone, P. Siciliano. A study of the catalytic activity and sensitivity to different alcohols of CeO_2-Fe_2O_3 thin films. Sensors and Actuators B: Chemical, 111-112 (2005) 78-83. https://doi.org/10.1016/j.snb.2005.06.045.

[132]Q.Y. Zhou, C.Y. Zhou, Y.H. Zhou, W. Hong, S.H. Zou, X.Q. Gong, J.J. Liu, L.P. Xiao, J. Fan. More than oxygen vacancies: a collective crystal- plane effect of CeO_2 in gas-phase selective oxidation of benzyl alcohol. Catalysis Science & Technology, 9 (2019) 2960-2967. https://doi.org/10.1039/c9cy00395a.

[133]N.H. Hanh, L.V. Duy, C.M. Hung, C.T. Xuan, N.V. Duy, N.D. Hoa. High-performance acetone gas sensor based on Pt-Zn_2SnO_4 hollow octahedra for diabetic diagnosis. Journal of Alloys and Compounds, 886 (2021) 161284. https://doi.org/10.1016/j.jallcom.2021.161284.

[134]Z. Yuan, C. Yang, Y. Li, F. Meng and J. Duan. Ppb-level 2-butanone gas sensor based on CTAB-assisted synthesis of small-size ZnSnO nano cube. IEEE Sensors Journal, 22 (2022) 20156-20164. https://doi.org/10.1109/JSEN.2022.3199397.

[135]G.C. Xi, S.X. Ouyang, P. Li, J.H. Ye, Q. Ma, N. Su, H. Bai, C. Wang. Ultrathin $W_{18}O_{49}$ nanowires with diameters below 1 nm: Synthesis, near-infrared absorption, photoluminescence, and photochemical reduction of carbon dioxide. Angewandte Chemie-International Edition, 51 (2012) 2395-2399. https://doi.org/10.1002/anie.201107681.

[136]Y.C. Wang, J.M. Wu. Effect of controlled oxygen vacancy on H_2 production through the piezocatalysis and piezophototronics of ferroelectric R3C $ZnSnO_3$ nanowires. Adv. Funct. Mater. 30 (2020) 1907619. https://doi.org/10.1002/adfm.201907619.

[137]C. Zhang, J. Wang, X. Geng. Tungsten oxide coatings deposited by plasma spray using powder and solution precursor for detection of nitrogen dioxide gas. Journal of Alloys and Compounds, 668 (2016) 128-136. https://doi.org/10.1016/j.jallcom.2016.01.219.

[138]V. Ambardekar, T. Bhowmick, P.P. Bandyopadhyay. Understanding on the hydrogen detection of plasma sprayed tin oxide/tungsten oxide (SnO_2/WO_3) sensor. International Journal of Hydrogen Energy, 47 (2022) 15120-15131. https://doi.org/10.1016/j.ijhydene.2022.03.005.

[139]C. Zhang, G.F. Liu, K.W. Liu, K.D. Wu. ZnO_{1-x} coatings deposited by atmospheric

plasma spraying for room temperature ppb-level NO_2 detection. Applied Surface Science, 528 (2020) 147041. https://doi.org/10.1016/j.apsusc.2020.147041.

[140]C. Wang, L.L. Guo, N. Xie, X.Y. Kou, Y.F. Sun, X.H. Chuai, S.M. Zhang, H.W. Song, Y. Wang, G.Y. Lu. Enhanced nitrogen oxide sensing performance based on tin-doped tungsten oxide nanoplates by a hydrothermal method. Journal of Colloid and Interface Science, 512 (2018) 740-749. https://doi.org/10.1016/j.jcis.2017.09.068.

[141]X.Q. Wei, K. Li, X.Y. Zhang, Q. Tong, J.W. Ji, Y.D. Cai, B. Gao, W.X. Zou, L. Dong. CeO_2 nanosheets with anion-induced oxygen vacancies for promoting photocatalytic toluene mineralization: Toluene adsorption and reactive oxygen species. Applied Catalysis B: Environmental, 317 (2022) 121694. https://doi.org/10.1016/j.apcatb.2022.121694.

[142]A.H. Navidpour, M. Fakhrzad. Photocatalytic activity of Zn_2SnO_4 coating deposited by air plasma spraying. Applied Surface Science Advances, 6 (2021) 100153. https://doi.org/10.1016/j.apsadv.2021.100153.

Chapter 2 Experimental methods

2.1 Research contents

With the aforementioned objective, this thesis develops room-temperature gas sensors based on metal oxides through a combination of chemical synthesis routes, such as hydrothermal methods, and surface modification techniques, including the loading noble metals (e.g., ruthenium), the construction of heterojunctions, and structural regulation. Subsequently, utilizing relevant characterization methods, the enhanced gas-sensing performance of the fabricated metal oxide-based gas sensors operating at room temperature is thoroughly explored.

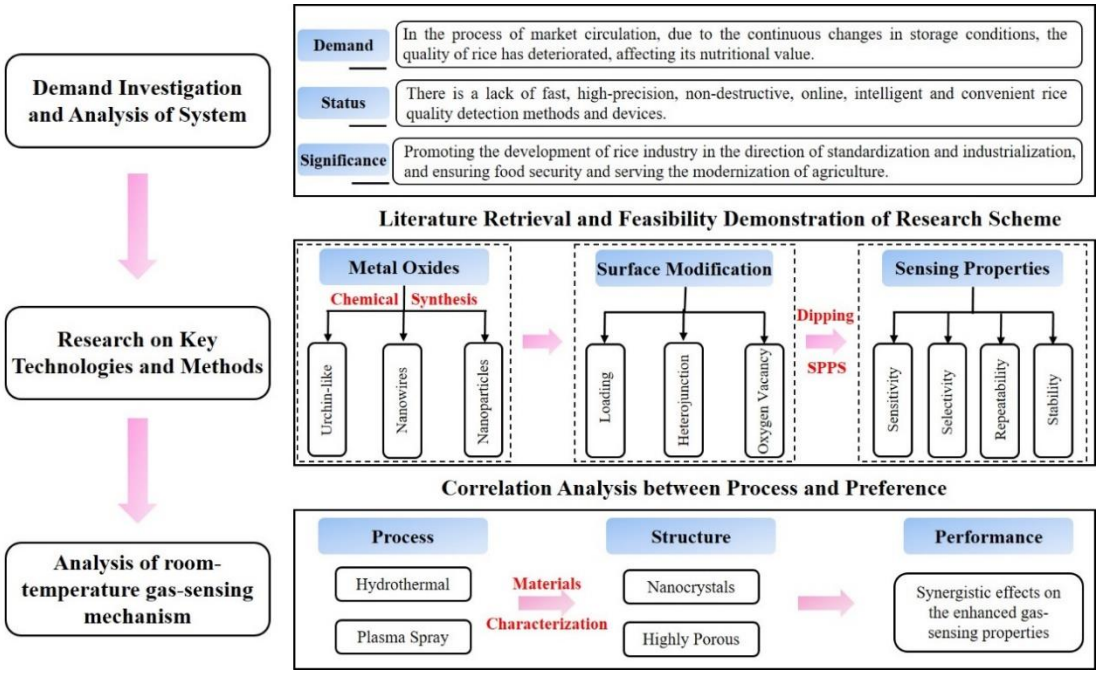

Fig. 2.1 Technical approach employed in this thesis.

The methodology employed in this study is illustrated in Fig. 2.1. The initial step involves a thorough examination of the E-nose requirements, verifying the viability of the research scheme through a comprehensive review of relevant literature. Subsequently, the focus shifts to key technologies and methods. This stage prominently includes the synthesis of MOSs with diverse morphologies and structures using chemical synthesis routes. Furthermore, a range of surface modification strategies are employed to enhance the surface characteristics of the synthesized MOSs. These MOSs or their precursors are then applied to the sensor substrate using dipping or plasma spraying techniques. The objective is to assess the room-temperature gas-sensing attributes of the fabricated gas sensors, including response, selectivity, repeatability,

stability, in detecting the target odors generated from rice aging.

2.2 Materials characterizations

The main instruments utilized in this study are illustrated in Tab. 2.1.

Tab. 2.1 Main instruments utilized in the experiments.

Instrument	Abbreviation	Model	Function
Field emission-scanning electron microscope	FE-SEM	S4800	Morphologies
High-resolution transmission electron microscopy	HRTEM	Tecnai G2 F30 S-TWIN	Structures
X-ray diffraction	XRD	Bruker D8 Advance	Phase compositions
X-ray photoelectron spectroscope	XPS	ESCALAB250Xi	Chemical states
Surface analysis and pore size analyzer	BET	Autosorb IQ3	Specific surface areas
Micro infrared spectrometer	FTIR	670-IR + 610-IR	Functional groups
Ultraviolet/visible/near-infrared spectrophotometer	UV-Vis	Cary 5000	Absorption spectra
Raman spectrometer	Raman	DXRxi	Composition distribution

2.3 Gas-sensing performance investigation

The gas-sensing performance of the fabricated gas sensors is investigated using a four-channel gas sensing testing instrument (HCRK-SD101, Wuhan Huachuang Ruike Technology Co., China) under controlled laboratory conditions with a temperature of 25±5 ℃ and a relative humidity of 30%±10%.

2.3.1 Measurement of gas sensors

2.3.1.1 Detection of VOCs

The schematic diagram of the experimental setup is shown in Fig. 2.2a. High-purity air (79%N_2+21%O_2) is used as the carrier gas. This air is bubbled through the VOC liquids to generate the target gas, which is then diluted before being exposed to the surface of the metal oxides. The theoretical concentration of the target gas is

reported in parts per million (ppm) and calculated using Eq. 2-1 [1, 2]. The concentration can be adjusted by varying the flow rates using mass flow controllers (MFCs, FS-200CV, Germany). In this setup, as illustrated in Fig. 2.2a, the flow (x) of the target gas with a theoretical concentration is controlled by one MFC, while the flow (y) of high-purity air (Nanjing Special Gas Factory Co., Ltd., China) is controlled by another MFC. The concentration of the target gas in ppm is defined as: theoretical concentration*x)/(x+y) [3]. This is achieved by separately adjusting the flows of the MFCs. For experiments investigating the effect of relative humidity, an additional flow (z) of high-purity air is controlled by another MFC and bubbled through deionized water. The relative humidity in % is defined as: z/(x+y+z)*%. By adjusting these flows, the desired concentration of the target gas and the relative humidity can be precisely controlled during the experiments.

$$\text{Concentration (ppm)} = \frac{10^6 \times Vapor\ pressure}{760} \tag{2-1}$$

The vapor pressure in mm Hg of the target VOC utilized in this thesis can be found in the Chemical Book [4].

2.3.1.2 Detection of rice sample

As shown in Fig. 2.2b, two rice varieties (japonica rice and indica rice) are purchased from a local supermarket in Yangzhou, China. For each test, 30 g of rice samples are sealed in a glass bottle with a volume of 50 mL. The storage temperature and duration are crucial parameters for evaluating the practical application of the fabricated sensors. In this experiment, the temperature of the glass bottle is maintained using a thermostat water bath. Subsequently, the testing process is consistent with the procedures outlined in Section 2.3.1. High-purity air flows through the sample container, and the gas-sensing testing device automatically records the changes in resistance. This setup allows for the monitoring of the VOCs emitted from the rice samples.

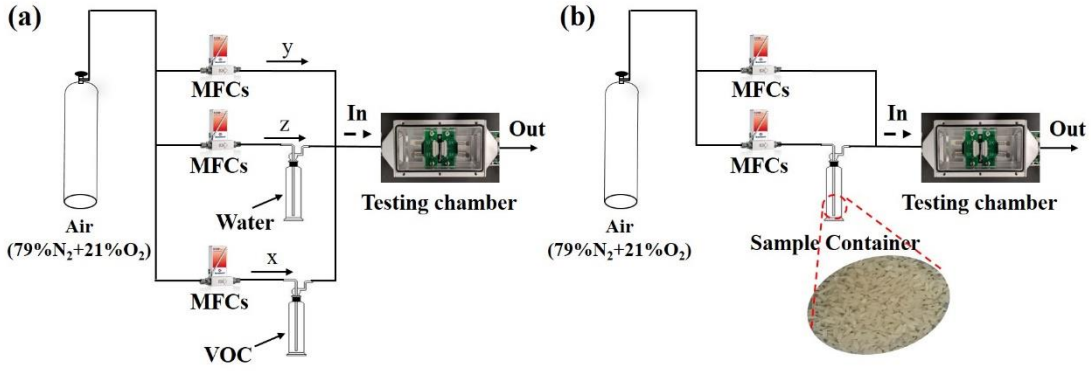

Fig. 2.2 Schematic illustrations of the gas-sensing testing system for the detection of (a) VOC liquid and (b) aroma profiles generated from rice aging.

2.3.2 Gas-sensing attributes

The most important aspects of gas-sensing performance investigation for MOS-based gas sensors are the 4 "S", namely response, selectivity, speed (response/recovery time), and stability. In addition, other commonly used gas-sensing attributes, including the limit of detection (LOD), reproducibility, repeatability, etc., are also discussed in this thesis.

2.3.2.1 Response

Response, one of the most crucial indicators for MOS-based gas sensors, refers to the sensor's ability to detect the target VOC. In this thesis, metal oxides like $W_{18}O_{49}$, CeO_2, and $ZnSnO_3$, which are all n-type MOS, are used to detect target VOCs such as nonanal, linalool, 2-undecanone, which are reducing gases. Unless otherwise specified, the sensor response in this work is expressed as R_a/R_g, where R_a represents the resistance in the purified air, and R_g refers to the resistance after reaching a steady state when exposed to an air/VOC mixture.

2.3.2.2 Selectivity

Selectivity, also known as cross-sensitivity, refers to the sensor's ability to distinguish the target VOC in complex environments. It is generally expressed by the ratio of the sensor response to the target gas and other interfering gases. Due to environmental complexity, selectivity is essential for applications tracking multiple VOCs, as cross-sensitivity can reduce the repeatability and reliability of sensor devices. Ideal gas sensors should exhibit a higher response and superior selectivity toward the detected VOC over other interfering gases, including both reducing and oxidizing ones.

2.3.2.3 Response and recovery times

Response and recovery times are commonly defined as the time required for the sensor's electrically transduced signals to change to 90% of the saturation value after introducing or switching off the target VOC [5]. If the baseline continuously drifts significantly or recovery is much lower than 80-90%, the device can be classified as unrecoverable, as it fails to meet the repeatability and long-term stability requirements for practical applications.

2.3.2.4 Long-term stability

Long-term stability is a key factor in demonstrating the reliability of the sensors. Researchers generally describe the remaining percentage of gas-sensing performance after certain periods. Long-term stability provides information regarding the optimal time required for calibration to compensate for gas-sensing performance reduction.

2.3.2.5 Repeatability

The repeatability of a gas sensor serves as a crucial metric for assessing its reliability in consistently generating signals when exposed to a specific concentration of gaseous analytes. This evaluation involves conducting consecutive performance investigations under the same testing conditions. If the results exhibit minimal errors or deviations, it indicates that the gas sensor possesses superior repeatability.

2.3.2.6 Limit of detection

The limit of detection (LOD) of the sensors can be obtained using the International Union of Pure and Applied Chemistry (IUPAC) standard method. According to the IUPAC, LOD is determined when the signal is over three times the noise level in the system based on the equation. Specifically, the standard deviation (σ) obtained by testing 100 points without any target gases, and the slope (s) of the linear fitting equation are utilized to calculate the theoretical LOD of a sensor based on the equation ($LOD=3\sigma/s$) [6, 7].

2.4 Conclusions

This chapter introduces the research contents adopted in this study and provides a detailed description of the equipment and methods used for characterizing the microstructure of gas-sensing materials and investigating the room-temperature gas-sensing performance of the developed sensors. Finally, the gas-sensing attributes (i.e., response, selectivity, speed, stability, etc.) are evaluated to assess the sensor's performance.

References

[1] Daneshkhah, S. Vij, A.P. Siegel, M. Agarwal. Polyetherimide/carbon black composite sensors demonstrate selective detection of medium-chain aldehydes including nonanal. Chemical Engineering Journal, 383 (2020) 123104. https://doi.org/10.1016/j.cej.2019.123104.

[2] G. Liu, E. Froudarakis, J.M. Patel, M.Y. Kochukov, B. Pekarek, P.J. Hunt, M. Patel, K. Ung, C.H. Fu, J. Jo, H.K. Lee, A.S. Tolias, B.R. Arenkiel. Target specific functions of EPL interneurons in olfactory circuits. Nature Communications, 10 (2019) 3369. https://doi.org/10.1038/s41467-019-11354-y.

[3] C. Zhang, J.Y. Xu, H.P. Li, H.L. Liao. Role of ruthenium incorporation on room-temperature nonanal sensing properties of Ru-loaded urchin-like $W_{18}O_{49}$ hierarchical nanostructure. Sensors and Actuators B: Chemical, 353 (2022) 131096. https://doi.org/10.1016/j.snb.2021.131096.

[4] https://www.chemicalbook.com/ProductIndex_EN.aspx.

[5] Y.S. Xu, T.T. Ma, L.L. Zheng, L. Sun, X.H. Liu, Y.Q. Zhao, J. Zhang. Rational design of Au/Co_3O_4-functionalized $W_{18}O_{49}$ hollow heterostructures with high sensitivity and ultralow limit for triethylamine detection. Sensors and Actuators B: Chemical, 284 (2019) 202-212. https://doi.org/10.1016/j.snb.2018.12.119.

[6] Z. Wang, L.Z. Huang, X.F. Zhu, X. Zhou, L.F. Chi. An ultrasensitive organic semiconductor NO_2 sensor based on crystalline TIPS-pentacene films. Advanced Materials, 29 (2017) 1703192. https://doi.org/10.1002/adma.201703192.

[7] Z.L. Song, Z.R. Wei, B.C. Wang, Z. Luo, S.M. Xu, W.K. Zhang, H.X. Yu, M. Li, Z. Huang, J.F. Zang, F. Yi, H. Liu. Sensitive room-temperature H_2S gas sensors employing SnO_2 quantum wire/reduced graphene oxide nanocomposites. Chemistry of Materials, 28 (2016) 1205-1212. https://doi.org/10.1021/acs.chemmater.5b04850.

Chapter 3 One-pot hydrothermal synthesis of Ru-loaded urchin-like $W_{18}O_{49}$ hierarchical nanostructures for nonanal detection

3.1 Introduction

As stated in Section 1.3.2.2, nonanal, a medium-chain aldehyde, is produced from the oxidation and hydrolysis of lipids during rice aging [1, 2]. Its concentration serves as a valuable indicator of rice quality. Developing sensors for nonanal sensing is crucial due to their potential applications in assessing the quality of rice. Nonanal is considered a selective biomarker for inspecting rice quality [3, 4]. The concentration of nonanal increases as fatty acid oxidize with aging [5], making the determination of nonanal content an ideal method for assessing rice quality.

Due to their advantages of simple operation, fast response, and high cost-effectiveness [6-8], metal oxide semiconductors, such as SnO_2 [9] and WO_3 [10], are widely employed as sensing materials for the analysis of nonanal. Among them, tungsten oxides are classified into stoichiometric WO_3 and nonstoichiometric WO_{3-x}. Compared to WO_3, sub-stoichiometric WO_{3-x} has garnered special attention due to its excellent physicochemical stability and extensive oxygen vacancies [11, 12]. Among the reported WO_{3-x} variants, $W_{18}O_{49}$ can exist in a pure and stable state form [13, 14], making it a promising gas-sensing material. However, $W_{18}O_{49}$-based gas sensors often exhibit limitations, including low response, high operating temperatures, and insufficient detection limit for the target gas, hindering their further development in the analysis of rice quality [15-17]. To dramatically improve the gas-sensing performance of pure $W_{18}O_{49}$, various optimization strategies, such as novel structure design [15, 18], composite formation [16, 19], and noble metal loading [20], have been widely adopted. Nevertheless, it is reported that gas sensors based on these materials generally operate at elevated temperatures ranging from 200 to 400 ℃. Xu et al. pointed out that the storage temperature is a crucial factor affecting nonanal content because the sensor response remains proportional to rice aging [21]. Consequently, to accurately detect changes in nonanal content, the gas sensor should be operated at room temperature, which helps prevent the degradation of gas sensors and the decomposition of the target gas molecules. However, sensors typically show low response at room temperature, limiting their application in the inspection of rice quality. In addition, most gas sensors based on MOSs are not highly sensitive to nonanal because of its chemical inertness, particularly at room temperature.

In this chapter, ruthenium (Ru)-loaded urchin-like $W_{18}O_{49}$ hierarchical nanostructures with highly concentrated oxygen vacancies and higher specific surface

areas are synthesized through a one-step hydrothermal method followed by calcination. The unique urchin-like morphology provides abundant adsorption sites for redox reactions, along with additional catalytic sites, enhancing the material's gas-sensing capabilities. It is anticipated that the Ru-loaded $W_{18}O_{49}$ will demonstrate superior room-temperature gas-sensing properties towards nonanal compared to pure $W_{18}O_{49}$. The incorporation of Ru is primarily responsible for these enhanced gas-sensing properties, enabling the detection of nonanal at ppm levels. During storage or market circulation, indica rice and japonica rice tend to deteriorate in sensory quality, leading to undesirable aroma profiles. Hence, the practicability of the optimal gas sensor in evaluating rice quality is tested by storing rice samples at different temperatures (25, 50, and 75 ℃). This approach aims to assess the sensor's effectiveness in monitoring the quality of rice over time under various storage conditions.

3.2 Experimental details

3.2.1 Chemicals

All chemicals used in this study are analytical reagents, and they are directly used without further purification. Detailed information regarding the formula, purity, and manufacturer is illustrated in Tab. 3.1.

Tab. 3.1 Chemical reagents used in this chapter.

Chemicals	Formula	Manufacturer	Purity
Tungsten chloride	WCl_6	Shanghai Aladdin Biochemical Technology Co., Ltd.	99%
Ruthenium chloride anhydrous	$RuCl_3$	Beijing Warwick Chemical Co., Ltd.	Ru 47%
Methanol	CH_3OH	Shanghai Aladdin Biochemical Technology Co., Ltd.	99.5%
Nonanal	$C_9H_{18}O$	Shanghai Aladdin Biochemical Technology Co., Ltd.	96%

3.2.2 Synthesis of Ru-loaded urchin-like $W_{18}O_{49}$ hierarchical nanostructures

Ru-loaded urchin-like $W_{18}O_{49}$ hierarchical nanostructures with highly concentrated oxygen vacancies were synthesized using a straightforward hydrothermal method followed by calcination treatment, as schematically demonstrated in Fig. 3.1.

In brief, 0.375 g of tungsten hexachloride (WCl_6) was dispersed in 80 mL methanol. The mixture was stirred continuously at room temperature to form a homogeneous solution. To incorporate Ru into the $W_{18}O_{49}$ nanostructures, varying amounts of ruthenium chloride ($RuCl_3$) were added to the WCl_6 solution. The mass percentage of Ru relative to $W_{18}O_{49}$ were set at 0.0%, 0.5%, 1.0%, and 2.0%, respectively. The mixed solutions were vigorously stirred for 1 hour. Subsequently, each solution was transferred into a Teflon-lined stainless steel autoclave with a volume of 100 mL. The autoclaves were then subjected to a hydrothermal reaction at 160 ℃ for 24 hours. After the hydrothermal reaction, the autoclaves were allowed to cool naturally to room temperature. The resulting solid precipitates were collected by centrifugation at 4000 rpm, followed by rinsing alternately with distilled water and absolute ethanol three times. The cleaned solid powders were dried using a vacuum freeze dryer for at least 36 hours. The dried powders were then annealed at 300 ℃ for 2 hours in a nitrogen atmosphere, with a heating rate of 2 ℃/min, to obtain the Ru-loaded $W_{18}O_{49}$ powders. The synthesized powders were labeled based on the Ru content as follows: 0.0%Ru-$W_{18}O_{49}$, 0.5%Ru-$W_{18}O_{49}$, 1.0%Ru-$W_{18}O_{49}$, and 2.0%Ru-$W_{18}O_{49}$, respectively.

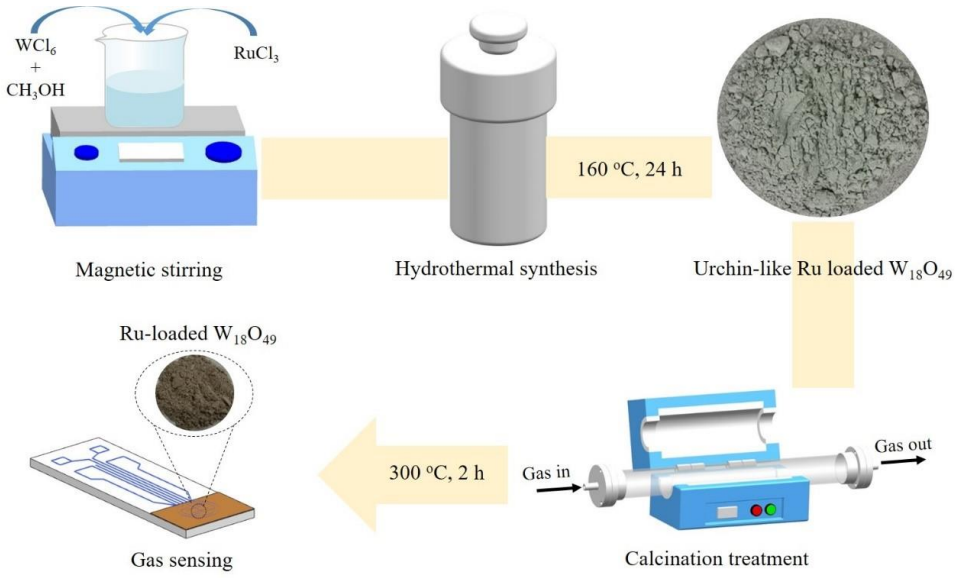

Fig. 3.1 Synthesis procedures of Ru-loaded urchin-like $W_{18}O_{49}$ hierarchical nanostructure-based gas-sensing materials.

3.2.3 Fabrication and measurement of gas sensors

The alumina sensor substrates (dimensions: 6x30 mm), which were screen-printed with platinum (Pt) electrodes, were cleaned using deionized water and ethanol. The gap between the gear-shaped electrodes was 0.42 nm. The synthesized Ru-loaded W18O49 powders were mixed with deionized water and ground to create a uniform paste. The homogeneous paste was then used to coat the surfaces of the cleaned sensor substrates

via a dip-coating process. After complete drying, the coated substrates were placed inside a testing chamber to dry and prepare for gas-sensing performance evaluations. In this study, nonanal was selected as the target gas, and its theoretical concentration was calculated by Eq. 2-1, where the vapor pressure of nonanal at 25 ℃ is 0.26 mm Hg [22].

3.3 Results and Discussion

3.3.1 Structural characterization

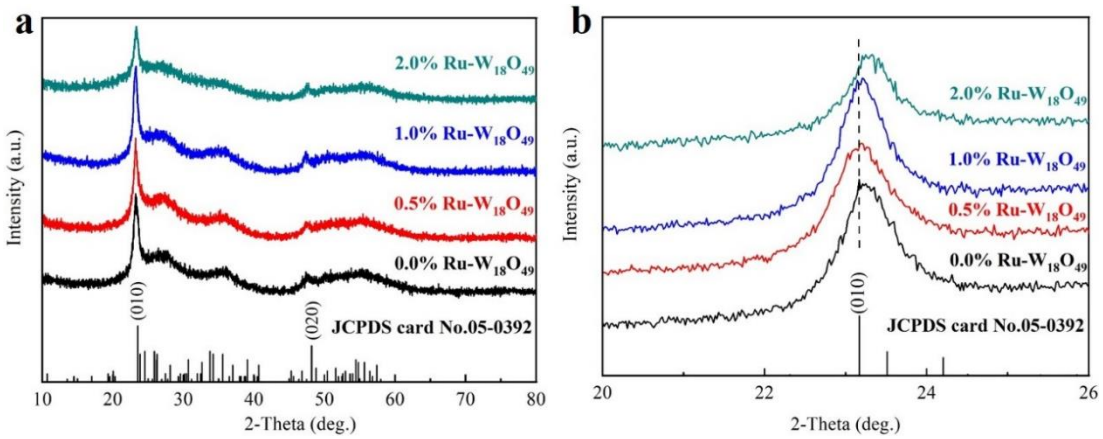

Fig. 3.2 (a) XRD patterns of pure and 0.5%-2.0%Ru-loaded $W_{18}O_{49}$ hierarchical nanostructure-based gas-sensing materials, (b) the slow scan of (010) peak.

The phase compositions of pure and Ru-loaded $W_{18}O_{49}$ (with Ru loading varying from 0.5% to 2.0%) were characterized using XRD equipment, as shown in Fig. 3.2. The results indicate a monoclinic-type microstructure of $W_{18}O_{49}$ [23], consistent with previous studies. According to the Jade 6.0 analysis, the XRD spectra of all samples exhibit two intense diffraction peaks corresponding to the (0 1 0) and (0 2 0) crystal planes (JCPDS No. 05-0392). These planes are identified as the primary peaks in the spectra, while other peaks are much weaker and contribute to broad diffraction peaks. The (0 1 0) crystal plane is particularly noted as the strongest peak, indicating that the primary growth direction of the $W_{18}O_{49}$ crystals is [0 1 0] [14]. These observations are further confirmed by lattice fringe measurements obtained from subsequent HRTEM. The incorporation of Ru into $W_{18}O_{49}$ does not alter the monoclinic structure, as no new diffraction peaks appear. This suggests that Ru is homogeneously incorporated into the $W_{18}O_{49}$ matrix. The XRD spectra reveal a rightward shift in the diffraction peaks after Ru incorporation (Fig. 3.2b), which is indicative of lattice defects within the sample. Furthermore, the crystallite sizes (D) were calculated using the Debye-Scherrer equation (Eq. 3-1). The results, summarized in Tab. 3.2, show that the 1.0%Ru-loaded $W_{18}O_{49}$ has the smallest crystallite size compared to the other samples. As the Ru loading increases beyond 1.0%, the crystallite size also increases, indicating that an

optimal amount of Ru incorporation can effectively inhibit the growth of $W_{18}O_{49}$ nanocrystals during hydrothermal synthesis.

$$D = (0.89\times\lambda)/(\beta\times\cos\theta) \quad (3\text{-}1)$$

Where λ is the X-ray wavelength of the equipment in nm (0.15408 nm), β is the peak width at a half maximum in radian, and θ is the diffraction angle in radian.

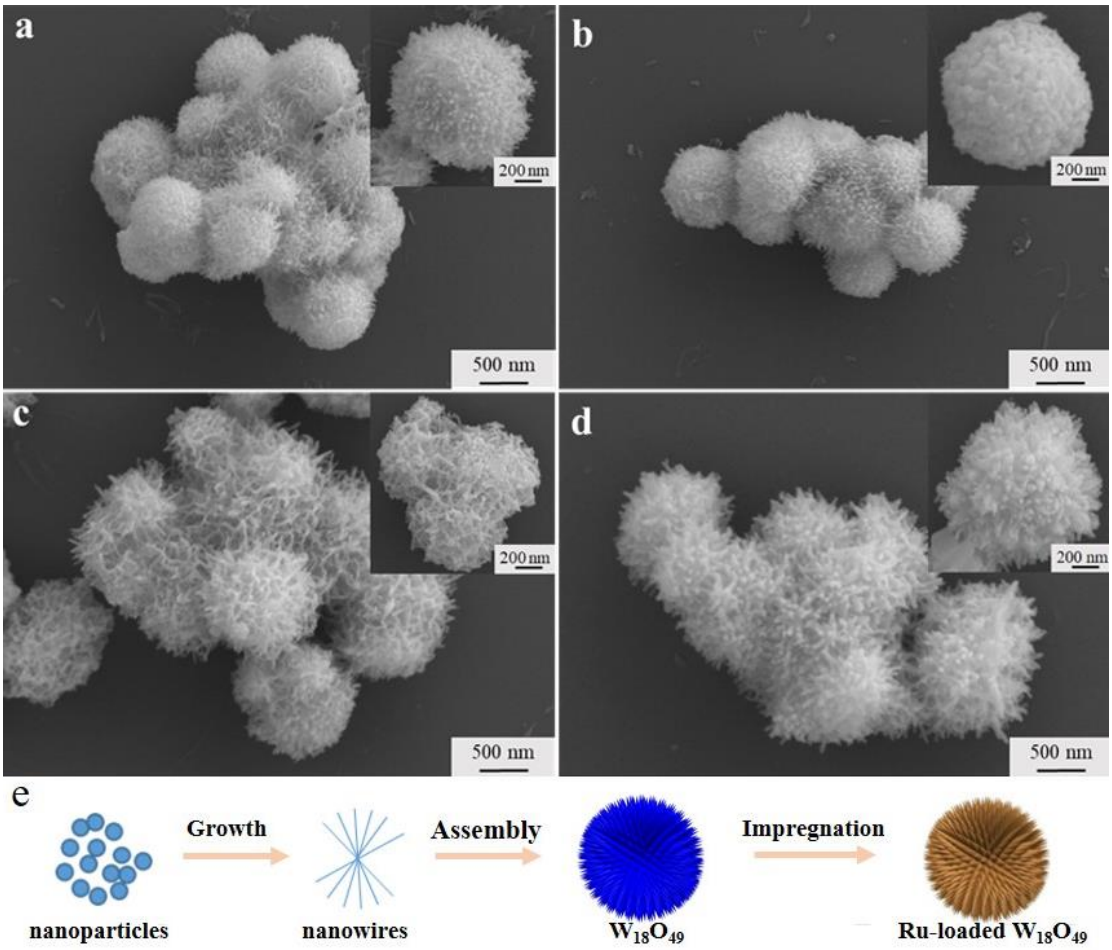

Fig. 3.3 FE-SEM images of (a) pure $W_{18}O_{49}$, (b) 0.5%Ru-loaded $W_{18}O_{49}$, (c) 1.0%Ru-loaded $W_{18}O_{49}$, (d) 2.0%Ru-loaded $W_{18}O_{49}$, (e) the formation mechanism of Ru-loaded urchin-like $W_{18}O_{49}$ hierarchical nanostructures.

Tab. 3.2 Crystallite size of pure and 0.5%-2.0%Ru-loaded $W_{18}O_{49}$ hierarchical nanostructures.

Sample	0.0%Ru	0.5%Ru	1.0%Ru	2.0%Ru
Size/nm	13.35	12.09	9.9	11.20

TEM was utilized to analyze the microstructure of the synthesized pristine and 1.0%Ru-loaded $W_{18}O_{49}$. The TEM morphologies of pure $W_{18}O_{49}$ and 1.0%Ru-loaded $W_{18}O_{49}$, shown in Figs. 3.4a and 3.4c respectively, are consistent with the morphologies observed by FE-SEM. The HRTEM images reveal a lattice fringe spacing of 0.378 nm for pure $W_{18}O_{49}$ (Fig. 3.4b), which corresponds to the (0 1 0) crystal plane. This confirms that the preferential growth direction of pure $W_{18}O_{49}$ is [0 1 0] [25], in agreement with the XRD analysis. For the 1.0%Ru-loaded $W_{18}O_{49}$, the lattice fringe spacing is observed to be 0.369 nm (Fig. 3.4d), which is smaller than that of pure $W_{18}O_{49}$. This reduction in lattice fringe spacing indicates the successful incorporation of Ru into the $W_{18}O_{49}$ structure, as evidenced by the shift in the diffraction peak seen in the XRD analysis (Fig. 3.2b). Besides, elemental analysis through EDX spectroscopy (Figs. 3.4f-3.4h) confirms the presence of W, O, and Ru in the 1.0% Ru-loaded $W_{18}O_{49}$ sample, and subsequent EDX mapping shows that all these elements are evenly distributed throughout the 1.0%Ru-loaded $W_{18}O_{49}$ hierarchical nanostructures, suggesting a uniform incorporation of Ru within the $W_{18}O_{49}$ matrix.

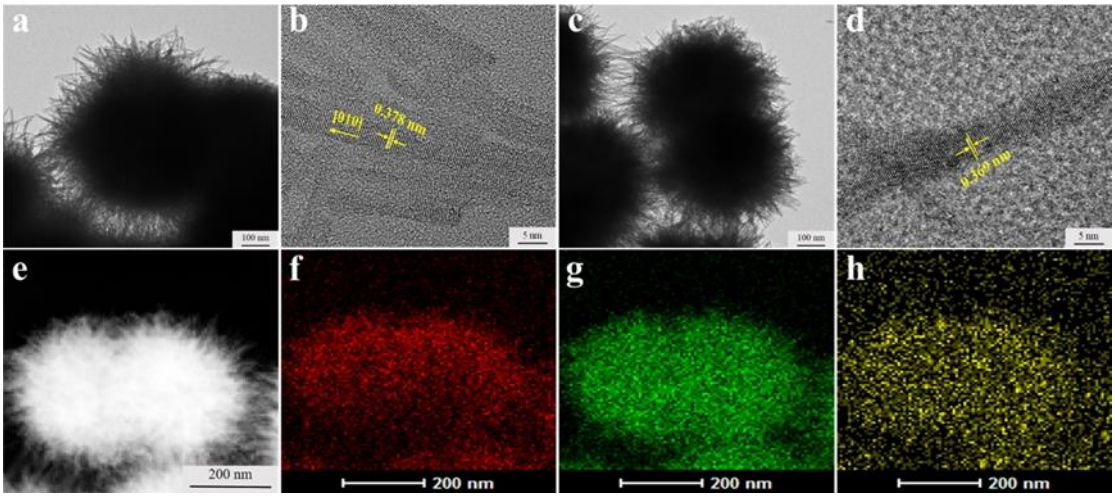

Fig. 3.4 TEM and HRTEM images of (a, b) pure $W_{18}O_{49}$, (c, d) 1.0%Ru-loaded $W_{18}O_{49}$, (e) high-angle annular dark-field scanning transmission electron microscope image of 1.0%Ru-loaded $W_{18}O_{49}$, (f-h) EDS mapping of W, O, and Ru elements.

The representative Raman spectra for the samples (Fig. 3.5a) indicate that the spectra are consistent with typical monoclinic $W_{18}O_{49}$, showing no shift with varying amounts of Ru loading. Characteristic peaks at 706 and 804 cm^{-1} are attributed to the W-O stretching mode. For the 0.5%-2.0%Ru-loaded $W_{18}O_{49}$, the Raman peaks shift towards lower wavenumbers compared to pure $W_{18}O_{49}$. This shift is associated with the reduced crystallite size of $W_{18}O_{49}$ after Ru incorporation. The N_2 adsorption and desorption isotherms of pure $W_{18}O_{49}$, 1.0% Ru-loaded $W_{18}O_{49}$ and 2.0%Ru-loaded $W_{18}O_{49}$ (Fig. 3.5b) correspond to type III isotherms. The specific surface area of

1.0%Ru-loaded $W_{18}O_{49}$ is significantly higher at 94.2 m^2/g, nearly double that of pure $W_{18}O_{49}$ (47.1 m^2/g). Pore size distribution curves indicate that the pore diameters for pure and 1.0%Ru-loaded $W_{18}O_{49}$ are 3.3 nm and 3.7 nm, respectively, both classified as mesoporous structures. Higher specific surface areas and mesoporous structures in gas-sensing materials enhance the number of active adsorption sites for the target gas. However, excessive Ru loading (e.g., 2.0%) reduces the specific surface area to 51.5 m^2/g. This reduction aligns with the XRD analysis suggesting that excessive Ru inhibits the crystallite growth of $W_{18}O_{49}$, leading to decreased specific surface areas. In addition, Fig. 3.5c reveals the UV-Vis-NIR absorption spectra for pure and 1.0%Ru-loaded $W_{18}O_{49}$. A significant absorption tail is identified in both near-infrared and visible regions, which indicates the presence of a substantial number of oxygen vacancies in the synthesized samples, achieved via a one-step hydrothermal route [26, 27]. Oxygen vacancies are crucial as they suggest that the $W_{18}O_{49}$-based gas sensing materials could lower the power consumption of gas sensors.

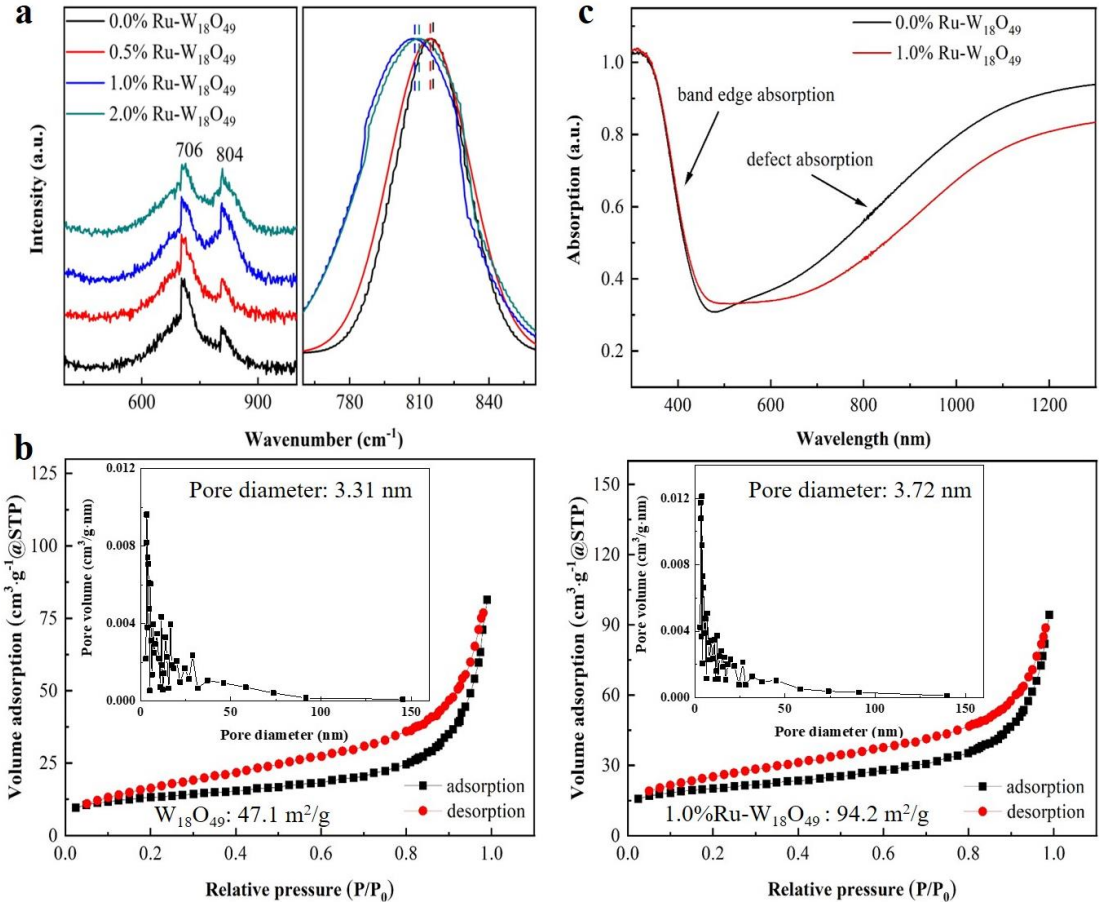

Fig. 3.5 (a) Raman spectra of pure and 0.5%-2.0%Ru-loaded $W_{18}O_{49}$ and a local enlargement of the peak at 804 cm^{-1}, (b) N_2 adsorption and desorption isotherms and corresponding pore size distribution curves of pure and 1.0%Ru-loaded $W_{18}O_{49}$, (c) UV-Vis-NIR spectra of pure and 1.0%Ru-loaded $W_{18}O_{49}$.

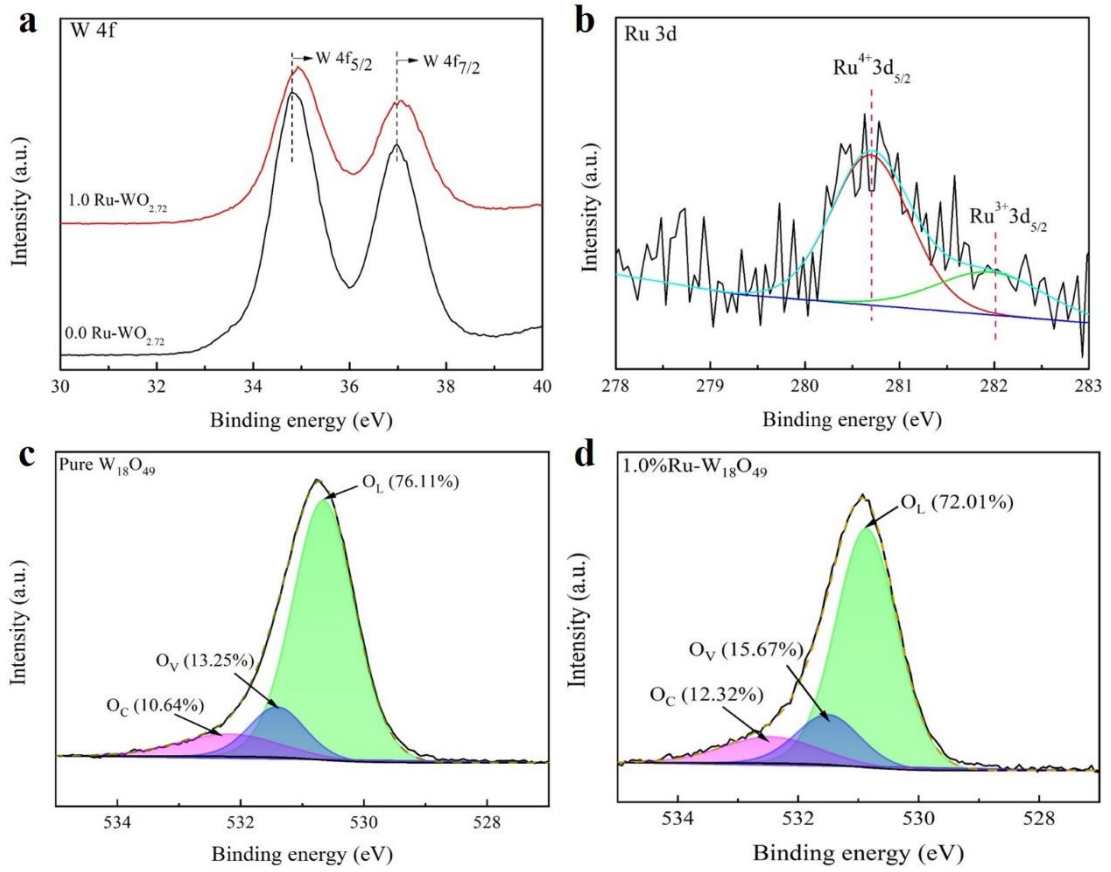

Fig. 3.6 XPS analysis of pure and 1.0%Ru-loaded $W_{18}O_{49}$, (a) W 4f spectra, (b) Ru 3d spectrum, (c, d) O 1s spectra.

The UV-Vis spectra confirm the presence of oxygen vacancies in $W_{18}O_{49}$-based gas-sensing materials. In order to further quantitatively analyze the changes in the concentrations of oxygen species before and after Ru incorporation, XPS was employed to analyze the chemical states of relevant elements in pure and 1.0%Ru-loaded $W_{18}O_{49}$. The XPS spectra of W 4f for pure and 1.0% Ru-loaded $W_{18}O_{49}$ are shown in Fig. 3.6a. Peaks at 35.5 and 37.6 eV correspond to W $4f_{5/2}$ and W $4f_{7/2}$, indicating a +6 oxidation state for tungsten [28, 29]. The W $4f_{5/2}$ peak in pure $W_{18}O_{49}$ is shifted 0.1 eV lower than in 1.0%Ru-loaded $W_{18}O_{49}$, suggesting electron loss in $W_{18}O_{49}$ due to Ru incorporation, confirming the formation of oxygen vacancies and successful Ru incorporation [30]. As illustrated in Fig. 3.6b, two kinds of Ru species are identified in the spectra of Ru 3d for 1.0%Ru-loaded $W_{18}O_{49}$, which can be attributed to Ru^{3+} and Ru^{4+}, respectively. Peaks at 280.7 and 281.9 eV correspond to Ru^{4+} $3d_{5/2}$ and Ru^{3+} $3d_{5/2}$, respectively [31-33]. The coexistence of Ru^{3+} and Ru^{4+} is beneficial for enhancing the catalytic activity of $W_{18}O_{49}$-based gas-sensing materials. Figs. 3.6c and 3.6d display the O 1s spectra for pure and 1.0%Ru-loaded $W_{18}O_{49}$, respectively. The spectra are fitted by the Gaussian function and are resolved into three peaks at 532.3, 531.5, and 530.6 eV, corresponding to chemisorbed oxygen (O_C), oxygen vacancy (O_V), and lattice oxygen (O_L),

respectively [34, 35]. By integrating each part, the concentrations of different oxygen species are calculated, as shown in the figures. In pure $W_{18}O_{49}$, the concentrations of O_C, O_V, and O_L are 10.64%, 13.25%, and 76.11%. For 1.0%Ru-loaded $W_{18}O_{49}$, the concentrations are 12.32%, 15.67%, and 72.01%, respectively. An increases in O_C and O_V components is observed after Ru incorporation. The gas-sensing mechanism of gas sensors based on metal oxides involves changes in carrier concentration due to the redox reaction between the target gas and O_C. The increased O_V component indicates more active adsorption sites available for redox reactions. Furthermore, the increased O_C component suggests that more oxygen species can participate in redox reactions. These changes in the chemical states are crucial for enhancing gas-sensing performance at room-temperature.

3.3.2 Gas-sensing performance investigation

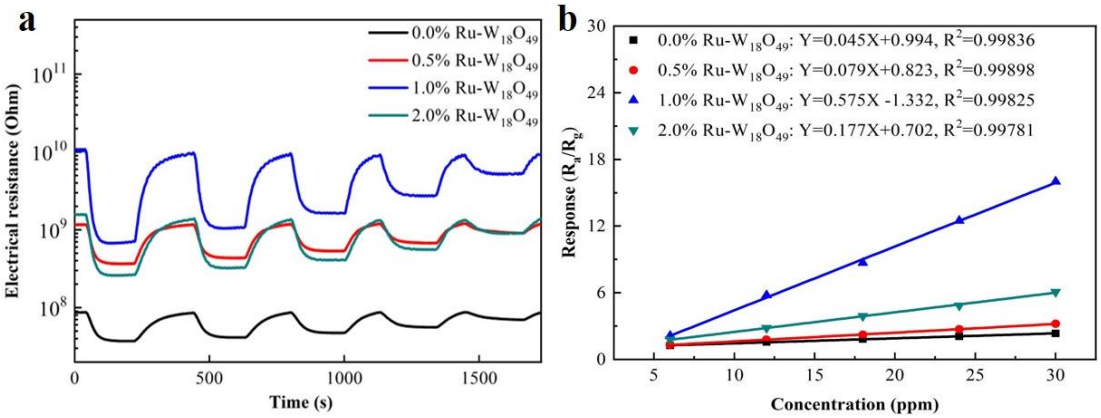

Fig. 3.7 (a) Changes in electrical resistance of all sensors towards different concentrations (6-30 ppm) of nonanal at room temperature, (b) linear relationship between sensor response and gas concentration.

To validate the gas-sensing performance of pure and Ru-loaded $W_{18}O_{49}$ sensors at low working temperatures, a series of laboratory tests were conducted. Fig. 3.7a illustrates the changes in electrical resistance of the sensors in response to different concentrations of nonanal at room temperature. The resistance of the sensors decreases upon exposure to nonanal and returns to the initial resistance (R_a) once purified air is introduced, indicating that the Ru-loaded $W_{18}O_{49}$ retains n-type characteristics. A notable observation is the significant increase in baseline resistance (R_a) with a low amount of Ru loading, which decreases again when Ru incorporation reaches 2.0%. For pure $W_{18}O_{49}$, the resistance (R_a) is measured at 87 MΩ, which for 1.0%Ru-loaded $W_{18}O_{49}$, it reaches 10.9 GΩ. This increase in resistance is attributed to the decrease in the crystallite size (Tab. 3.2) and carrier concentration due to the generation of depletion layers. XRD analysis indicates that Ru incorporation inhibits crystallite growth, which corresponds to the observed increase in resistance (R_a) for 1.0%Ru-loaded $W_{18}O_{49}$. This

phenomenon aligns with Kou et al.'s findings that resistance increases as crystallite size decreases [36]. Excessive Ru incorporation results in agglomeration and growth of Ru, reducing specific surface areas and diminishing the inhibition effect, leading to decreased resistance (R_a) [37, 38]. This is corroborated by XRD and BET analyses. Based on changes in the electrical resistance illustrated in Fig. 3.7a, the relationship between sensor response and gas concentration is demonstrated in Fig. 3.7b. The response presents a positive linear correlation with nonanal concentration. Besides, it is noteworthy that the response of 1.0%Ru-loaded $W_{18}O_{49}$ does not saturate even at a nonanal concentration of 30 ppm, suggesting that the fabricated gas sensor is capable of detecting nonanal molecules over a wide range. Specifically, the response of 1.0%Ru-loaded $W_{18}O_{49}$ to 30 ppm nonanal is 16.1, which is 6.8 times higher than that of pure $W_{18}O_{49}$. The enhanced performance is due to the increased active sites for nonanal absorption provided by the coexistence of Ru^{3+} and Ru^{4+}. Consequently, the incorporation of 1.0% Ru into $W_{18}O_{49}$ significantly improves room-temperature gas-sensing performance. The sensors demonstrate a wide detection range for nonanal, making them suitable for applications in rice quality assessment where nonanal is a key indicator.

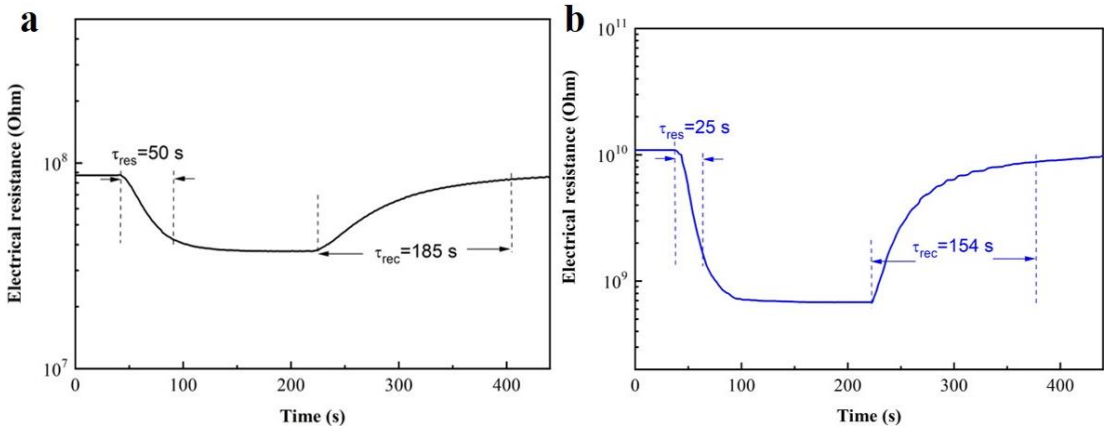

Fig. 3.8 Dynamic response-recovery curves of (a) pure and (b) 1.0%Ru-loaded $W_{18}O_{49}$ towards 30 ppm nonanal.

To provide a comprehensive evaluation of the gas-sensing performance of the developed sensors, dynamic response-recovery curves of pure and 1.0%Ru-loaded $W_{18}O_{49}$ were also analyzed. Figs. 3.8a and 3.8b show the dynamic response and recovery times of the sensors towards 30 ppm nonanal at room temperature. Compared to pure $W_{18}O_{49}$, the 1.0%Ru-loaded $W_{18}O_{49}$ sensor displays a significantly shorter response time of 25 s, suggesting superior response properties. Both sensors show recovery times exceeding 2 minutes. In fact, this slow recovery is a common limitation for MOS-based gas sensors operating at low temperatures, including room temperature. The slow recovery speed is attributed to the lower energy provide at room temperature,

which is insufficient to overcome the activation energy required for the desorption of nonanal molecules from the sensor surface [39]. This is a typical challenge for MOS-based gas sensors in low-temperature operations.

Given the crucial role of selectivity in practical applications [39], the selectivity of 1.0%Ru-loaded $W_{18}O_{49}$ was tested against various interfering gases (i.e., SO_2, H_2S, CO, NH_3, C_2H_5OH, C_3H_8O) at room temperature, as demonstrated in Fig. 3.9a. These results suggest that the 1.0%Ru-loaded $W_{18}O_{49}$ sensor exhibits excellent selectivity towards nonanal over the other interfering gases. The superior selectivity can be attributed to the lower bond energy of C-H-O in nonanal (312.8 kJ/mol), which makes it more susceptible to bond breaking during interactions with surface chemisorbed oxygen species [41, 42]. This facilitates the preferential adsorption and reaction of nonanal on the sensor surface, enhancing its selectivity.

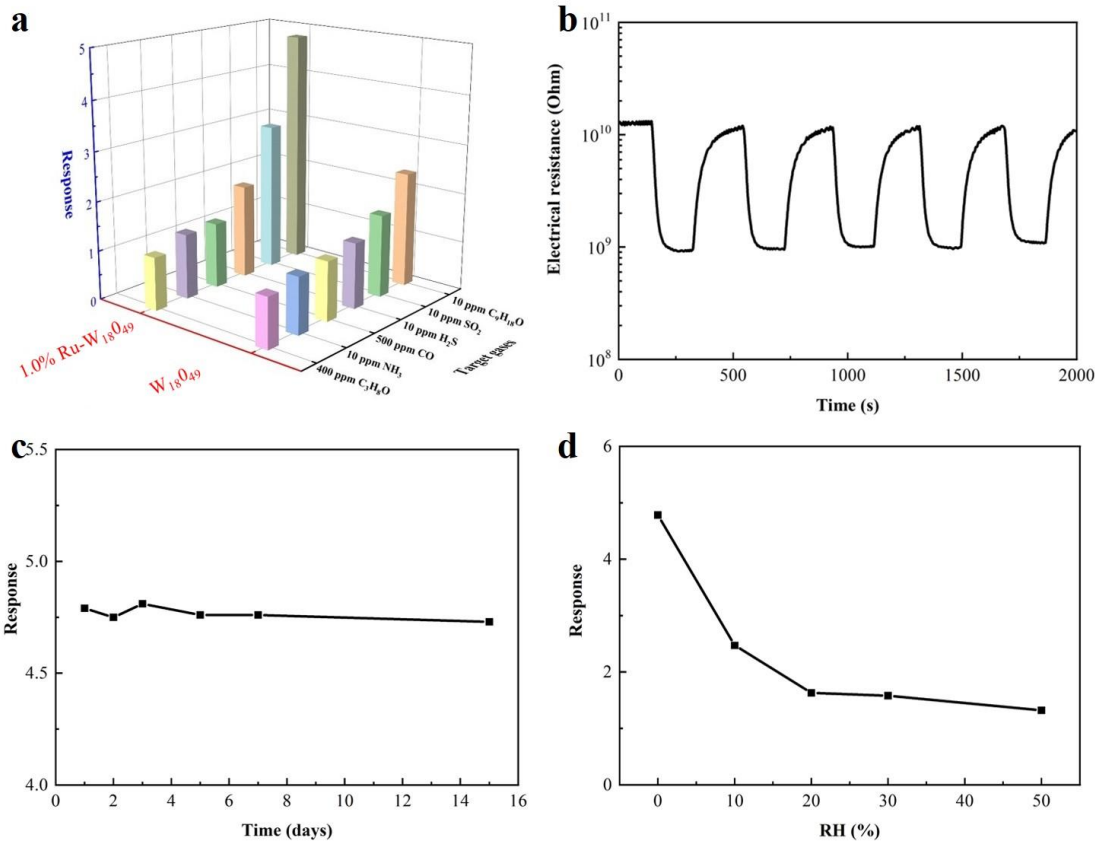

Fig. 3.9 (a) Response of 1.0%Ru-loaded $W_{18}O_{49}$ towards different interfering gases, (b) reproducibility of 1.0%Ru-loaded $W_{18}O_{49}$ towards 30 ppm nonanal, (c) stability of 1.0%Ru-loaded $W_{18}O_{49}$ towards 10 ppm nonanal, (d) response of 1.0%Ru-loaded $W_{18}O_{49}$ towards 10 ppm nonanal under different relative humidity conditions.

Fig. 3.9b presents the reversibility of the 1.0%Ru-loaded $W_{18}O_{49}$ sensor, which was tested by exposing the sensor to 30 ppm nonanal at room temperature over five cycles. The sensor maintains a consistent response over the five cycles, indicating

excellent reversibility. Furthermore, reproducibility and stability are also key indices for evaluating the service life and accuracy of the developed gas sensors in practical applications. The responses of the 1.0%Ru-loaded $W_{18}O_{49}$-based gas sensor towards 30 ppm nonanal were tested over an extended period, as displayed in Fig. 3.9c. There is no significant decrease in the sensor response over time, indicating excellent reproducibility and long-term stability. The stable existence of $W_{18}O_{49}$ in the environment likely contributes to the sensor's long-term stability and reproducibility, ensuring reliable performance in practical applications. Moreover, water vapor in the air adsorbs on the surface of gas-sensing materials, affecting the response of the gas sensors. Fig. 3.9d illustrates the effect of relative humidity on the response of 1.0%Ru-loaded $W_{18}O_{49}$ towards 10 ppm nonanal at room temperature. The sensor response decreases from 4.78 to 2.47 as relative humidity increases from 0% to 20%. Beyond 20%, the sensor response stabilizes. The initial decrease in response is attributed to the adsorption of water molecules on the sensor surface, which reduces the number of active sites available for nonanal adsorption. Besides, nonanal's practical insolubility in water further contributes to the decreased response at higher humidity levels. As relative humidity levels above 20%, the adsorption of water molecules reaches saturation, and the sensor response stabilize.

Tab. 3.3 Recently reported literature on nonanal sensors.

Material	Temperature	Concentration	Response	Ref.
Polyetherimide/Carbon black	RT	50 ppm	2.06	[41]
SnO_2 nanosheet	300 ℃	1 ppm	1.02	[9]
WO_3 nanowire	RT	3 ppm	1.03	[10]
Pt, Pd, Au/SnO_2 films	300 ℃	10 ppm	2.45	[43]
Ru-loaded $W_{18}O_{49}$	RT	10 ppm	4.79	This work

Tab. 3.3 summarizes the gas-sensing performance of 1.0%Ru-loaded $W_{18}O_{49}$-based gas sensor compared with recently reported literature on nonanal sensors. The results indicate that the 1.0%Ru-loaded $W_{18}O_{49}$-based gas sensor outperforms previously reported nonanal sensors, making it a competitive room-temperature gas sensor for nonanal analysis. Overall, the combination of non-stoichiometric WO_{3-x} synthesis and Ru incorporation, as proposed in this chapter, presents a promising strategy for developing high-performance room-temperature MOS-based gas sensors, particularly for the analysis of aldehydes.

3.3.3 Gas-sensing mechanism

The gas-sensing mechanism of the 1.0%Ru-loaded $W_{18}O_{49}$ that is well-accepted is an "adsorption-interaction-desorption" process [44, 45]. When the sensor is placed in the purified air, oxygen molecules adsorb on the surface of the gas-sensing materials to form surface chemisorbed oxygen species (i.e., O_2^-, O^-, and O^{2-}) according to their optimal working temperature. The proposed chemical reaction between the gas-sensing materials and the target gas can be outlined as follows [46]:

$$O_2\ (gas) \rightarrow O_2\ (ads) \tag{3-2}$$

$$O_2\ (ads) + e^- \rightarrow O_2^-\ (ads)\ (T < 150\ ℃) \tag{3-3}$$

$$O_2\ (ads) + 2e^- \rightarrow 2O^-\ (ads)\ (150\ ℃ < T < 400\ ℃) \tag{3-4}$$

$$O_2\ (ads) + 2e^- \rightarrow O^{2-}\ (ads)\ (T > 400\ ℃) \tag{3-5}$$

In this work, the gas-sensing performance investigations conducted at room temperature indicate that O_2^- is the dominant adsorption species of oxygen on the sensor surface. During this process, electrons become trapped by oxygen molecules. The movement of carriers generates a built-in field, resulting in the formation of an electrical potential difference between the surface and bulk of the gas-sensing materials. This phenomenon leads to an upward bending of the band structure. In the case of Ru-loaded $W_{18}O_{49}$, electrons flow from $W_{18}O_{49}$ to Ru, creating a wider electron-depletion region on the side of $W_{18}O_{49}$. The Schottky contact between Ru and $W_{18}O_{49}$ causes a higher barrier height, as schematically illustrated in Fig. 3.10. Consequently, the resistance (R_a) of the sensor increases [47].

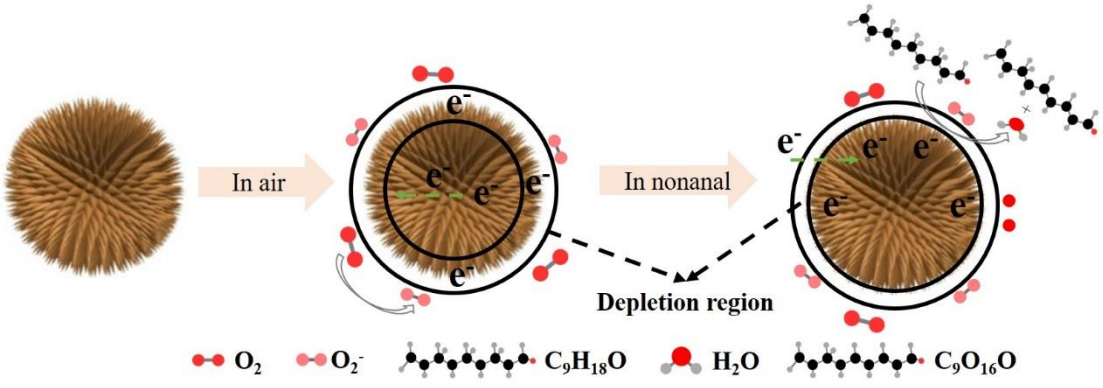

Fig. 3.10 Schematic illustrations of the room-temperature gas-sensing mechanism of Ru-loaded $W_{18}O_{49}$ in the analysis of nonanal.

When nonanal ($C_9H_{18}O$) interacts with the surface of the gas-sensing materials, it initially undergoes adsorption to form adsorbed states, as shown in Eq. 3-6.

Subsequently, the adsorbed nonanal reacts with the surface chemisorbed oxygen species (O_2^-) to produce new substances, including $C_9H_{16}O$ (ads) (resulting from the loss of H) and H_2O (gas), as depicted in Eq. 3-7 [48, 49]. This reaction releases electrons back into the conduction band, leading to a significant reduction in the thickness of the depletion region and the height of the potential barrier. As a result, the resistance (R_g) of the sensor decreases [50, 51].

$$C_9H_{18}O\ (gas) \rightarrow C_9H_{18}O\ (ads) \tag{3-6}$$

$$2C_9H_{18}O\ (ads) + O_2^- \rightarrow 2C_9H_{16}O + 2H_2O\ (gas) + e^- \tag{3-7}$$

The enhanced room-temperature gas-sensing performance of the 1.0%Ru-loaded $W_{18}O_{49}$-based gas sensor can be attributed to several key factors. Firstly, the unique urchin-like morphology has a large specific surface area (94.2 m^2/g) and excellent surface permeability, facilitating the adsorption of gas molecules. Secondly, the presence of oxygen vacancies within the material significantly enhances gas-sensing reactions. The concentrations of oxygen vacancies and chemisorbed oxygen species are higher in 1.0%Ru-loaded $W_{18}O_{49}$, as evidenced by the O 1s spectra analysis (Figs. 3.6c and 3.6d). Oxygen vacancies act as electron donors, creating additional gas-absorbing sites and free electrons, thereby enhancing the gas-sensing process. Moreover, many works have reported that the gas-sensing performance of MOS-based gas sensors is influenced by their bandgaps [52]. From the UV-Vis-NIR spectra shown in Fig. 3.5c, the 1.0%Ru-loaded $W_{18}O_{49}$ has a narrower energy band. It is acknowledged that MOS with narrower bad gaps is helpful to generate more excited charge carriers, and more adsorbed oxygen species can be accumulated on the surface of the gas-sensing materials. Thirdly, loading an appropriate amount of Ru effectively inhibits the growth of $W_{18}O_{49}$ nanocrystals during hydrothermal synthesis and enhances catalytic effects. This results in increased specific surface areas and concentrations of oxygen vacancies and chemisorbed oxygen species, further improving the gas-sensing properties of the sensor. Overall, these factors collectively contribute to the enhanced room-temperature gas-sensing performance of the 1.0%Ru-loaded $W_{18}O_{49}$-based gas sensor in the analysis of nonanal.

3.3.4 Practical application of 1.0%Ru-loaded $W_{18}O_{49}$-based gas sensor

To verify the practicability of the in evaluating rice quality, the changes in resistance of the sensor towards VOCs generated from the two types of rice are monitored. To carry out the above experiment, 30 g of japonica rice and indica rice bought from a supermarket were sealed in a 50 mL glass bottle. The flow was adjusted by a mass flow controller. As demonstrated in Fig. 3.11a, the response of the fabricated gas sensor towards the VOCs generated from indica rice aging is much higher than that

of japonica rice stored at 25 ℃, suggesting that the sensor may be capable of distinguishing indica rice from japonica rice. In addition, the variation of electrical resistance is recorded at room temperature with the concentration changes of the produced VOCs during the storage of indica rice at different temperatures (i.e., 25, 50, and 75 ℃). As illustrated in Fig. 3.11b, the sensor response significantly increases with higher storage temperatures under the same testing conditions, demonstrating an elevated concentration of VOCs derived from the rice aging. An increase in the sensor response is chiefly attributed to the higher storage temperature, significantly accelerating the oxidation rate of the lipids [21]. Given this situation, the aging process of rice accelerates to increase the concentration of aldehydes. These practical experiments reveal that the fabricated gas sensor based on 1.0%Ru-loaded $W_{18}O_{49}$ may be utilized to be the detection unit of high-performance E-nose for room-temperature detection of aldehydes.

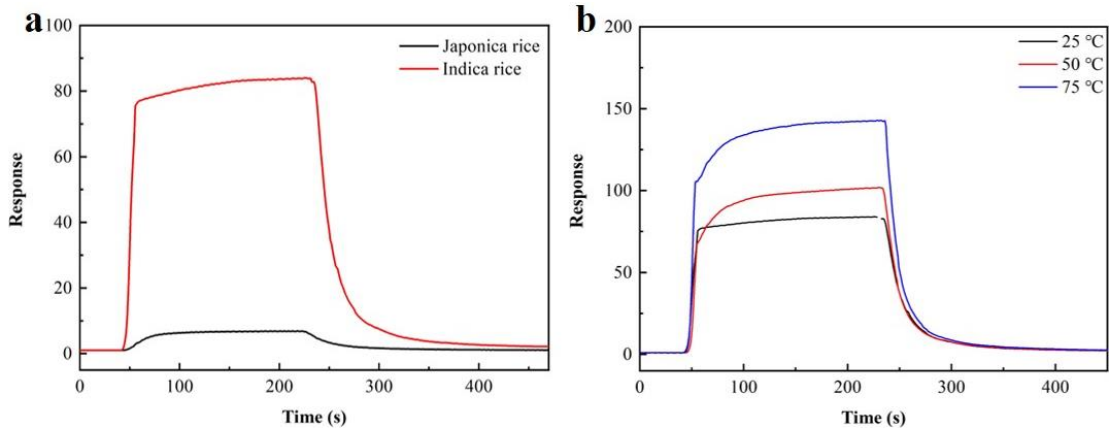

Fig. 3.11 (a) Response measured at 25 ℃ under exposure to VOCs from the two types of rice, (b) response towards different concentrations of VOCs generated from 30 g indica rice stored at different temperatures (25, 50, and 75 ℃).

3.4 Conclusions

In this chapter, pure and 0.5%-2.0%Ru-loaded urchin-like $W_{18}O_{49}$ hierarchical nanostructures are synthesized by a one-step hydrothermal combined with the subsequent calcination under an inert atmosphere (N_2). By controlling the amount of Ru loading, the crystallite size and the oxygen vacancy concentration of $W_{18}O_{49}$-based gas-sensing materials are regulated, and they are used for room-temperature detection of aldehydes, being a characteristic biomarker generated from rice aging. The structural characterizations and gas-sensing performance investigations are conducted to comprehensively investigate the influence of Ru incorporation on the enhanced gas-sensing mechanisms of the $W_{18}O_{49}$-based gas sensor. The main conclusions drawn in this chapter are summarized as follows:

(1) Microstructural analyses of both pure and Ru-loaded $W_{18}O_{49}$ reveal negligible alterations in the morphology before and after the loading of Ru with both variants maintaining the urchin-like structure. The XRD analysis indicates that a moderate amount of Ru loading effectively suppresses the growth of $W_{18}O_{49}$-based nanocrystals during the hydrothermal synthesis.

(2) Analysis of the Ru 3d spectrum illustrates that Ru exists in two valence states rather than as a simple substance, indicating the co-existence of Ru (III) and Ru (IV), thereby enhancing the catalytic activity. According to the peak fitting results of the O 1s spectra, the relative percentages of chemisorbed oxygen species and oxygen vacancies slightly increase after the loading of Ru, collectively enhancing the subsequent room-temperature gas-sensing performance.

(3) Room-temperature gas-sensing performance of Ru-loaded $W_{18}O_{49}$ towards nonanal, one of the medium-chain aldehydes derived from the oxidation and hydrolysis of the lipids in rice aging, demonstrates that the baseline resistance (R_a) increases two orders of magnitude, the sensor response elevates by 6.8 times, and the response time decreases by 50% in comparison with pure $W_{18}O_{49}$. Moreover, a comparison with recent literature on nonanal sensors illustrates that 1.0%Ru-loaded $W_{18}O_{49}$ can indeed achieve the detection of nonanal at room temperature.

(4) The enhanced gas-sensing performance of Ru-loaded $W_{18}O_{49}$ can be due to its unique urchin-like morphology, the elevated relative proportions of chemisorbed oxygen species and oxygen vacancies, and the co-existence of Ru^{3+} and Ru^{4+}. In detail, the urchin-like morphology provides large specific surface areas, which is beneficial to adsorb nonanal molecules. Non-stoichiometric $W_{18}O_{49}$ has highly concentrated oxygen vacancies, enhancing the adsorption of oxygen, thus increasing the oxygen species that react with nonanal. Incorporating a proper amount of Ru into $W_{18}O_{49}$ can effectively inhibit crystallite growth together with the catalytic oxidation of both Ru (III) and Ru (IV), which causes an increase in the specific surface area, relative proportions of chemisorbed oxygen and oxygen vacancy components.

(5) The practical experiments demonstrate that the response of 1.0%Ru-loaded $W_{18}O_{49}$ towards VOCs in indica rice aging is 83.9, representing a 12.3-fold increase compared to japonica rice, suggesting that it may be capable of distinguishing indica rice from japonica rice. In addition, as the storage temperature rises, the sensor response significantly increases. Collectively, these results underscore the potential of the developed gas sensor as a component of an E-nose system for room-temperature detection of aldehydes.

References

[1] X.Q. Hu, L. Lu, Z.L. Guo, Z.W. Zhu. Volatile compounds, affecting factors and evaluation methods for rice aroma: A review. Trends in Food Science & Technology, 97 (2020) 136-146. https://doi.org/10.1016/j.tifs.2020.01.003.

[2] K.W. Liu, C. Zhang. Volatile organic compounds gas sensor based on quartz crystal microbalance for fruit freshness detection: A review. Food Chemistry, 334 (2021) 127615. https://doi.org/10.1016/j.foodchem.2020.127615.

[3] C.C. Li, W. Li, X.H. Chen, M.Q. Feng, X. Rui, M. Jiang, M.S. Dong. Microbiological, physicochemical and rheological properties of fermented soymilk produced with exopolysaccharide (EPS) producing lactic acid bacteria strains. LWT-Food Science and Technology, 57 (2014) 477-485. https://doi.org/10.1016/j.lwt.2014.02.025.

[4] Q.Y. Zhao, Y. Xue, Q. Shen. Changes in the major aroma-active compounds and taste components of Jasmine rice during storage. Food Research International, 133 (2020) 109160. https://doi.org/10.1016/j.foodres.2020.109160.

[5] S.M. Lee, H.J. Lim, J.W. Chang, B.S. Hurh, Y.S. Kim. Investigation on the formations of volatile compounds, fatty acids, and γ-lactones in white and brown rice during fermentation. Food Chemistry, 269 (2018) 347-354. https://doi.org/10.1016/j.foodchem.2018.07.037.

[6] H. Shin, W.G. Jung, D.H. Kim, J.S. Jang, Y.H. Kim, W.T. Koo, J. Bae, C. Park, S.H. Cho, B.J. Kim, I.D. Kim. Single-atom Pt stabilized on one-dimensional nanostructure support via carbon nitride/SnO_2 heterojunction trapping. ACS Nano, 14 (2020) 11394-11405. https://doi.org/10.1021/acsnano.0c03687.

[7] M. Poloju, N. Jayababu, E. Manikandan, M. Reddy. Enhancement of the isopropanol gas sensing performance of SnO_2/ZnO core/shell nanocomposites. Journal of Materials Chemistry C, 5 (2017) 2662-2668. https://doi.org/10.1039/C6TC05095F.

[8] Y. Li, Y.L. Lu, K.D. Wu, D.Z. Zhang, M. Debliquy, C. Zhang. Microwave-assisted hydrothermal synthesis of copper oxide-based gas-sensitive nanostructures. Rare Metals, 40 (2021) 1477-1493. https://doi.org/10.1007/s12598-020-01557-4.

[9] P.G. Choi, N. Shirahata, Y. Masuda. Tin oxide nanosheet thin film with bridge type structure for gas sensing. Thin Solid Films, 698 (2020) 137845. https://doi.org/10.1016/j.tsf.2020.137845.

[10] G.Z. Zhang, C. Wang, W. Mizukami, T. Hosomi, K. Nagashima, H. Yoshida, K. Nakamura, T. Takahashi, M. Kanai, T. Yasui, Y. Aoki, Y. Baba, T. Yanagida. Monovalent sulfur oxoanions enable millimeter-long single-crystalline h-WO_3 nanowire synthesis. Nanoscale, 12 (2020) 9058-9066.

https://doi.org/10.1039/C9NR10565D.

[11] A. Staerz, S. Somacescu, M. Epifani, T. Kida, U. Weimar, N. Barsan. WO_3-based gas sensors: Identifying inherent qualities and understanding the sensing mechanism. ACS Sensors, 5 (2020) 1624-1633. https://doi.org/10.1021/acssensors.0c00113.

[12] F. Peng, W.W. Yu, Y. Lu, Y. Sun, X.L. Fu, J.M. Hao, X. Chen, R. Cong, N. Dai. Enhancement of low-temperature gas-sensing performance using substoichiometric WO_{3-x} modified with CuO. ACS Applied Materials & Interfaces, 337 (2020) 41230-41238. https://doi.org/10.1021/acsami.0c09213.

[13] C. Shu, S. Kang, Y.S. Jin, X. Yue, P.K. Shen. Bifunctional porous non-precious metal WO_2 hexahedral networks as an electrocatalyst for full water splitting. Journal of Materials Chemistry A, 5 (2017) 9655-9660. https://doi.org/10.1039/C7TA01527E.

[14] Y.S. Xu, T.T. Ma, L.L. Zheng, L. Sun, X.H. Liu, Y.Q. Zhao, J. Zhang. Rational design of Au/Co_3O_4-functionalized $W_{18}O_{49}$ hollow heterostructures with high sensitivity and ultralow limit for triethylamine detection. Sensors and Actuators B: Chemical, 284 (2019) 202-212. https://doi.org/10.1016/j.snb.2018.12.119.

[15] Y. Xiong, Z.Y. Zhu, T.C. Guo, H. Li, Q.Z. Xue. Synthesis of nanowire bundle-like WO_3-$W_{18}O_{49}$ heterostructures for highly sensitive NH_3 sensor application. Journal of Hazardous Materials, 353 (2018) 290-299. https://doi.org/10.1016/j.jhazmat.2018.04.020.

[16] S.B. Sun, M.W. Wang, X.T. Chang, Y.C. Jiang, D.Z. Zhang, D.S. Wang, Y.L. Zhang, Y.H. Lei. $W_{18}O_{49}$/$Ti_3C_2T_x$ Mxene nanocomposites for highly sensitive acetone gas sensor with low detection limit. Sensors and Actuators B: Chemical, 304 (2020) 127274. https://doi.org/10.1016/j.snb.2019.127274.

[17] P. Wang, S.S. Guo, Z.X. Hu, L.C. Zhou, T.K. Li, S.L. Pu, H. Mao, H. Cai, Z.F. Zhu, B.B. Chen, H.Y. Li, H. Liu. Single-atom Cu stabilized on ultrathin $WO_{2.72}$ nanowire for highly selective and ultrasensitive ppb-level toluene detection. Advanced Science, 10 (2023) 2302778. https://doi.org/10.1002/advs.202302778.

[18] H. Li, S. Chu, Q. Ma, H. Li, Q.D. Che, J.P. Wang, G. Wang, P. Yang. Multilevel effective heterojunctions based on SnO_2/ZnO 1D fibrous hierarchical structure with unique interface electronic effects. ACS Applied Materials & Interfaces, 11 (2019) 31551-31561. https://doi.org/10.1021/acsami.9b10410.

[19] J.S. Jang, H. Yu, S.J. Choi, W.T. Koo, J. Lee, D.H. Kim, J.Y. Kang, Y.J. Jeong, H. Jeong, I.D. Kim. Heterogeneous metal oxide-graphene thorn-bush single fiber as a freestanding chemiresistor. ACS Applied Materials & Interfaces, 11 (2019) 10208-10217. https://doi.org/10.1021/acsami.8b22015.

[20] D.L. Feng, Z.Y. Zhu, L.L. Du, X.X. Xing, C. Wang, J. Chen, Y.T. Tian, D.C. Yang. Improved sensing performance of WO_3 nanoparticles decorated with Ag and Pt

nanoparticles. Rare Metals, 40 (2021) 1642-1650. https://doi.org/10.1007/s12598-020-01666-0.

[21] J.Y. Xu, K.W. Liu, C. Zhang. Electronic nose for volatile organic compounds analysis in rice aging. Trends in Food Science & Technology, 109 (2021) 83-93. https://doi.org/10.1016/j.tifs.2021.01.027.

[22] https://www.chemicalbook.com/ProductChemicalPropertiesCB2667328_EN.htm.

[23] K. Thummavichai, N.N. Wang, L.C. Lem, M. Phillips, C. Ton-That, H. Chang, C.X. Hu, F. Xu, Y.D. Xia, Y.Q. Zhu. Lanthanide-doped $W_{18}O_{49}$ nanowires: synthesis, structure and optical properties. Materials Letters, 214 (2018) 232-235. https://doi.org/10.1016/j.matlet.2017.12.022.

[24] Y.Y. Zhao, Q.W. Tang, P.Z. Yang, B.L. He. Robust electrocatalysts from metal doped $W_{18}O_{49}$ nanofibers for hydrogen evolution. Chemical Communications, 53 (2017) 4323-4326. https://doi.org/10.1039/C7CC01249G.

[25] G.C. Xi, J.H. Ye, Q. Ma, N. Su, H. Bai, C. Wang. In situ growth of metal particles on 3D urchin-like WO_3 nanostructures. Journal of the American Chemical Society, 134 (2012) 6508-6511. https://doi.org/10.1021/ja211638e.

[26] H.Y. Chen, L.Z. Song, S.X. Ouyang, J.B. Wang, J. Lv, J.H. Ye. Co and Fe codoped $WO_{2.72}$ as alkaline-solution-available oxygen evolution reaction catalyst to construct photovoltaic water splitting system with solar-to-hydrogen efficiency of 16.9%. Advanced Science, 6 (2019) 1900465. https://doi.org/10.1002/advs.201900465.

[27] Y.S. Xu, L.L. Zheng, C. Yang, W. Zheng, X.H. Liu, J. Zhang. Oxygen vacancies enabled porous SnO_2 thin films for highly sensitive detection of triethylamine at room temperature. ACS Applied Materials & Interfaces, 12 (2020) 20704-20713. https://doi.org/10.1021/acsami.0c04398.

[28] Y.S. Xu, T.T. Ma, L.L. Zheng, Y.Q. Zhao, X.H. Liu, J. Zhang. Heterostructures of hematite-sensitized $W_{18}O_{49}$ hollow spheres for improved acetone detection with ultralow detection limit. Sensors and Actuators B: Chemical, 288 (2019) 432-441. https://doi.org/10.1016/j.snb.2019.03.015.

[29] T. Soltani, A. Tayyebi, B.K. Lee. Sonochemical-driven ultrafast facile synthesis of WO_3 nanoplates with controllable morphology and oxygen vacancies for efficient photoelectrochemical water splitting. Ultrasonics Sonochemistry, 50 (2019) 230-238. https://doi.org/10.1016/j.ultsonch.2018.09.023.

[30] B.Y. Kim, J.W. Yoon, J.K. Kim, Y.C. Kang, J.H. Lee. Dual role of multiroom-structured Sn-doped NiO microspheres for ultrasensitive and highly selective detection of xylene. ACS Applied Materials & Interfaces, 10 (2018) 16605-16612. https://doi.org/10.1021/acsami.8b02412.

[31] J. Wang, J. Su, H. Chen, X.X. Zou, G.D. Li. Oxygen vacancy-rich, Ru-doped In_2O_3 ultrathin nanosheets for efficient detection of xylene at low temperature. Journal of

Materials Chemistry C, 6 (2018) 4156-4162. https://doi.org/10.1039/C8TC00638E.

[32] J. Balcerzak, W. Redzynia, J. Tyczkowski. In-situ XPS analysis of oxidized and reduced plasma deposited ruthenium-based thin catalytic films. Applied Surface Science, 426 (2017) 852-855. https://doi.org/10.1016/j.apsusc.2017.07.248.

[33] E.A. Paoli, F. Masini, R. Frydendal, D. Deiana, C. Schlaup, M. Malizia, T.W. Hansen, S. Horch, I.E.L. Stephens, I. Chorkendorff. Oxygen evolution on well-characterized mass-selected Ru and RuO_2 nanoparticles. Chemical Science, 6 (2015) 190-196. https://doi.org/10.1039/C4SC02685C.

[34] J. Jung, D.H. Kim. $W_{18}O_{49}$ nanowires assembled on carbon felt for application to supercapacitors. Applied Surface Science, 433 (2018) 750-755. https://doi.org/10.1016/j.apsusc.2017.10.109.

[35] D. Liu, X.W. Ren, Y.S. Li, Z.L. Tang, Z.T. Zhang. Nanowires-assembled WO_3 nanomesh for fast detection of ppb-level NO_2 at low temperature. Journal of Advanced Ceramics, 9 (2020) 17-26. https://doi.org/10.1007/s40145-019-0343-3.

[36] X.Y. Kou, F.Q. Meng, K. Chen, T.S. Wang, P. Sun, F.M. Liu, X. Yan, Y.F. Sun, F.M. Liu, K. Shimanoe, G.Y. Lu. High-performance acetone gas sensor based on Ru-doped SnO_2 nanofibers. Sensors and Actuators B: Chemical, 320 (2020) 128292. https://doi.org/10.1016/j.snb.2020.128292.

[37] S.S. Mehta, D.Y. Nadargi, M.S. Tamboli, L.A. Chaudhary, P.S. Patil, I.S. Mulla, S.S. Suryavanshi. Ru-loaded mesoporous WO_3 microflowers for dual applications: enhanced H_2S sensing and sunlight-driven photocatalysis. Dalton Transactions, 47 (2018) 16840-16845. https://doi.org/10.1039/C8DT03667E.

[38] Y.C. Huan, K.D. Wu, C.J. Li, H.L. Liao, M. Debliquy, C. Zhang. Micro-nano structured functional coatings deposited by liquid plasma spraying. Journal of Advanced Ceramics, 9 (2020) 517-534. https://doi.org/10.1007/s40145-020-0402-9.

[39] J.Y. Xu, H.L. Liao, C. Zhang. $ZnSnO_3$ based gas sensors for pyridine volatile marker detection in rice aging during storage. Food Chemistry, 408 (2023) 135204. https://doi.org/10.1016/j.foodchem.2022.135204.

[40] Y.J. Su, J.J. Wang, B. Wang, T.N. Yang, B.X. Yang, G.Z. Xie, Y.H. Zhou, S.L. Zhang, H.L. Tai, Z.X. Cai, G.R. Chen, Y.D. Jiang, L.Q. Chen, J. Chen. Alveolus-inspired active membrane sensors for self-powered wearable chemical sensing and breath analysis. ACS Nano, 14 (2020) 6067-6075. https://doi.org/10.1021/acsnano.0c01804.

[41] A. Daneshkhah, S. Vij, A.P. Siegel, M. Agarwal. Polyetherimide /carbon black composite sensors demonstrate selective detection of medium-chain aldehydes including nonanal. Chemical Engineering Journal, 383 (2020) 123104. https://doi.org/10.1016/j.cej.2019.123104.

[42] J.A. Herron, P. Ferrin, M. Mavrikakis. First-principles mechanistic analysis of

dimethyl ether electro-oxidation on monometallic single-crystal surfaces. Journal of Physical Chemistry C, 118 (2014) 24199-24211. https://doi.org/10.1021/jp505919x.

[43] T. Itoh, T. Nakashima, T. Akamatsu, N. Izu, W. Shin. Nonanal gas sensing properties of platinum, palladium, and gold-loaded tin oxide VOCs sensors. Sensors and Actuators B: Chemical, 187 (2013) 135-141. https://doi.org/10.1016/j.snb.2012.09.097.

[44] A.M. Al-Enizi, M. Naushad, A.H. Al-Muhtaseb, A.H. Ruksana, S.M. Alshehri, Z.A. Alothman, T. Ahamad. Synthesis and characterization of highly selective and sensitive Sn/SnO_2/N-doped carbon nanocomposite (Sn/SnO_2@NGC) for sensing toxic NH_3 gas. Chemical Engineering Journal, 345 (2018) 58-66. https://doi.org/10.1016/j.cej.2018.03.138.

[45] H. Li, S.S. Chu, Q. Ma, Y. Fang, J.P. Wang, Q.D. Che, G. Wang, P. Yang. Novel construction of morphology-tunable C-N/SnO_2/ZnO/Au microspheres with ultrasensitivity and high selectivity for triethylamine under various temperature detections. ACS Applied Materials & Interfaces, 11 (2019) 8601-8611. https://doi.org/10.1021/acsami.8b22357.

[46] S. Cao, T.T. Zhou, X.Y. Xu, Y. Bing, N. Sui, J. Wang, J. Li, T. Zhang. Metal-organic frameworks derived inverse/normal bimetallic spinel oxides toward the selective VOCs and H_2S sensing. Journal of Hazardous Materials, 457 (2023) 131734. https://doi.org/10.1016/j.jhazmat.2023.131734.

[47] F.D. Zhang, X. Dong, X.L. Cheng, Y.M. Xu, X.F. Zhang, L.H. Huo. Enhanced gas-sensing properties for trimethylamine at low temperature based on MoO_3/$Bi_2Mo_3O_{12}$ hollow microspheres. ACS Applied Materials & Interfaces, 11 (2019) 11755-11762. https://doi.org/10.1021/acsami.8b22132.

[48] D. Meena, B. Singh, A. Anand, M. Singh, M.C. Bhatnagar. Phase dependent selectivity shifting behavior of Cd_2SnO_4 nanoparticles based gas sensor towards volatile organic compounds (VOC) at low operating temperature. Journal of Alloys and Compounds, 820 (2020) 153117. https://doi.org/10.1016/j.jallcom.2019.153117.

[49] H.J. Gao, Y.Z. Ma, P. Song, Z.X. Yang, Q. Wang. Three-dimensional reduced graphene oxide/cobaltosic oxide as a high-response sensor for triethylamine gas at room temperature. Materials Science in Semiconductor Processing, 133 (2021) 105904. https://doi.org/10.1016/j.mssp.2021.105904.

[50] M.S. Yao, W.H. Li, G. Xu. Metal-organic frameworks and their derivatives for electrically-transduced gas sensors. Coordination Chemistry Reviews, 426 (2021) 213479. https://doi.org/10.1016/j.ccr.2020.213479.

[51] J. Wang, F.M. Chen, Q. Guo, Y. Meng, M.R. Jiang, C.S. Wu, J. Zhuang, D.W. Zhang. Light-addressable square wave voltammetry (LASWV) based on a field-

effect structure for electrochemical sensing and imaging. ACS Sensors, 6 (2021) 1636-1642. https://doi.org/10.1021/acssensors.1c00170.

[52] N. Sui, S. Cao, P. Zhang, T.T. Zhou, T. Zhang. The effect of different crystalline phases of In_2O_3 on the ozone sensing performance. Journal of Hazardous Materials, 418 (2021) 126290. https://doi.org/10.1016/j.jhazmat.2021.126290.

Chapter 4 Oxygen engineering on cerium oxide nanowires by post-treatment for linalool detection

4.1 Introduction

Linalool, an alcohol produced from the further breakdown of aldehydes, significantly contributes to the aroma profile of rice during aging [1-5]. Changes in its content can serve as an indicator for inspecting rice quality. Therefore, monitoring and identifying linalool concentration is an effective method for evaluating rice quality. Due to the limitations of traditional assessment methods, such as liquid chromatography-mass spectrometry, near-infrared spectroscopy, and GC-MS, it is essential to develop a non-destructive and real-time measurement technique for linalool monitoring with excellent gas-sensing properties.

Commercially available gas sensors based on metal oxides, such as tin oxide [6] and zinc oxide [7], have been widely used for the quantitative assessment of volatile compounds, including linalool. Among these materials, cerium oxide (CeO_2) stands out as a promising gas-sensing material due to its abundant crystal defects, high electrical conductivity, and good chemical stability [8, 9]. Previous studies have demonstrated the utilization of CeO_2-based gas sensors for detecting VOCs, showcasing their rapid response and recovery times. For example, Lyu et al. constructed a hollow-structured CeO_2 for detecting VOCs [10]. This sensor exhibited a rapid response/recovery time (6/11 s) towards 100 ppm acetone at an optimal working temperature of 260 ℃. However, operating at such a high temperature, which exceeds the boiling point of some VOCs, may lead to the pyrolysis of the target gas. This drawback limits its application in rice quality inspection. Therefore, to effectively identify variations in linalool concentration during rice aging, the operation of a CeO_2-based gas sensor should be performed at low working temperatures [11].

At low working temperatures, CeO_2-based gas sensors often suffer from limitations such as a low response and high detection limits. To significantly improve the gas-sensing properties of CeO_2 at low working temperatures, particularly at room temperature, several optimization strategies have been adopted. For example, Liu et al. synthesized hollow CeO_2 tubules with mesoporous structures for VOC detection [12]. Their investigations revealed that the sensor response towards 100 ppm p-xylene VOC was 12.4 at a relatively low working temperature of 133 ℃. Notably, the limit of detection of the optimal gas sensor was reduced to 100 ppb, the lowest value among the reported gas sensors based on CeO_2. Motaung et al. constructed a heterojunction between CeO_2 and SnO_2 through a hydrothermal method [13]. The gas sensor based on

CeO_2-SnO_2 nanocomposites exhibited an impressive response (~39.8) towards 20 ppm of the target gas at room temperature. Unfortunately, CeO_2, being an ionic conductor, has inadequate adsorption sites, low conductivity, and high electrical resistance (1-10 GΩ) at room temperature, dramatically affecting the concentration of linalool that can be measured by the gas sensor. Additionally, most MOS-based gas sensors have a low response towards linalool macromolecules due to the chemical inertness of linalool, especially at room temperature.

Regulating the electronic structures and surface chemical states of MOS is a feasible solution for developing high-performance room-temperature MOS-based gas sensors. Oxygen vacancy engineering has emerged as a promising pathway to optimize the crystal structure and surface activity of metal oxides, significantly improving their room-temperature gas-sensing performance at room temperature [14, 15]. For instance, Xu et al. developed a series of gas sensors based on SnO_2 thin films with varying concentrations of oxygen vacancies by annealing under different temperatures in an ambient atmosphere for the room-temperature detection of VOCs [16]. Their sensor demonstrated a high response of 150.5 towards 10 ppm trimethylamine. The exceptional gas-sensing performance was attributed to the regulation of oxygen vacancies, which dramatically enhanced the carrier concentration in the conduction band and provided additional adsorption sites for VOC detection. However, this method can only incorporate a limited concentration of oxygen vacancy into MOS, as annealing in an air atmosphere lacks strong reducibility.

In this chapter, CeO_2 nanowires with varying proportions of oxygen vacancies and Ce^{3+} ions are synthesized via a simple hydrothermal method followed by calcination under different controlled atmospheres (e.g., air, Ar, and 5%H_2+95%Ar). The nanowire morphology provides more adsorption sites for interactions between gas molecules and gas-sensing materials. Additionally, the valance states between Ce^{4+} and Ce^{3+} are regulated within the crystal structures, influencing the concentrations of oxygen species. This study focuses on the gas-sensing properties of the developed gas sensors and elucidates the room-temperature gas-sensing mechanism towards linalool. During storage, with the changes in circumstances (i.e., period, temperature, humidity, etc.), the sensory quality of rice deteriorates, displaying an unpleasant aroma profile. Consequently, the practicability of the developed gas sensor for analyzing rice quality is verified using two varieties of rice (indica and japonica rice) stored for various periods (1, 3, 5, 7, 15, and 30 days).

4.2 Experimental details

4.2.1 Chemicals

All chemicals used in this study are of analytical grade and were used directly without further purification. Deionized water (18 MΩ/cm) used in all experiments was prepared using an ultra-pure purification system (Aqua Solutions). Detailed information regarding the chemical formula, purity, and manufacturer is provided in Tab. 4.1.

Tab. 4.1 Chemical reagents used in this chapter.

Chemicals	Formula	Manufacturer	Purity
Cerium(III) chloride heptahydrate	$CeCl_3 \cdot 7H_2O$	Shanghai Aladdin Biochemical Technology Co., Ltd.	99.9%
Sodium hydroxide	NaOH	Shanghai Aladdin Biochemical Technology Co., Ltd.	96.0%
Ethanol	C_2H_5OH	Chinasun Specialty Products Co., Ltd.	99.7%
Linalool	$C_{10}H_{18}O$	Shanghai Aladdin Biochemical Technology Co., Ltd.	96%

4.2.2 Synthesis of CeO_2 nanowires

Oxygen engineering on CeO_2 nanowires was performed through a simple hydrothermal method combined with subsequent calcination, as schematically illustrated in Fig. 4.1. Typically, 0.5 g of $CeCl_3 \cdot 7H_2O$ was mixed with 20 mL of a 10 M NaOH aqueous solution and stirred continuously for at least 40 minutes. The resulting mixture was then sealed in a 50 mL Teflon-lined stainless steel autoclave and subjected to hydrothermal synthesis at 130 ℃ for 24 hours. After naturally cooling to room temperature, the solid precipitates were collected by centrifugation and rinsed alternately with deionized water and absolute ethanol to remove impurities. The cleaned precipitates were then dried in a vacuum oven at 70 ℃ for 24 hours. Finally, the dried precursors were annealed at 400 ℃ for 2 hours at a heating rate of 3 ℃/min under different controlled atmospheres (e.g., air, Ar, and 5%H_2+95%Ar). The samples obtained from these treatments are designated as S1 (air), S2 (Ar), and S3 (5%H_2+95%Ar), respectively.

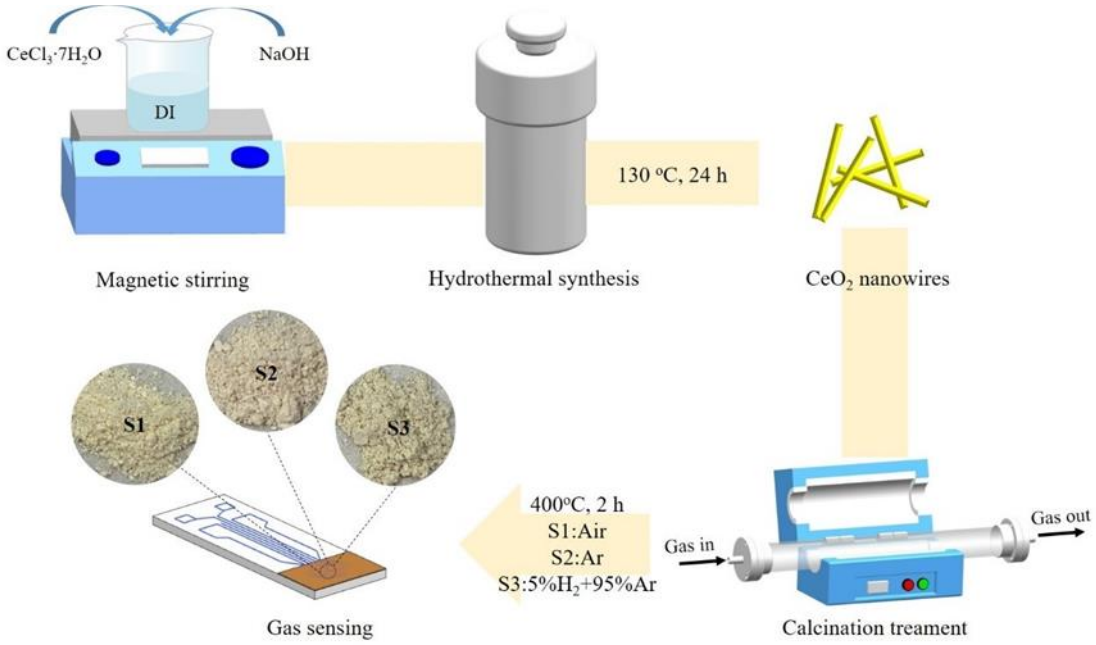

Fig. 4.1 Schematic illustration of oxygen vacancy engineering on CeO_2 nanowires.

4.2.3 Fabrication and measurement of gas sensor

The fabrication of gas sensors follows the procedure outlined in Section 3.2.3. Linalool is chosen as the target gas for this chapter, and its theoretical concentration is calculated using Eq. 2-1, considering the vapor pressure of linalool at 25 ℃ to be 0.17 mm Hg [17].

4.3 Results and discussion

4.3.1 Structural characterization

To investigate the impact of post-treatment under different controlled atmospheres on the structural evolution of CeO_2, the morphologies of the three samples were examined using FE-SEM. As shown in Fig. 4.2, all powders synthesized through a one-step hydrothermal method using $CeCl_3$ as the metal source and deionized water as the solvent exhibit a nanowire morphology with an average diameter of 50 ± 10 nm. This unique nanostructure features a high length-diameter ratio, providing a large contact area and superior physicochemical properties, resulting in a substantial surface-to-volume ratio [18, 19]. Despite partial fracture, the nanowire structure remains largely unchanged even after annealing under hydrogen-argon mixtures with strong reducibility. In addition, agglomeration effect is enhanced to reduce the surface tension of the gas-sensing materials, maintaining them in a relatively stable state. Variations in nanowire lengths may arise from formation during hydrothermal growth and intense ultrasonic

sample preparation before FE-SEM observation.

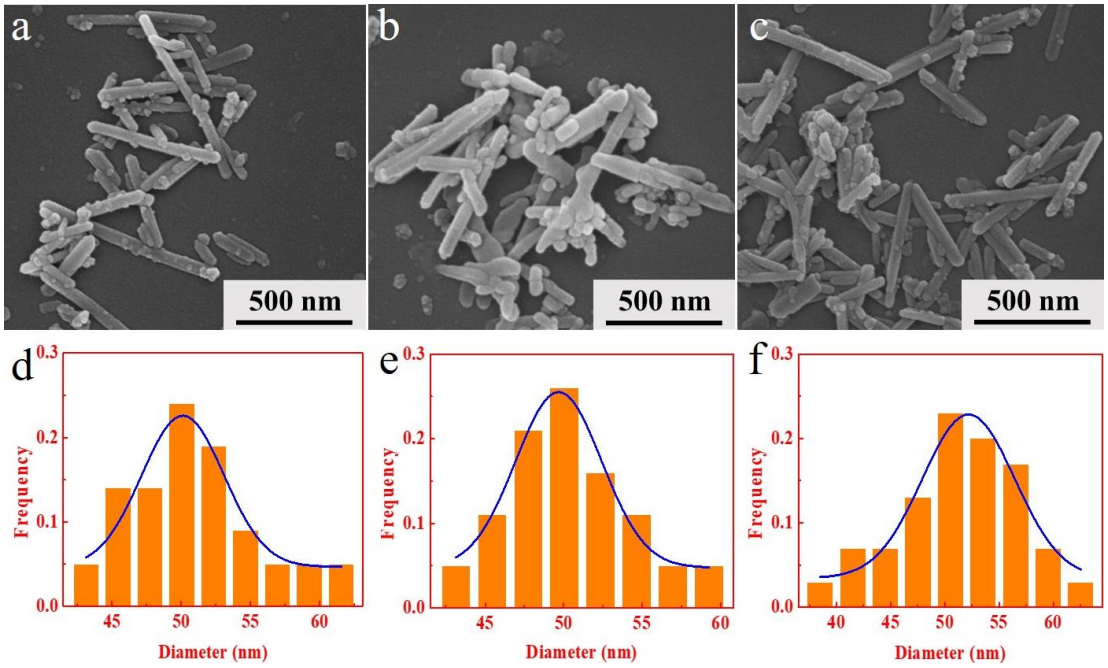

Fig. 4.2 FE-SEM images and diameter distributions of (a, d) S1, (b, e) S2, and (c, f) S3.

To investigate the crystal structures of CeO_2 nanowires, the TEM image of S1 is depicted in Fig. 4.3a, showcasing a uniform diameter distribution of the nanowires, consistent with the FE-SEM observations. Analysis of lattice fringe spacing, as shown in Fig. 4.3b, reveals spacing of 0.19 nm and 0.31 nm perpendicular to the growth direction, corresponding to the (2 2 0) and (1 1 1) crystal planes, respectively. The selected area electron diffraction image (Fig. 4.3c) confirms the crystalline nature of the synthesized sample, with a preferential growth direction along [1 1 0] [20]. Meanwhile, the HAADF-STEM image of S1 (Fig. 4.3d) and corresponding element mappings (Figs. 4.3e and 4.3f) demonstrate uniform distribution and co-existence of cerium (Ce) and oxygen (O) elements along the contour of the sample, validating successful synthesis and maintenance of CeO_2 nanowires through the hydrothermal method and subsequent calcination under different controlled atmospheres. Furthermore, exploring the formation mechanism of CeO_2 nanowires, Fig. 4.3g presents a schematic diagram illustrating the two-step process. At high concentrations of NaOH (10 M), rapidly hydrolysis generates abundant OH^- ions during hydrothermal synthesis, facilitating the thermal hydrolysis of cerium ions at 130 ℃ to form nanoparticles. Subsequently, these nanoparticles form nanowire structures with varying lengths through an oriented attachment mechanism. Most importantly, the high NaOH concentration may have a great influence on the stereo configuration of cerium complexation, resembling a cubic structure, which contributes to the formation of CeO_2 nanowires [21].

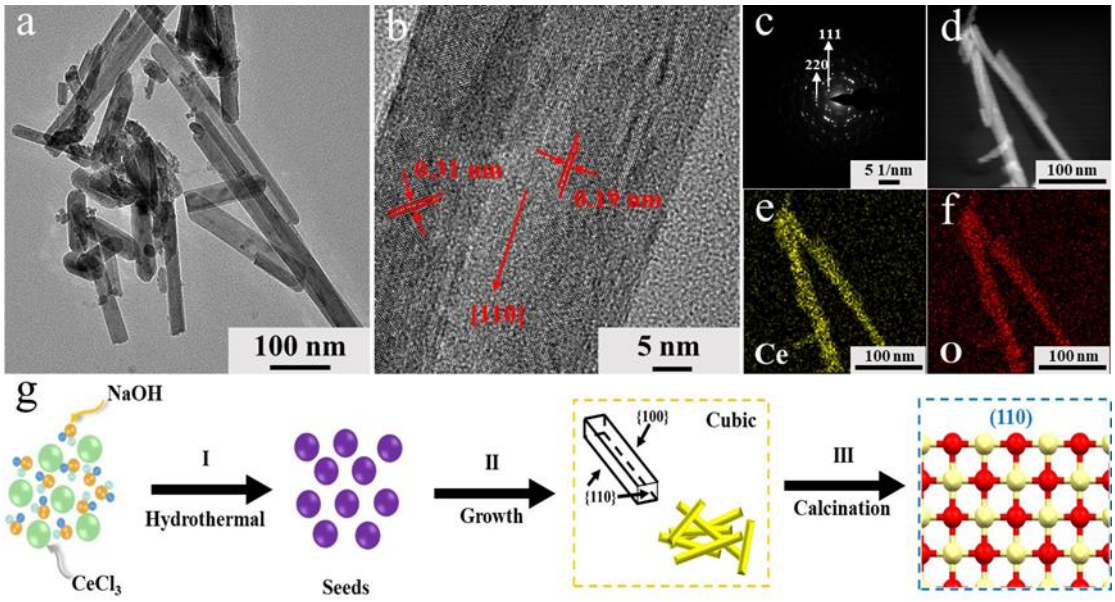

Fig. 4.3 (a) TEM and (b) HRTEM images, (c) SAED image, (d) HAADF-STEM image and (e-f) EDS mapping of S1, (g) schematic diagram of the formation mechanism of CeO_2 nanowires.

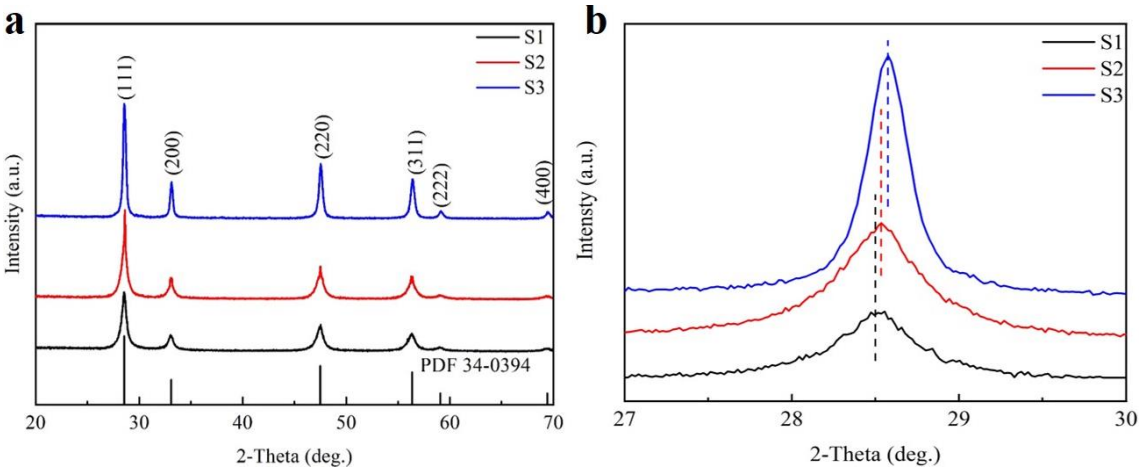

Fig. 4.4 (a) XRD pattern of S1, S2, and S3, and (b) slow scan of (111) peak

To examine the crystal structures of CeO_2 nanowires annealed under different controlled atmospheres, X-ray diffraction analysis is depicted in Fig. 4.4. It can be seen that the diffraction peaks align perfectly with the fluorite-type CeO_2, corresponding to the face-centered cubic phases (JCPDS No. 34-0394). Notably, there is no prominent shift observed in the XRD spectra, suggesting the preservation of the crystalline phase even under the atmosphere with strong reducibility. Compared with the sample annealed under air, the peaks of S2 and S3 become sharper and stronger, implying a higher crystallinity in these samples accompanied by an increase in the average crystallite size (Tab. 4.2). Besides, after the incorporation of oxygen vacancies, the diffraction peak

shifts to the right (Fig. 4.4b), indicating a correlation with the incorporation of different concentrations of oxygen vacancies into cerium oxides.

Tab. 4.2 Average crystallite sizes of S1, S2, and S3.

Sample	S1	S2	S3
Size/nm	10.26	10.99	20.21

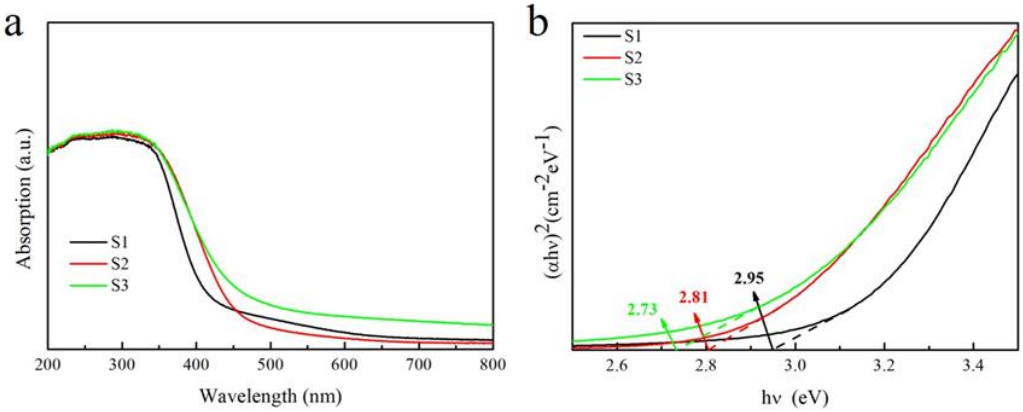

Fig. 4.5 (a) UV-Vis absorption spectra, and (b) Tauc plot of S1, S2, and S3.

It is reported that the incorporation of oxygen vacancies can effectively narrow the bandgap of MOS, thereby expanding the absorption range of gas-sensing materials. The ultraviolet-visible (UV-Vis) absorption spectra of all samples depicted in Fig. 4.5a were analyzed to gain detailed insights into their intrinsic performance. The spectra reveal a large absorption tail in the visible and near-infrared regions with a wavelength of less than 400 nm. Notably, the light absorption ability of S2 and S3 shows a significant red shift, with the absorption edge located near 430 nm. This shift can be attributed to the introduction of oxygen vacancies, broadening the range of light absorption. It is likely associated with free electrons and/or oxygen vacancy-induced polarons, indicating the existence of a large number of oxygen vacancies [11, 22]. Additionally, the bandgap of the three samples was calculated according to the Tauc formula (Eq. 4-1), as evident in Fig. 4.5b. The bandgap values for S1, S2, and S3 are 2.95, 2.81, and 2.73 eV, respectively. The introduction of oxygen vacancies dramatically reduces the bandgap, primarily due to the reduction of Ce^{4+} in CeO_2 to Ce^{3+}, leading to the high conductivity of oxygen ions [23].

$$\alpha h\gamma = A\times(h\gamma - E_g)^{1/2} \quad (4\text{-}1)$$

Where α is the absorption coefficient being a function of wavelength α(λ), h is the Planck constant, γ is frequency, A is a proportionality constant, and E_g is an optical band gap of metal oxides.

To further investigate the evolution of oxygen vacancy in the three samples, a Raman analysis was conducted. Fig. 4.6 reveals the Raman spectra of S1, S2, and S3 with a scanning range of 350-550 cm^{-1}. There is only one broad characteristic peak located at around 460 cm^{-1}, primarily originating from the Raman active vibrational mode of the fluorite-type structure of CeO_2 nanowires. Most importantly, it can be also seen from the figure that the Raman bands of S1, S2, and S3 are located at 459, 461, and 462 cm^{-1}, respectively. Compared with S1, the peaks of S2 and S3 slightly shift towards higher wavenumbers. The shift in the peak of S3 indicates elevated concentrations of oxygen vacancies due to the presence of a lower oxidation state of cerium ions (Ce^{3+}) in the samples [24].

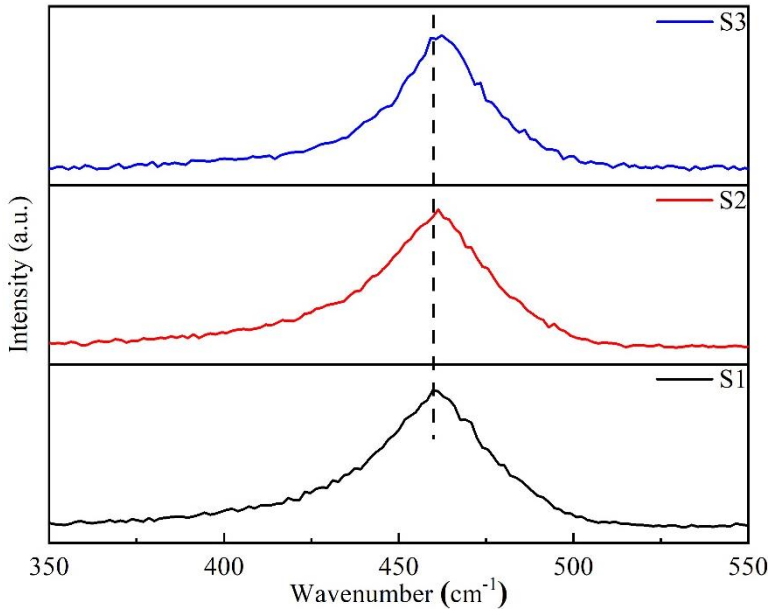

Fig. 4.6 Raman spectra of S1, S2, and S3.

To effectively confirm the chemical composition and oxidation states, XPS analyses were conducted. Figs. 4.7a-4.7c reveal the Ce 3d spectra of all synthesized samples. These spectra are fitted into the eight peaks, corresponding to two kinds of oxidation states of Ce ions. The peaks marked by u″ and v″ are attributed to the oxidation state of Ce^{3+}, whereas the peaks marked by u, u′, u‴, v, v′, and v‴ are assigned to Ce^{4+} [25, 26]. Ce^{3+} oxidation states indicate the existence of unsaturated chemical bonds and oxygen vacancies. According to Ref. [27], the integrated areas of Ce^{4+} and Ce^{3+} are calculated, as summarized in Tab. 4.3. Subsequently, the concentrations of Ce^{3+} in S1, S2, and S3 are estimated to be around 0.12, 0.17, and 0.19, respectively, as illustrated in Tab. 4.4. It is obvious that S3 exhibits a higher concentration of Ce^{3+} ions, which may be closely related to the positively charged Ce ions with accompanying charge-compensated electrons [28]. The generation of oxygen vacancies has been closely related to the interaction between metal oxides and hydrogen under high

annealing temperatures, leading to the loss of lattice oxygen bonded with Ce-O-Ce and the formation of oxygen vacancies based on the following process [29]. Consequently, the regulation of the electronic structures and surface chemical states of CeO_2 nanowires with different concentrations of oxygen vacancies via a simple method, including annealing the precursor under different controlled atmospheres, makes them promising materials for gas-sensing applications, particularly in the analysis of VOCs. Furthermore, the O 1s spectra demonstrated in Figs. 4.7d-4.7f are well-divided into three Gaussian-Lorenz peaks centered at round 528.6, 529.8, and 530.9 eV, representing lattice oxygen (O_L), surface chemisorbed oxygen (O_C), and oxygen vacancy (O_V), respectively [30]. The relative quantitative analysis of O 1s spectra is also illustrated in Tab. 4.4. The value of x' ($x' = [O_{1s}]/[Ce_{3d}]$) is smaller than that of x (x=[O]/[Ce]), further confirming that the formation of oxygen vacancies is accompanied by an increase of the relative proportion of Ce^{3+} ions. The presence of oxygen vacancies generates adequate adsorption sites, significantly enhancing the relative proportion of surface chemisorbed oxygen species participating in the gas-sensing process [14].

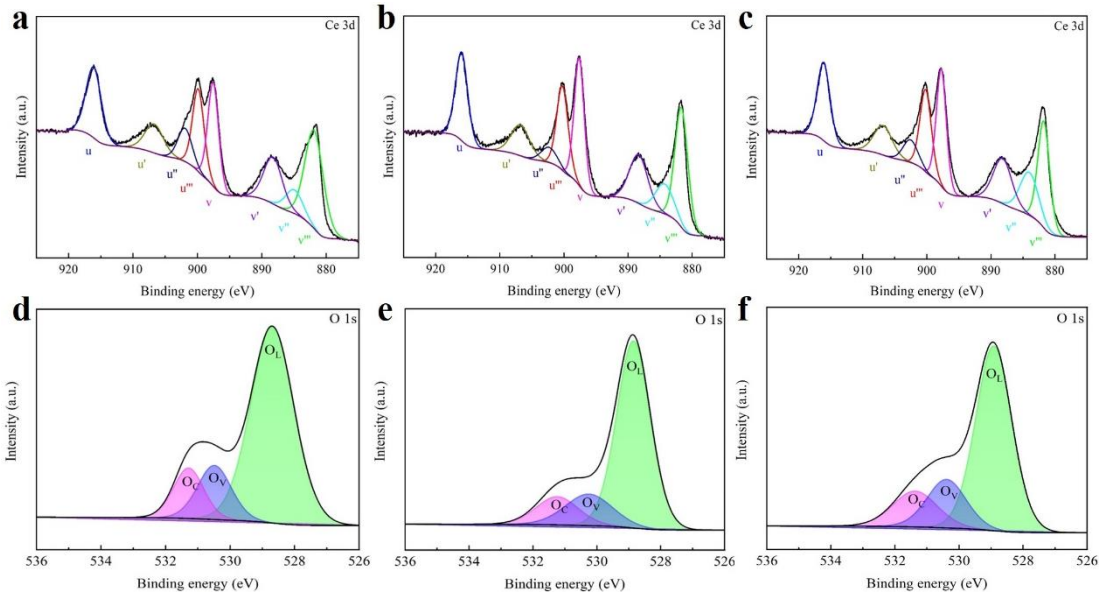

Fig. 4.7 XPS analysis of Ce 3d and O 1s spectra for (a, d) S1, (b, e) S2, and (c, f) S3.

Tab. 4.3 Integrated areas of individual XPS peaks of Ce 3d in S1, S2, and S3.

	Ce $3d_{3/2}$				Ce $3d_{5/2}$			
	u	u'	u''	u'''	v	v'	v''	v'''
S1	118785	56892	50114	92002	101392	192503	43524	115440
S2	58886	37291	14298	36116	63649	102068	68182	83519
S3	97436	66359	38520	104897	119308	158139	123977	142368

Tab. 4.4 Concentrations of Ce^{3+} and Ce^{4+} ions and stoichiometry ratios of CeO_2 nanowires annealed under different controlled atmospheres.

	Ce^{3+}	Ce^{4+}	O_L	O_C	O_V	x^a	x'^b
S1	0.12	0.88	0.72	0.12	0.16	1.94	1.91
S2	0.17	0.83	0.70	0.13	0.17	1.92	1.65
S3	0.19	0.81	0.66	0.15	0.19	1.91	1.34

Note: $^a x = [O]/[Ce] = 1.5Ce^{3+} + 2Ce^{4+}$, $^b x' = [O_{1s}]/[Ce_{3d}] = (A_O/A_{Ce}) \times (S_{Ce}/S_O)$, where $S_{Ce} = 7.399$, and $S_O = 0.711$.

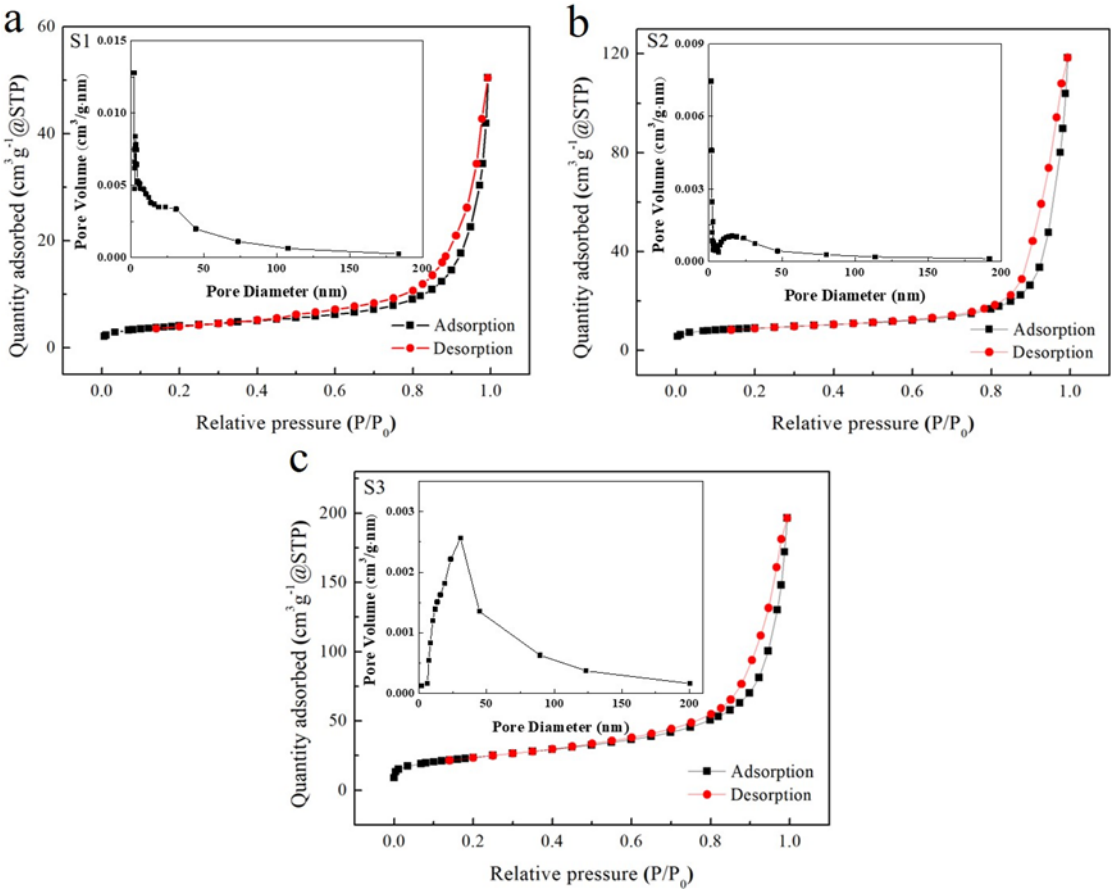

Fig. 4.8 Nitrogen adsorption-desorption isotherms and pore distributions of S1, S2, and S3.

The surface activities and porous structures of all samples were analyzed by the BET method, as revealed in Fig. 4.8. The specific surface areas and pore diameters of S1, S2, and S3 are demonstrated in Tab. 4.5. The adsorption-desorption curves of the three samples belong to type IV and have H3 hysteresis loops. The H3 hysteresis loop of S3 is clearer, which may be related to its larger mesoporous structure. The pore size distributions reveal that the maximum pore sizes of S1, S2, and S3 are 14.4, 21.4, and 22.2 nm, respectively. This further confirms that S3 has a larger pore size, which is advantageous for the adsorption and desorption of the target gas on the surface of the sensor during the gas-sensing process. In addition, the specific surface area of S1, S2,

and S3 is 15.5, 32.9, and 83.9 m^2/g, respectively, indicating that the surface chemical states are modified after annealing under different controlled conditions. Consequently, the sample with a high specific surface area facilitates the adsorption of gas molecules, contributing to enhancing the gas-sensing performance of S3.

Tab. 4.5 Specific surface areas and pore diameters of S1, S2, and S3.

Sample	S1	S2	S3
Specific surface area (m^2/g)	14.5	32.9	83.9
Pore diameter (nm)	14.4	21.4	22.2

4.3.2 Gas-sensing performance investigation

Based on the above-stated structural characterizations, the room-temperature gas-sensing properties of S1, S2, and S3 were comprehensively investigated. Fig. 4.9a shows the variations of electrical resistance of the sensors towards various concentrations of linalool. The resistance increases when exposed to the purified air and eventually displays a high state ranging from 1 to 10 GΩ. Once linalool is introduced into the testing chamber, the resistance decreases. When the purified air is released again, the resistance returns to the initial value (R_a), indicating that all gas sensors exhibit an n-type characteristic. Besides, the baseline resistance (R_a) of S1, S2, and S3 is 9.6, 7.62, and 2.33 GΩ, respectively. It can be seen that the resistance (R_a) of S2 and S3 decreases, which can be ascribed to the influence of oxygen vacancy, indicating a significant increase in the electron concentration. Normally, the electrons trapped in the donor level are directly excited into the conduction band of CeO_2 nanowires, increasing the carrier concentration of the conduction band, and eventually displaying a lower electrical resistance (R_a) [31, 32]. The fitting results between the response and linalool concentration are depicted in Fig. 4.9b. It is obvious that controlling the annealing atmosphere significantly affects the gas-sensing performance, and all gas sensors demonstrate an excellent positive linear correlation with the ppm-level linalool concentration, suggesting that the developed gas sensors have the ability to quantitatively analyze linalool. S3 reveals the highest response towards linalool. Specifically, the sensor response of S3 towards 20 ppm linalool at room temperature is 16.7, which is approximately 3.2 and 2.4 times higher than those of S1 and S2, respectively, indicating a significant increase in the sensor response. This enhancement is nearly similar to the sequence of increasing oxygen vacancy concentration measured by XPS (Tab. 4.4), primarily due to the presence of oxygen vacancies efficiently increasing the concentration of surface chemisorbed oxygen species, contributing to an increase in response. Besides, the specific surface area of S3 illustrated in Fig. 4.8 is

83.95 m^2/g, which is much larger than those of S1 (14.54 m^2/g) and S2 (32.91 m^2/g). A higher specific surface area can provide adequate sites for the adsorption of linalool molecules, contributing to the improvement of the response of MOS-based gas sensors. Meanwhile, it is worth noting that the S3-based gas sensor is not inclined to be saturated even if the concentration of linalool is up to 20 ppm, indicating that the developed gas sensor can detect linalool at a wide range. Hence, it turns out that S3 shows excellent room-temperature gas-sensing performance and is also available for a wide range of concentrations of linalool sensing. Based on Ref. [33], the detection limit of S3 towards linalool is calculated to be approximately 540 ppb.

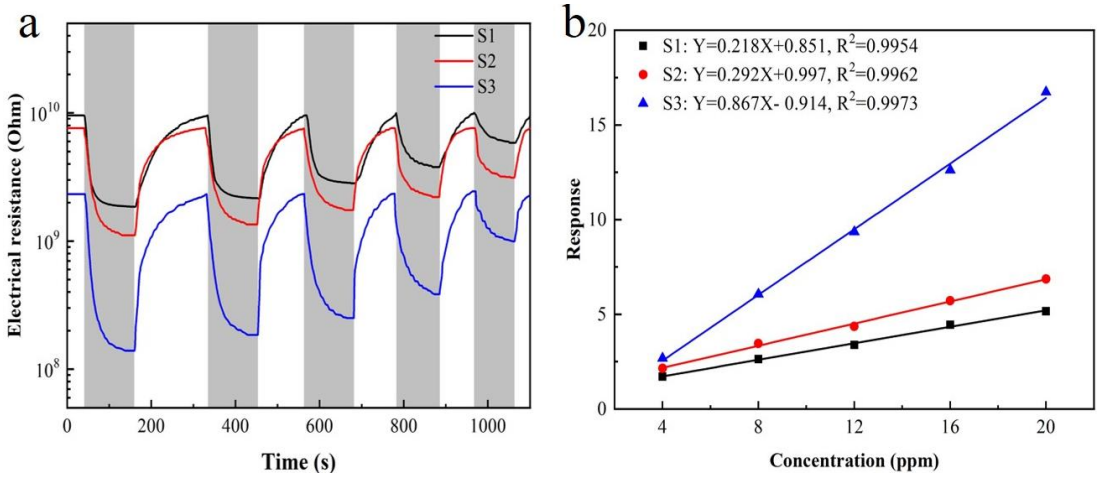

Fig. 4.9 (a) Changes in resistance of gas sensors towards 4-20 ppm linalool, and (b) linear relationship between sensor response and gas concentration.

To comprehensively evaluate the room-temperature gas-sensing performance of the developed gas sensors, the dynamic gas-sensing performance of all samples was also analyzed. Fig. 4.10 shows the response-recovery curves of S1, S2, and S3 towards 20 ppm linalool at room temperature. It can be calculated that the response time (τ_{res}) and recovery time (τ_{rec}) are 26 and 144 s for S1, 21 and 131 s for S2, 16 and 121 s for S3, respectively. At this point, the short τ_{res} of the sensor may be due to its high specific surface areas providing more active adsorption sites, facilitating the rapid diffusion of linalool among the CeO_2 sensing materials. Then it should also be noted that the τ_{rec} of the sensor is still relatively long compared to the traditional heated semiconductor-based gas sensors, primarily because the energy obtained from room temperature is much lower than the activation energy for the desorption of linalool molecules [34]. After the comprehensive comparison, it is found that the S3-based gas sensor with the highest proportion of oxygen vacancies displays excellent gas-sensing properties towards the target gas at room temperature, with the highest sensor response and the shortest response/recovery times.

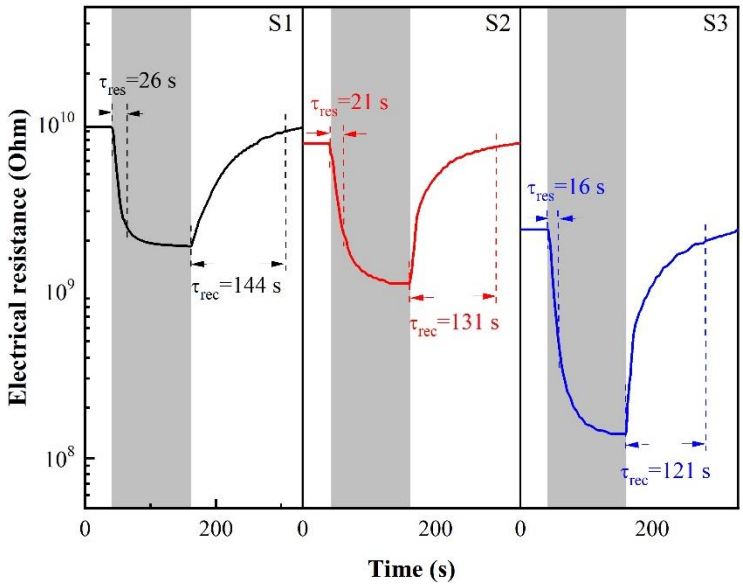

Fig. 4.10 Dynamic response-recovery curves of S1, S2, and S3 towards 20 ppm linalool.

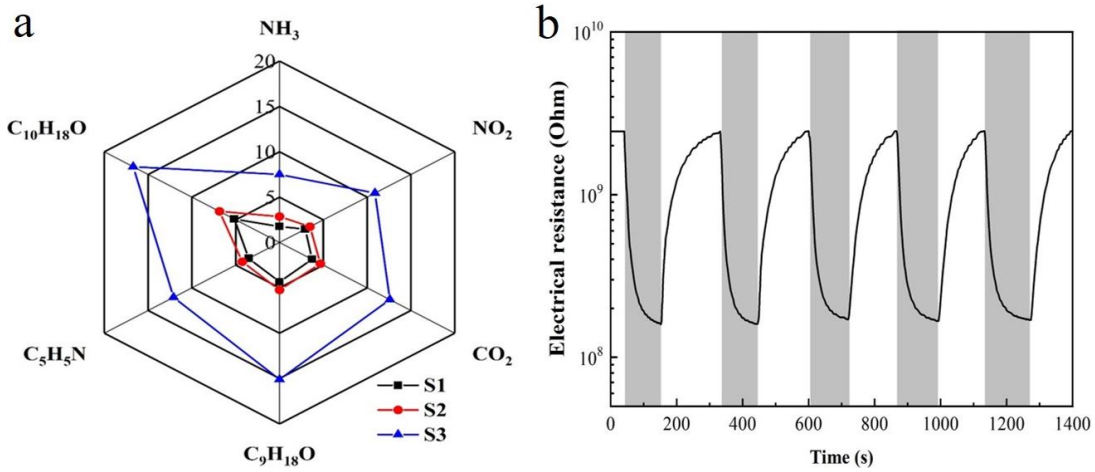

Fig. 4.11 (a) Response of S1, S2, and S3-based gas sensors towards 20 ppm interfering gases, and (b) reproducibility of S3 towards 20 ppm.

In view of the practical application of the developed gas sensors, apart from the indices including sensor response and response/recovery times, an outstanding capability is to distinguish linalool from other interfering gases [35]. The selectivity of all gas sensors towards 20 ppm of different kinds of interfering gases, including NH_3, NO_2, CO_2, $C_9H_{19}O$, and C_5H_5N, is evident in Fig. 4.11a. These results indicate the S3-based gas sensor has superior selectivity towards linalool. This is primarily because the ethyl groups in linalool has the highest electron-donating ability among various atmospheres [16]. Besides, more oxygen vacancies in S3 can promote the adsorption of linalool molecules, which is due to the strong electron affinity interaction between the target gas molecules with oxygen vacancy [36]. Consequently, linalool molecules are more easily adsorbed onto the CeO_2 sensing materials and react with its surface

chemisorbed oxygen species to reach a higher response. Moreover, the sensor responses to 20 ppm linalool are measured within five cycles to verify the repeatability of S3, and the result is shown in Fig. 4.11b. There are no obvious changes in both baseline resistance (R_a) and sensor response. From the data obtained from the figure, it can be calculated that the deviation of sensor response and baseline resistance (R_a) of the S3-based gas sensor is 6.8% and 1.8%, respectively. Obviously, both of them are less than 10%, indicating the excellent repeatability of the sensor in the analysis of the target gas.

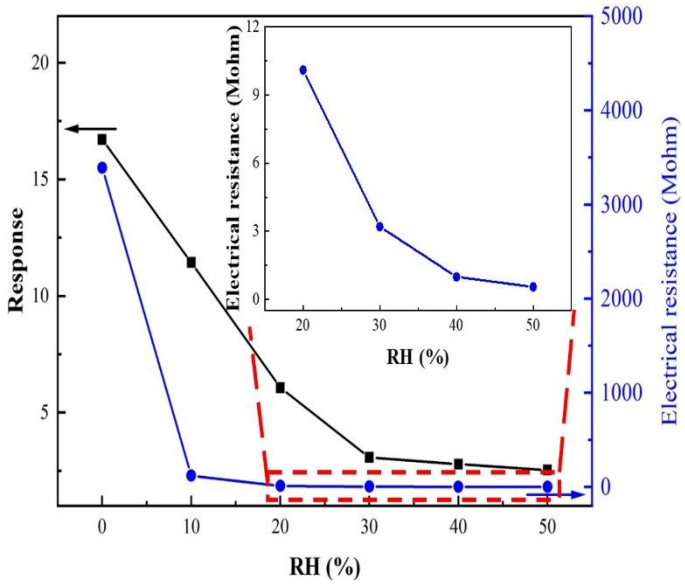

Fig. 4.12 Changes in both response and resistance of the S3-based gas sensor towards 20 ppm linalool under various relative humidity atmospheres.

It is well-recognized that humidity can exert a substantial influence on the application of MOS-based gas sensors in practical applications. As depicted in Fig. 4.12, the sensor response and the baseline resistance (R_a) towards 20 ppm linalool under various relative humidity values are calculated to investigate the effect of relative humidity on S3. As the relative humidity increases, the sensor response and baseline resistance (R_a) accordingly decrease. Notably, with the relative humidity ranging from 0% to 30%, the sensor response significantly decreases from 16.7 to 3.1. The baseline resistance decreases by 99%. Meanwhile, it can be seen that when the relative humidity further reaches over 30%, the decrease in both sensor response and baseline resistance is very limited. The gas-sensing performance degradation is chiefly owing to the adsorption of water molecules occupying the majority of the adsorption sites, decreasing the number of active sites for the interaction between linalool molecules and oxygen species [37]. Besides, the surface chemisorbed oxygen species that reacted with water molecules are mainly responsible for the decrease in the resistance [38]. As the relative humidity further increases, the adsorption of water molecules on the surface of CeO_2 nanowires becomes saturated, with a limited impact on the adsorption of gas

molecules. Hence, when the relative humidity exceeds 30%, the changes in both sensor response and baseline resistance are almost narrower.

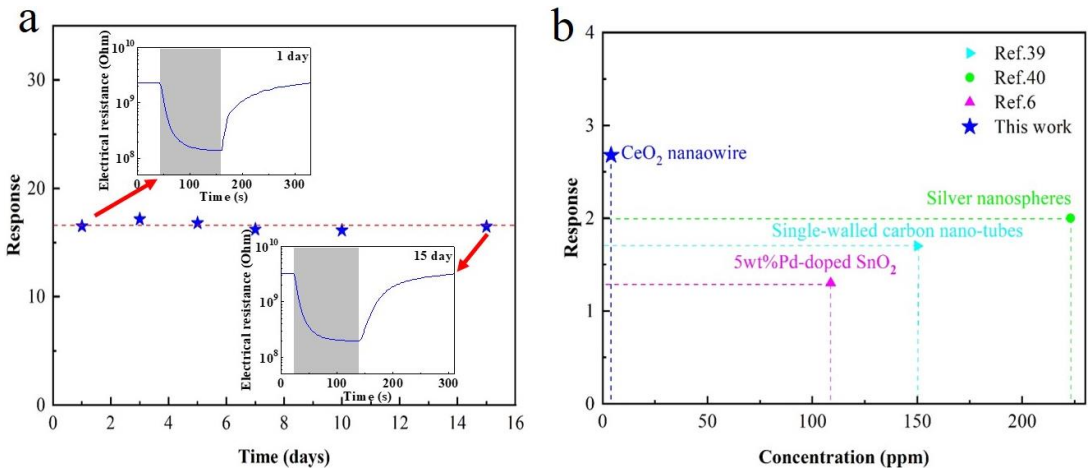

Fig. 4.13 (a) Long-term stability of the S3-based gas sensor towards 20 ppm linalool, and (b) gas-sensing performance compared with other state-of-the-art linalool sensors.

Long-term stability is also a crucial factor for further evaluating the service life of the developed gas sensors. Fig. 4.13a shows the long-term stability of the S3-based gas sensor towards 20 ppm linalool at room temperature. There is no obvious attenuation and fluctuation in both sensor response and baseline resistance towards 20 ppm linalool within 15 days, demonstrating superior long-term stability. Additionally, the gas-sensing performance compared with other state-of-the-art linalool sensors operating at a low temperature (150 ℃) or room temperature is shown in Fig. 4.13b, and detailed information containing its morphology, response, and working temperature in the analysis of linalool is demonstrated in Tab. 4.6. This suggests that S3 with extensive oxygen vacancies still displays an excellent sensor response even at a lower concentration of linalool. Hence, it is a competitive linalool sensor, which can be employed to inspect rice aging.

In conclusion, the S3-based gas sensor demonstrates exceptional room-temperature gas-sensing performance for linalool, including high sensitivity, selectivity, stability, and a low limit of detection. These characteristics make it a promising candidate for practical applications such as monitoring the aging process of rice, where detecting volatile organic compounds like linalool is essential. The superior performance is attributed to the high specific surface area, extensive oxygen vacancies, and optimized surface chemical states of the CeO_2 nanowires, which collectively enhance the adsorption and reaction of linalool molecules on the sensor's surface.

Tab. 4.6 Detail information on gas-sensing performance in comparison with other state-of-art linalool sensors.

Material	Morphology	Conc.	Tem.	Res.	Ref.
Single-walled carbon	nanotubes	150 ppm	RT	1.7	[39]
Ag	nanospheres	223 ppm	RT	2	[40]
Pd-doped SnO_2	nanocomposites	110 ppm	150 ℃	1.3	[6]
CeO_2	nanowires	4 ppm	RT	2.6	This work

Note: Conc., Concentration; Tem., Temperature, Res., Response; RT, room temperature.

4.3.3 Gas-sensing mechanism

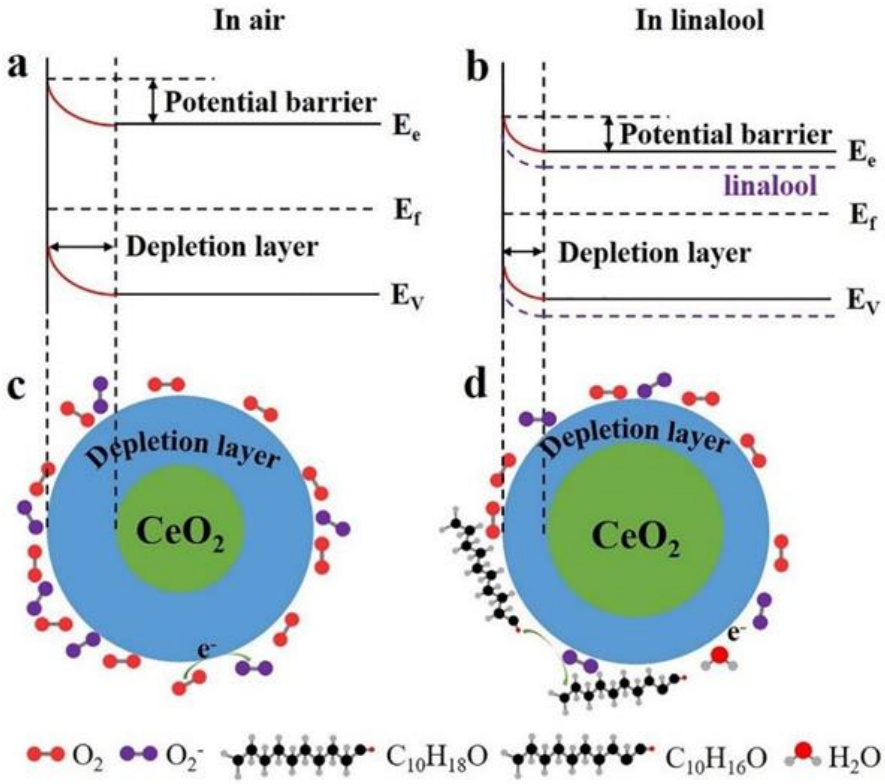

Fig. 4.14 Schematic illustration of the room-temperature gas-sensing mechanism of CeO_2-based gas sensors (a, c) in air and (b, d) in linalool.

The room-temperature gas-sensing mechanism of CeO_2 nanowires towards pp,-level linalool can be elucidated based on the characteristic space charge model of n-type metal oxides. This mechanism is schematically depicted in Fig. 4.14. Specifically, when the CeO_2-based gas sensor is exposed to purified air, oxygen molecules from the air are adsorbed onto the surface of CeO_2 nanowires. These oxygen molecules capture free electrons from the conduction band of CeO_2, forming adsorbed oxygen species (O_2^-) [41]. This process creates an electron depletion region near the surface and increases

the potential barrier (Figs. 4.14a and 4.14c). The capture of electrons by oxygen molecules reduces the electron concentration in CeO_2, leading to an increase in the sensor's resistance [42, 43]. When linalool molecules ($C_{10}H_{18}O$) are introduced into the sensing environment, they first get adsorbed onto the surface of CeO_2 nanowires, transforming from gas phases ($C_{10}H_{18}O$ (gas)) to adsorbed phase ($C_{10}H_{18}O$ (ads)), as shown in Eq. 4-3 [11]. Subsequently, a redox reaction occurs between the adsorbed linalool molecules ($C_{10}H_{18}O$ (ads)) and the adsorbed oxygen species (O_2^-) at room temperature. This reaction is depicted in Eq. 4-4. During this reaction, linalool loses hydrogen atoms (producing $C_{10}H_{16}O$ (ads), water vapor (H_2O (gas) is released, and free electrons (e^-) are generated)). The release of electrons onto the conduction band of CeO_2 decreases the thickness of the depletion region and lowers the potential barrier [44]. This reduction in the depletion region and potential barrier results in an increase in the electron concentration within the CeO_2 nanowires, which subsequently decreases the sensor's electrical resistance [45, 46].

$$C_{10}H_{18}O\ (gas) \rightarrow C_{10}H_{18}O\ (ads) \quad (4\text{-}3)$$

$$2C_{10}H_{18}O\ (ads) + O_2^-\ (ads) \rightarrow 2C_{10}H_{16}O\ (ads) + 2H_2O\ (gas) + e^- \quad (4\text{-}4)$$

The enhanced room-temperature gas-sensing performance of the S3-based gas sensor for linalool sensing can be attributed to several key factors: the nanowire morphology, high specific surface area, and increased percentages of chemisorbed oxygen and oxygen vacancy components. In detail, the CeO_2 nanowires exhibit a high surface-to-volume ratio, which facilitates the efficient transmission and diffusion of linalool molecules across the sensor surface. This structure enhances the interaction between the gas molecules and the sensing materials, leading to improved sensitivity. Secondly, S3 possesses a significantly higher specific surface area of 83.95 m^2/g compared to S1 and S2 (Tab. 4.5). This large surface area provides more active sites for the adsorption of linalool molecules, thereby increasing the sensor response [47, 48]. The high surface area allows for more effective interaction between the gas molecules and the sensor surface, enhancing the overall sensing performance. Thirdly, XPS analysis (Tab. 4.4) indicates that S3 has a higher relative proportion of chemisorbed oxygen and oxygen vacancy components compared to S1 and S2. Chemisorbed oxygen species play a crucial role in the gas-sensing mechanism by reacting with the target gas, while oxygen vacancies provide additional adsorption sites, facilitating the redox reactions necessary for sensing. The presence of oxygen vacancies is associated with the substitution of Ce^{4+} by Ce^{3+}, which helps maintain charge balance [49, 50], and increases the proportion of oxygen vacancies. This substitution process releases negative charges into the conduction band, enhancing carrier concentrations and improving the sensor's electrical properties [51, 52].

4.3.4 Practical application of CeO_{2-x}-based gas sensors

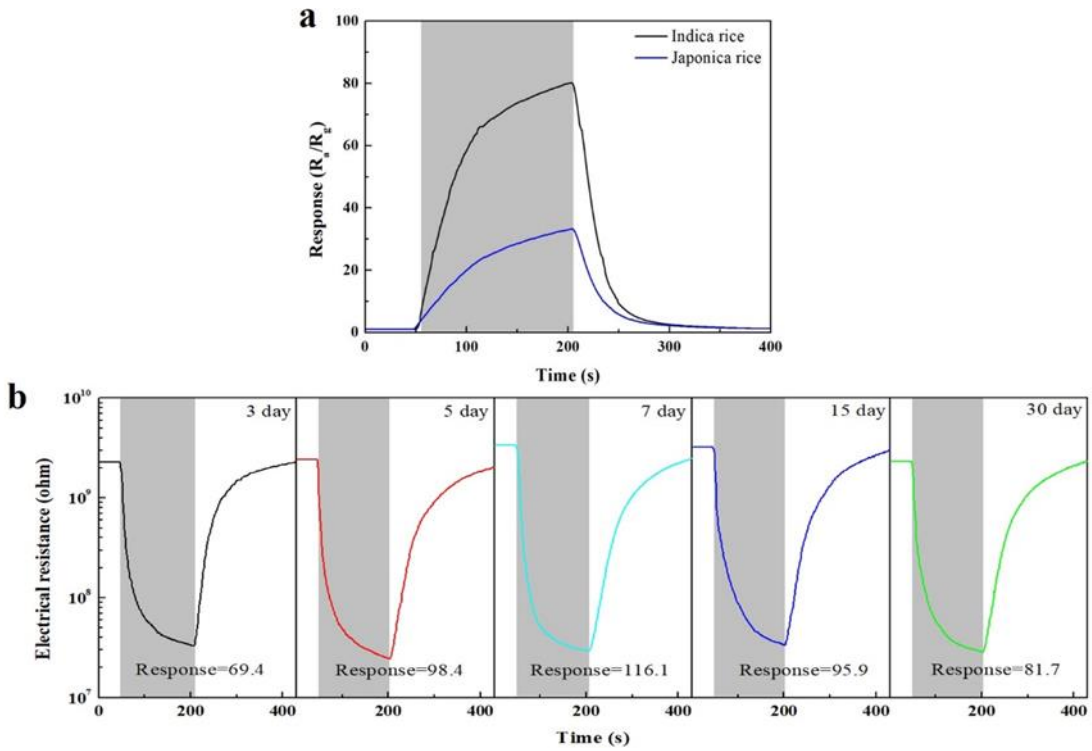

Fig. 4.15 (a) Response measured under exposure towards VOCs generated from indica rice and japonica rice, (b) response towards VOCs generated from 30 g indica rice stored for various periods.

To verify the practicability of the developed CeO_{2-x}-based gas sensors for inspecting rice quality during storage, the variations in the electrical resistance of the S3-based sensor were monitored when exposed to VOCs generated by two kinds of rice (indica rice and japonica rice) stored for various periods (1, 3, 5, 7, 15, and 30 days). Fig. 4.15a displays the sensor response to VOCs from both types of rice during aging. Notably, the response towards the VOCs from indica rice aging is significantly higher (80.2) compared to japonica rice (36.1), demonstrating the sensor's ability to distinguish between the two types. This suggest that the S3-based sensor is effective in identifying the quality of different rice varieties based on VOC emissions. Additionally, as depicted in Fig. 4.15b, the sensor response and baseline resistance (R_a) to VOCs from indica rice stored for different storage periods (3, 5, 7, 15, and 30 days) exhibit minimal fluctuation. This consistency aligns with the long-term stability tests (Fig. 4.15a), indicating reliable sensor performance over extended periods. During the continuous testing lasting for 30 days, there is no significant change in the sensor response, which is chiefly because of the slow aging process of indica rice stored at room temperature. It is reported that rice undergoes significant aging after being stored at room temperature for six months to a year. In addition, variables such as temperature, pressure,

and humidity during testing can impact sensor response, underscoring the importance of controlled testing conditions. Above all, these results demonstrate that the sensor may be utilized as the detection unit of high-performance E-nose for room-temperature detection of alcohol.

4.4 Conclusions

In this chapter, oxygen vacancies of CeO_2 nanowires, synthesized by a simple hydrothermal method, are regulated by post-treatment under different controlled atmospheres (e.g., air, Ar, and 5%H_2+95%Ar). Then they were employed for the detection of linalool, a key alcohol generated during rice aging, at room temperature. The structural characterizations and gas-sensing performance investigations were conducted to investigate the influence of post-treatment under different atmospheres on the enhanced gas-sensing performance of CeO_2-based gas sensors. The main conclusions drawn from this research are summarized as follows:

(1) The microstructural analyses revealed that the nanowire morphology of the samples remained largely unchanged even after annealing under strong reducing atmospheres (5%H_2+95%Ar). XRD analysis indicated that all samples maintained a crystalline phase, with S2 and S3 displaying sharper and stronger peaks, implying a higher crystallinity.

(2) The formation mechanism of CeO_2 nanowires involves rapid hydrolysis of Ce ions under high NaOH concentration, resulting in nanoparticles that subsequently form nanowire structures through an oriented attachment mechanism. These nanostructures exhibit a high length-diameter ratio, large contact area, and superior physicochemical properties.

(3) Ce 3d spectrum analysis revealed that annealing under strong reducing atmospheres incorporates oxygen vacancies into the CeO_2 nanowires, partially reducing Ce^{4+} ions to Ce^{3+}. This incorporation leads to an increase in crystal defects and oxygen vacancies, significantly enhancing the number of active sites for gas adsorption and improving the room-temperature gas-sensing performance.

(4) The S3-based gas sensor showed superior gas-sensing properties towards linalool, including a high response of 16.74, a response/recovery time of 16/121 s, and a low theoretical detection limit of 540 ppb. Comparative analysis with recent literature indicates that CeO_2 nanowires, especially those annealed under strong reducing atmospheres, are capable of detecting linalool at room temperature even at low concentrations.

(5) The elevated gas-sensing properties of S3 are attributed to its unique nanowire structure, higher specific surface area, and increased proportions of chemisorbed oxygen and oxygen vacancy components. The nanowire structure provides a large

surface-to-volume ratio, facilitating the transmission and diffusion of linalool. XPS analysis revealed the highest proportions of chemisorbed oxygen and oxygen vacancies in S3, enhancing the reactivity with linalool. The partial reduction of Ce^{4+} to Ce^{3+} increases the concentration of oxygen vacancies, contributing to charge balance and enhancing carrier concentration.

(6) Practical experiments demonstrated that the S3-based gas sensor could effectively distinguish between VOC generated by indica and japonica rice aging at room temperature. The sensor response and baseline resistance (Ra) showed minimal fluctuation over extended storage periods, indicating excellent long-term stability. These findings highlight the effectiveness of regulating electronic structures and surface chemical states in CeO_2 nanowires for improving room-temperature gas-sensing performance. Collectively, these results underscore the significant potential of the developed CeO_{2-x}-based gas sensor in practical applications, particularly for monitoring rice aging and possibly other VOC detection scenarios at room temperature.

References

[1] X.Q. Hu, L. Lu, Z.L. Guo, Z.W. Zhu. Volatile compounds, affecting factors and evaluation methods for rice aroma: A review. Trends in Food Science & Technology, 97 (2020) 136-146. https://doi.org/10.1016/j.tifs.2020.01.003.

[2] Y. Arbid, M. Sleiman, C. Richard. Photochemical interactions between pesticides and plant volatiles. Science of the Total Environment, 807 (2022) 150716. https://doi.org/10.1016/j.scitotenv.2021.150716.

[3] H.W. Qin, S.B. Yang, M.Q. Yang, Y.Z. Wang, T.M. Yang, J.Y. Zhang. Effects on volatile oil and volatile compounds of Amomum tsao-ko with different pre-drying and drying methods. Industrial Crops and Products, 174 (2021) 114168. https://doi.org/10.1016/j.indcrop.2021.114168.

[4] J. Shi, Y.Q. Nian, D.D. Da, X.L. Xu, G.H. Zhou, D. Zhao, C.B. Li. Characterization of flavor volatile compounds in sauce spareribs by gas chromatography-mass spectrometry and electronic nose. LWT, 124 (2020) 109182. https://doi.org/10.1016/j.lwt.2020.109182.

[5] J.Y. Xu, K.W. Liu, C. Zhang. Electronic nose for volatile organic compounds analysis in rice aging. Trends in Food Science & Technology, 109 (2021) 83-93. https://doi.org/10.1016/j.tifs.2021.01.027.

[6] P. Kakoty, M. Bhuyan, K. Das. Performance of Pd doped SnO_2 as sensing material for tea aromatic chemicals. IEEE Sensors Journal, 18 (2018) 4392-4398. https://doi.org/10.1109/JSEN.2018.2827119.

[7] F.A. Jan, Wajidullah, R. Ullah, N. Ullah, Salman, M. Usman. Exploring the environmental and potential therapeutic applications of Myrtus communis L. assisted synthesized zinc oxide (ZnO) and iron doped zinc oxide (Fe-ZnO) nanoparticles. Journal of Saudi Chemical Society, 25 (2021) 101278. https://doi.org/10.1016/j.jscs.2021.101278.

[8] J.S. Liu, Y.X. Zhen, X.F. Zhang, Z.P. Deng, Y.M. Xu, L.H. Huo, S. Gao. Bio-template synthesis of CeO_2 ultrathin nanosheets for highly selective and sensitive detection of ppb-level p-xylene vapor. Ceramics International, 48 (2022) 1550-1559. https://doi.org/10.1016/j.ceramint.2021.09.234.

[9] W.T. Yang, X. Wang, S.Y. Song, H.J. Zhang. Syntheses and applications of noble-metal-free CeO_2-based mixed-oxide nanocatalysts. Chem, 5 (2019) 1743-1774. https://doi.org/10.1016/j.chempr.2019.04.009.

[10] L. Lyu, Q. Xie, Y.Y. Yang, R.R. Wang, W.F. Cen, S.Y. Luo, W.S. Yang, Y. Gao, Q.Q. Xiao, P. Zou, Y. Yang. A novel CeO_2 hollow-shell sensor constructed for high sensitivity of acetone gas detection. Applied Surface Science, 571 (2022) 151337. https://doi.org/10.1016/j.apsusc.2021.151337.

[11] C. Zhang, J.Y. Xu, H.P. Li, H.L. Liao. Role of ruthenium incorporation on room-temperature nonanal sensing properties of Ru-loaded urchin-like $W_{18}O_{49}$ hierarchical nanostructure. Sensors and Actuators B: Chemical, 353 (2022) 131096. https://doi.org/10.1016/j.snb.2021.131096.

[12] J.S. Liu, B.Y. Song, J. Huang, Z.P. Deng, X.F. Zhang, Y.M. Xu, L.H. Huo, S Gao. Absorbent cotton derived mesoporous CeO_2 hollow tubule for enhanced detection of p-xylene at low energy consumption. Journal of Alloys and Compounds, 873 (2021) 159774. https://doi.org/10.1016/j.jallcom.2021.159774.

[13] D.E. Motaung, Z.P. Tshabalala, P.R. Makgwane, F.A. Mahmoud, D.N. Oosthuizen, F.R. Cummings, N. Leshabane, N. Hintsho-Mbita, X.G. Li, S.S. Ray, H.C. Swart. Multi-functioning of CeO_2-SnO_2 heterostructure as room temperature ferromagnetism and chemiresistive sensors. Journal of Alloys and Compounds, 906 (2022) 164317. https://doi.org/10.1016/j.jallcom.2022.164317.

[14] H. Yuan, S.A.A.A. Aljneibi, J. Yuan, Y. Wang, H. Liu, J. Fang, C. Tang, X. Yan, H. Cai, Y. Gu, S.J. Pennycook, J. Tao, D. Zhao. ZnO nanosheets abundant in oxygen vacancies derived from metal-organic frameworks for ppb-level gas sensing. Advanced Materials, 31 (2019) 1807161. https://doi.org/10.1002/adma.201807161.

[15] Y.C. Huan, K.D. Wu, C.J. Li, H.L. Liao, M. Debliauy, C. Zhang. Micro-nano structured functional coatings deposited by liquid plasma spraying. Journal of Advanced Ceramics, 9 (2020) 517-534. https://doi.org/10.1007/s40145-020-0402-9.

[16] Y.S. Xu, L.L. Zheng, C. Yang, W. Zheng, X.H. Liu, J. Zhang. Oxygen vacancies enabled porous SnO_2 thin films for highly sensitive detection of triethylamine at room temperature. ACS Applied Materials & Interfaces, 12 (2020) 20704-20713. https://doi.org/10.1021/acsami.0c04398.

[17] https://www.chemicalbook.com/ProductChemicalPropertiesCB5347184_EN.htm.

[18] J.P. Meng, Z. Li. Schottky-contacted nanowire sensors. Advanced Materials, 32 (2020) 2000130. https://doi.org/10.1002/adma.202000130.

[19] H. Liu, H.Y. Zhang, W.H. Zhu, M.L. Bo, T.T. Zhao. Crystalline-to-amorphous phase transformation in CuO nanowires for gaseous ionization and sensing application. ACS Sensors, 6 (2021) 4118-4125. https://doi.org/10.1021/acssensors.1c01638.

[20] G.N. Li, B. Wang, D.E. Resasco. Water promotion (or inhibition) of condensation reactions depends on exposed cerium oxide catalyst facets. ACS Catalysis, 10 (2020) 5373-5382. https://doi.org/10.1021/acscatal.0c01009.

[21] S. Cao, N. Sui, P. Zhang, T.T. Zhou, J.C. Tu, T. Zhang. TiO_2 nanostructures with different crystal phases for sensitive acetone gas sensors. Journal of Colloid and Interface Science, 607 (2022) 357-366. https://doi.org/10.1016/j.jcis.2021.08.215.

[22] H.Y. Chen, L.Z. Song, S.X. Ouyang, J.B. Wang, J. Lv, J.H. Ye. Co and Fe codoped

$WO_{2.72}$ as alkaline-solution-available oxygen evolution reaction catalyst to construct photovoltaic water splitting system with solar-to-hydrogen efficiency of 16.9%. Advanced Science, 6 (2019) 1900465. https://doi.org/10.1002/advs.201900465.

[23] T.H. Wondimu, G.C. Chen, H.Y. Chen, D.M. Kabtamu, A.W. Bayeh, K.C. Wang, H.C. Huang, C.H. Wang. High catalytic activity of oxygen-vacancy-rich tungsten oxide nanowires supported by nitrogen-doped reduced graphene oxide for the hydrogen evolution reaction. Journal of Materials Chemistry A, 6 (2018) 19767-19774. https://doi.org/10.1039/C8TA07000H.

[24] W. Gao, Z.Y. Zhang, J. Li, Y.Y. Ma, Y.Q. Qu. Surface engineering on CeO_2 nanorods by chemical redox etching and their enhanced catalytic activity for CO oxidation. Nanoscale, 7 (2015) 11686-11691. https://doi.org/10.1039/C5NR01846C.

[25] H.M. Sun, C.Y. Tian, G.L. Fan, J.N. Qi, Z.T. Liu, Z.H. Yan, F.Y. Cheng, J. Chen, C.P. Li, M. Du. Boosting activity on Co_4N porous nanosheet by coupling CeO_2 for efficient electrochemical overall water splitting at high current densities. Advanced Functional Materials, 30 (2020) 1910596. https://doi.org/10.1002/adfm.201910596.

[26] R. Hassandoost, S. Pouran, A. Khataee, Y. Orooji, S.W. Joo. Hierarchically structured ternary heterojunctions based on Ce^{3+}/Ce^{4+} modified Fe_3O_4 nanoparticles anchored onto graphene oxide sheets as magnetic visible-light-active photocatalysts for decontamination of oxytetracycline. Journal of Hazardous Materials, 376 (2019) 200-211. https://doi.org/10.1016/j.jhazmat.2019.05.035.

[27] S. Putla, M.H. Amin, B.M. Reddy, A. Nafady, K.A. Al Farhan, S.K. Bhargava. MnO_x nanoparticle dispersed CeO_2 nanocubes: A remarkable heteronanostructured system with unusual structural characteristics and superior catalytic performance. ACS Applied Materials & Interfaces, 7 (2015) 16525-16535. https://doi.org/10.1021/acsami.5b03988.

[28] S. Cong, Y.Y. Yuan, Z.G. Chen, J.Y. Hou, M. Yang, Y.L. Su, Y.Y. Zhang, L. Li, Q.W. Li, F.X Geng, Z.G. Zhao. Noble metal-comparable SERS enhancement from semiconducting metal oxides by making oxygen vacancies. Nature Communications, 6 (2015) 7800. https://doi.org/10.1038/ncomms8800.

[29] A.W. Bayeh, G.Y. Lin, Y.C. Chang, D.M. Kabtamu, G.C. Chen, H.Y. Chen, K.C. Wang, Y.M. Wang, T.C. Chiang, H.C. Huang, C.H. Wang. Oxygen-vacancy-rich cubic CeO_2 nanowires as catalysts for vanadium redox flow batteries. ACS Sustainable Chemistry & Engineering, 8 (2020) 16757-16765. https://doi.org/10.1021/acssuschemeng.0c03861.

[30] H. Bi, L.X. Zhang, Y. Xing, P. Zhang, J.J. Chen, J. Yin, L.J. Bie. Morphology-controlled synthesis of CeO_2 nanocrystals and their facet-dependent gas sensing

properties. Sensors and Actuators B: Chemical, 330 (2021) 129374. https://doi.org/10.1016/j.snb.2020.129374.

[31] Y. Zhao, C. Chang, F. Teng, Y. Zhao, G. Chen, R. Shi, G. Waterhouse, W. Huang, T. Zhang. Defect-engineered ultrathin δ-MnO_2 nanosheet arrays as bifunctional electrodes for efficient overall water splitting. Advanced Energy Materials, 7 (2017) 1700005. https://doi.org/10.1002/aenm.201700005.

[32] N. Luo, C. Wang, D. Zhang, M.M. Guo, X.H. Wang, Z.X. Cheng, J.Q. Xu. Ultralow detection limit MEMS hydrogen sensor based on SnO_2 with oxygen vacancies. Sensors and Actuators B: Chemical, 354 (2022) 130982. https://doi.org/10.1016/j.snb.2021.130982.

[33] C. Zhang, Y. Li, G.F. Liu, K.W. Liu, K.D. Wu. Room temperature NO_2 sensing properties of $ZnO_{1-\alpha}$ coating prepared by hydrogen reduction method. Ceramics International, 47 (2021) 29873-29880. https://doi.org/10.1016/j.ceramint.2021.07.160.

[34] D.X. Ju, H.Y. Xu, Z.W. Qiu, Z.C. Zhang, Q. Xu, J. Zhang, J.Q. Wang, B.Q. Cao. Near room temperature, fast-response, and highly sensitive triethylamine sensor assembled with Au-loaded ZnO/SnO_2 core-shell nanorods on flat alumina substrates. ACS Applied Materials & Interfaces, 7 (2015) 19163-19171. https://doi.org/10.1021/acsami.5b04904.

[35] C. Huang, S. Adimi, D. Liu, H. Guo, T. Thomas, J. P. Attfield, S. Ruan, F. Qu, M. Yang. Mesoporous titanium niobium nitrides supported Pt nanoparticles for highly selective and sensitive formaldehyde sensing. Journal of Materials Chemistry A, 9 (2021) 19840-19846. https://doi.org/10.1039/D1TA02433G.

[36] T.S. Wang, S.Y. Liu, P. Sun, Y.C. Wang, K. Shimanoe, G.Y. Lu. Unexpected and enhanced electrostatic adsorption capacity of oxygen vacancy-rich cobalt-doped In_2O_3 for high-sensitive MEMS toluene sensor. Sensors and Actuators B: Chemical, 342 (2021) 129949. https://doi.org/10.1016/j.snb.2021.129949.

[37] F.D. Qu, S.D. Zhang, C.Z. Huang, X.Y. Guo, Y. Zhu, T. Thomas, H.C. Guo, J.P. Attfield, M.H. Yang. Surface functionalized sensors for humidity-independent gas detection. Angewandte Chemie-International Edition, 60 (2021) 6561-6566. https://doi.org/10.1002/ange.202015856.

[38] H. Bai, H. Guo, J. Wang, Y. Dong, B. Liu, F. Guo, D. Chen, R. Zhang, Y. Zheng. Hydrogen gas sensor based on SnO_2 nanospheres modified with Sb_2O_3 prepared by one-step solvothermal route. Sensors and Actuators B: Chemical, 331 (2021) 129441. https://doi.org/10.1016/j.snb.2021.129441.

[39] H. Wang, P. Ramnani, T. Pham, C.C. Villarreal, X.J. Yu, G. Liu, A. Mulchandani. Gas biosensor arrays based on single-stranded DNA-functionalized single-walled carbon nanotubes for the detection of volatile organic compound biomarkers released by Huanglongbing disease-infected citrus trees. Sensors, 19 (2019) 4795.

https://doi.org/10.3390/s19214795.

[40] T. Shahar, G. Feldheim, S. Marx, D. Mandler. Core-shell nanoparticles for gas phase detection based on silver nanospheres coated with a thin molecularly imprinted polymer adsorbed on a chemiresistor. Nanoscale, 10 (2018) 17593-17602. https://doi.org/10.1039/C8NR01437J.

[41] H.P. Liang, L.P. Guo, N.J. Cao, H.Y. Hu, H. Li, de N.F. Rooij, A. Umar, H. Algarni, Y. Wang, G.F. Zhou. Practical room temperature formaldehyde sensing based on a combination of visible-light activation and dipole modification. Journal of Materials Chemistry A, 9 (2021) 23955-23967. https://doi.org/10.1039/D1TA06346D.

[42] C. Zhang, Y.C. Huan, Y. Li, Y.F. Luo, M. Debliquy. Low concentration isopropanol gas sensing properties of Ag nanoparticles decorated In_2O_3 hollow spheres. Journal of Advanced Ceramics, 11 (2022) 379-391. https://doi.org/10.1007/s40145-021-0530-x.

[43] J.H. Ma, Y. Ren, X.R. Zhou, L.L. Liu, Y.H. Zhu, X.W. Cheng, P.C. Xu, X.X. Li, Y.H. Deng, D.Y. Zhao. Pt nanoparticles sensitized ordered mesoporous WO_3 semiconductor: Gas sensing performance and mechanism study. Advanced Functional Materials, 28 (2018) 1705268. https://doi.org/10.1002/adfm.201705268.

[44] C. Zhang, Y. Li, G.F. Liu, H.L. Liao. Preparation of ZnO_{1-x} by peroxide thermal decomposition and its room temperature gas sensing properties. Rare Metals, 41 (2022) 871-876. https://doi.org/10.1007/s12598-021-01840-y.

[45] J. Wang, F.M. Chen, Q. Guo, Y. Meng, M.R. Jiang, C.S. Wu, J. Zhuang, D.W. Zhang. Light-addressable square wave voltammetry (LASWV) based on a field-effect structure for electrochemical sensing and imaging. ACS Sensors, 6 (2021) 1636-1642. https://doi.org/10.1021/acssensors.1c00170.

[46] A. Sadeghzadeh-Attar. Photocatalytic degradation evaluation of N-Fe codoped aligned TiO_2 nanorods based on the effect of annealing temperature. Journal of Advanced Ceramics, 9 (2020) 107-122. https://doi.org/10.1007/s40145-019-0353-1.

[47] J. Li, M. Yang, X.L. Cheng, X.F. Zhang, C.Y. Guo, Y.M. Xu, S. Gao, Z. Major, H. Zhao, L.H. Huo. Fast detection of NO_2 by porous SnO_2 nanotoast sensor at low temperature. Journal of Hazardous Materials, 419 (2021) 126414. https://doi.org/10.1016/j.jhazmat.2021.126414.

[48] D. Liu, X.W. Ren, Y.S. Li, Z.L. Tang, Z.T. Zhang. Nanowires-assembled WO_3 nanomesh for fast detection of ppb-level NO_2 at low temperature. Journal of Advanced Ceramics, 9 (2020) 17-26. https://doi.org/10.1007/s40145-019-0343-3.

[49] H.T. Bui, S. Weon, J.W. Bae, E.J. Kim, B. Kim, Y.Y. Ahn, K. Kim, H. Lee, W. Kim. Oxygen vacancy engineering of cerium oxide for the selective photocatalytic

oxidation of aromatic pollutants. Journal of Hazardous Materials, 404 (2021) 123976. https://doi.org/10.1016/j.jhazmat.2020.123976.

[50] J. Lee, Y. Choi, B.J. Park, J.W. Han, H.S. Lee, J.H. Park, W. Lee. Precise control of surface oxygen vacancies in ZnO nanoparticles for extremely high acetone sensing response. Journal of Advanced Ceramics, 11 (2022) 769-783. https://doi.org/10.1007/s40145-022-0570-x.

[51] Y. Li, Y.L. Lu, K.D. Wu, D.Z. Zhang, M. Debliquy, C. Zhang. Microwave-assisted hydrothermal synthesis of copper oxide-based gas-sensitive nanostructures. Rare Metals, 40 (2021) 1477-1493. https://doi.org/10.1007/s12598-020-01557-4.

[52] M.S. Yao, W.H. Li, G. Xu Metal-organic frameworks and their derivatives for electrically-transduced gas sensors. Coordination Chemistry Reviews, 426 (2021) 213479. https://doi.org/10.1016/j.ccr.2020.213479.

Chapter 5 Rationally designed zinc stannate heterojunctions by solution precursor plasma spraying for 2-undecaone detection

5.1 Introduction

2-Undecanone is a significant ketone derived from the oxidative degradation of unsaturated fatty acids during rice aging [1-3]. The concentration of 2-undecanone in rice increases with the oxidation rate of fatty acids over time, making it a reliable indicator for evaluating rice quality. Currently, methods like headspace solid-phase micro-extraction coupled with gas chromatography-mass spectroscopy and near-infrared spectroscopy have been extensively available for identifying 2-undecanone concentration in rice aging [4-6].

To effectively address the shortcomings of traditional instrument methods, MOS-based gas sensors have been widely developed for monitoring VOC [7, 8]. Most MOSs have a wide bandgap, resulting in optimal working temperatures generally above 200 ℃. This temperature range is problematic for detecting 2-undecanone due to its pyrolysis point being below the working temperature, leading to its degradation before detection. As a result, there have been no reported uses of oxides for 2-undecanone sensing. Among various metal oxides, zinc stannate ($ZnSnO_3$) has emerged as a promising material for VOC monitoring. $ZnSnO_3$ is an n-type metal oxide with notable properties, such as low visible adsorption (bandgap ~3.1-3.9 eV), high electrical conductivity (~100 $S \cdot cm^{-1}$), and significant electron mobility (~10-15 $cm^2 \cdot V^{-1} \cdot S^{-1}$). These attributes make $ZnSnO_3$ a potential candidate for gas-sensing applications [9]. $ZnSnO_3$ can be fabricated into various morphologies such as porous, core-shell, hierarchical structures, which are generally responsible for enhancing gas-sensing performance. For instance, Cao et al. prepared $ZnSnO_3$ thin films with mesoporous structures through magnetron sputtering [10], and their gas-sensing measurements revealed a high sensor response of 11.5 towards 50 ppm ethanol at an optimal working temperature of 290 ℃. The large specific surface areas of mesoporous structures were chiefly responsible for this superior gas-sensing performance. Recently, metal oxides with dual-mesoporous structures have attracted significant interest. These structures enhance pore connectivity compared to mono-mesoporous structures, facilitating the transmission of gas molecules dominated by Knudsen diffusion and promoting interaction with active absorption sites. Ma et al. synthesized transition metal oxides with dual-mesoporous structures via a co-assembly approach and applied them to 3-hydroxy-2-butanone sensors [11], achieving a response of 1.4 even at an ultra-low concentration (50 ppb), which was superior to previously reported gas sensors. Furthermore, the existence of

dual-mesoporous structures prevents pore blockage caused by particle migration, making them favorable for gas-sensing applications involving gas-solid interface reactions. Nevertheless, the creation of secondary pores in porous materials generally involves complex procedures using templates like silica, polymers, or surfactants. To overcome this, a more general and convenient route is proposed for fabricating dual-mesoporous $ZnSnO_3$.

On the other hand, heterojunction construction is a recognized effective tactic to boost the gas-sensing performance of metal oxides. By creating heterojunctions, the band structure of metal oxides can be modified, which can reduce the working temperature and enhance the gas-sensing response. Wang et al. utilized nano-TiO_2 decoration to reduce the working temperature of a sensor based on $ZnSnO_3$ [12]. This was achieved because the impurity energy bands generated at the bottom of the conduction band merged with it to form band tails, thereby reducing the bandgap. This reduction means less energy is required to excite electrons into the conduction band, making the sensor more efficient at lower temperatures due to the heterojunctions formed at the interfaces between TiO_2 and $ZnSnO_3$. Additionally, modulating the electronic structures and surface chemical states, especially by incorporating oxygen vacancies, is another effective route to develop high-performance gas sensors. The formation of oxygen vacancies in $ZnSnO_3$ decreases its bandgap, which improves the efficiency of electron transfer. This, in turn, reduces the working temperature and enhances the response. For example, hollow cubic $ZnSnO_3$ with a controllable concentration of oxygen vacancies was synthesized by Wang et al. through a simple hydrothermal combined with an alkali etching method [13]. Their experiments displayed that $ZnSnO_3$ with 21.1% oxygen vacancies had dramatically enhanced gas-sensing properties compared to pristine $ZnSnO_3$ nanocubes without etching. Notably, the working temperature decreased by 12%, and the sensor response increased by 400%. Inspired by these findings, combining heterojunction construction with the incorporation of oxygen vacancies may be an effective optimization strategy for reducing the working temperature and enhancing the response of $ZnSnO_3$ in detecting 2-undecanone. Typically, achieving this involves at least two steps. Heterojunctions are first prepared through various chemical synthesis routes to create interfaces, and then the obtained solid precipitates are treated by processes such as annealing under different controlled atmospheres or etching for varying durations to incorporate oxygen vacancies. Despite the successes of these methods, they have some drawbacks, such as slow particle growth and insufficient crystal defects, which can limit the enhancement of gas-sensing performance of $ZnSnO_3$.

Owing to its notable advantages including ultra-high temperature (exceeding 10,000 K), extremely rapid cooling rate (10^5-10^7 K/s), and reducing atmosphere (H_2), plasma spray can serve as a feasible technique for fabricating $ZnSnO_3$ with porous

heterostructures and highly concentrated oxygen vacancies [14, 15]. Among them, the different volatilization rates of Zn and Sn atoms during the rapid cooling process result in the formation of heterojunctions within $ZnSnO_3$ material. Meanwhile, the small radius of the O atom at its site makes the $ZnSnO_3$ structure unstable, promoting the formation of oxygen vacancies, especially under the high-temperature conditions of the plasma spray. Furthermore, the reducing atmosphere (H2) further facilitates the generation of a large number of oxygen vacancies on the surface of $ZnSnO_3$, enhancing its gas-sensing properties. In this chapter, high-performance gas sensors are fabricated by integrating dual-mesoporous structures, heterojunction construction, and controlled concentrations of oxygen vacancies. The solution precursor plasma spray (SPPS) technique is employed using corresponding precursors to achieve the desired ZnSnO3 structures. This method allows for precise control over the formation of dual-mesoporous structures, heterojunctions, and oxygen vacancies. Then the gas-sensing performance of the fabricated ZnSnO3 sensors is thoroughly investigated at room temperature, focusing on the detection of ppm-level 2-undecanone. In addition, the practicability of the developed gas sensor is verified by evaluating the quality of two varieties of rice (indica and japonica rice) stored for different periods. These results confirm that the sensor can effectively monitor rice quality, making them suitable for incorporation into high-performance E-nose for room-temperature detection of VOCs.

5.2 Experimental details

5.2.1 Chemicals

All chemicals used in this study are analytical reagents and were used directly without further purification. The deionized water (18 MΩ/cm) employed in all experiments was prepared using an ultra-pure purification system (Aqua Solutions). Detailed information on the chemicals is provided in Tab. 5.1.

Tab. 5.1 Chemical reagents used in this chapter.

Chemicals	Formula	Manufacturer	Purity
Zinc nitrate hydrate	$Zn(NO_3)_2{\cdot}6H_2O$	Sigma Aldrich Chemie GmbH (Germany)	98.0%
Tin (IV) chloride pentahydrate	$SnCl_4{\cdot}5H_2O$	Sigma Aldrich Chemie GmbH (Germany)	98.0%
2-undecanone	$C_{11}H_{22}O$	Shanghai Aladdin Biochemical Technology Co., Ltd.	99.0%

5.2.2 Fabrication and measurement of gas sensors

The metal precursors, $Zn(NO_3)_2{\cdot}6H_2O$ and $SnCl_4{\cdot}5H_2O$, were dissolved in deionized water at a molar ratio of 1:1 to form saturated aqueous solutions with a concentration of 0.3 M under continuous stirring. For the plasma spraying deposition process, a plasma torch (F4, Oerlikon Metco, Switzerland) served as the heat source and was mounted on a six-axis robotic arm (ABB, Switzerland) for depositing the nanocrystals onto commercial alumina oxide plates measuring 22×28×1 mm^3. As schematically shown in Fig. 5.1, the solutions were injected into the plasma jet via a stainless steel needle, with pressurized nitrogen acting as the driving gas. The parameters of SPPS process are outlined in Tab. 5.2. Notably, to rationally design porous nanostructures and highly concentrated oxygen vacancies in the samples, the secondary plasma gas (hydrogen) was varied at rates of 1, 3, and 5 L/min. The corresponding samples are labeled as H1, H3, and H5, respectively.

The gas-sensing coatings were directly deposited onto the surfaces of the sensor substrates using SPPS. 2-Undecanone, selected as the target gas for this study due to its significance as a biomarker of rice aging, was utilized the gas-sensing experiments. The theoretical concentration of 2-undecanone was calculated using Eq. 2-1, where the vapor pressure of 2-undecanone vapors at 25 ℃ is 0.1 mm Hg.

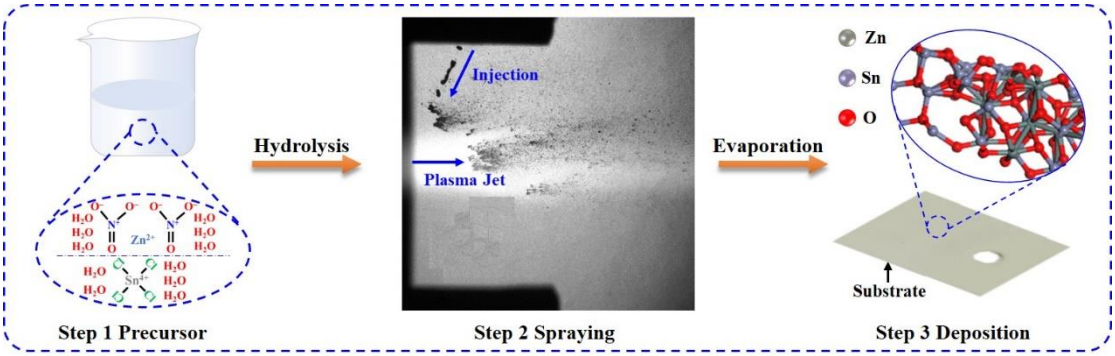

Fig. 5.1 Schematic illustration of the plasma spraying deposition.

Tab. 5.2 Spraying parameters for $ZnO/ZnSnO_3$ nanoscale heterojunctions by SPPS.

Parameter/Unit	Value
Current/A	580
Ar flow/L·min^{-1}	35
H_2 flow/L·min^{-1}	1, 3, 5
Spray distance/mm	90
Substrate preheating temperature/℃	400
Solution flow rate/mL·min^{-1}	28

5.2.3 Theoretical calculation

All spin-polarization density functional theory (DFT) calculations were conducted within the generalized gradient approximation (GGA) framework, utilizing the Perdew-Burke-Emzerhof (PBE) formulation. Grimme's DFT-D3 methodology was employed to describe dispersion interactions. The calculations accounted for valence electrons using a plane wave basis expansion with an energy cutoff of 450 eV. Partial occupancies of the Kohn-Sham orbitals were permitted, employing the Gaussian smearing method with a width of 0.05 eV to enhance computational efficienct. Self-consistent calculations were carried out with a convergence energy threshold of 10^{-5} eV to ensure accuracy. In this study, the crystal structures of the materials were determined based on XRD patterns. In detail, $ZnSnO_3$ was found to possess an ilmenite-like structured and crystallizes in the trigonal R3c space group. On the other hand, ZnO exhibits a Wurtzite structure and crystallizes in the hexagonal P63mc space group.

5.3 Results and discussion

5.3.1 Structural characterization

In Fig. 5.1, the uniform transparent solutions containing $Zn(NO_3)_2{\cdot}6H_2O$ and $SnCl_4{\cdot}5H_2O$ precursors with a molar ratio of 1:1 are successfully injected into the plasma jet, as confirmed by SprayCam equipment. The parameters for the liquid injection are detailed in Tab. 5.2. Subsequently, the molten droplets condense on the surface of the substrate, forming gas-sensing coatings with different thicknesses. This formation process involves several stages, including evaporation, precipitation, pyrolysis, and melting, as schematically illustrated in Fig. 5.2.

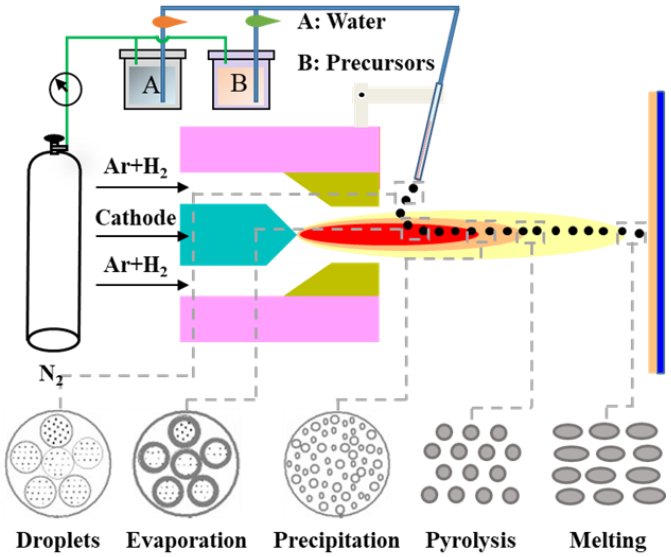

Fig. 5.2 Schematic illustration of the evolution of the gas-sensing coatings.

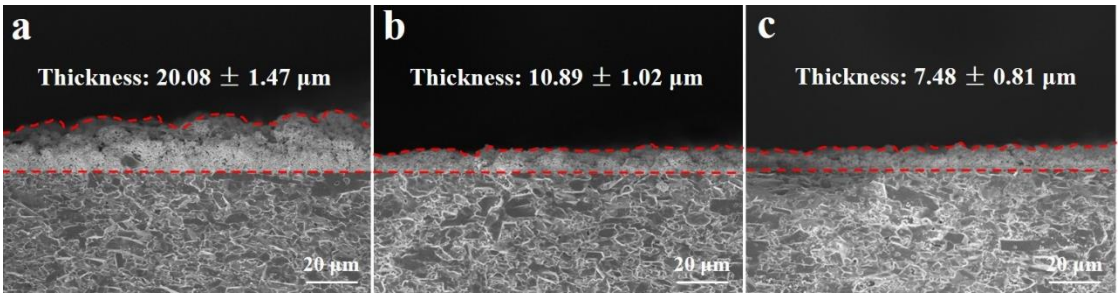

Fig. 5.3 Cross-sectional profiles of H1, H3, and H5-based gas-sensing coatings.

According to the cross-sectional profiles depicted in Fig. 5.3, the thickness of H1 is measured to be 20.08 ± 1.47 μm, making it the thickest among other samples. In contrast, H3 has a thickness of 10.89 ± 1.02 μm, while H5 is the thinnest at 7.48 ± 0.81 μm. H1 also exhibits a higher surface roughness compared to the other samples. This variation in thickness and surface roughness is primarily attributed to the change in hydrogen flow, which affects the energy density of the plasma jet. Consequently, the efficiency of the precursors entering the plasma jet decreases even under the same spraying conditions, resulting in variations in thickness and surface roughness that subsequently affect the gas-sensing performance [16-18]. FE-SEM images shown in Figs. 5.4a-5.4c provide further insight into the morphologies of the gas-sensing coatings. At hydrogen flows of 1 and 3 L/min, a large number of minor pores with nanometer-sized dimensions are observed on the surface, displaying highly porous structures. In contrast, the structure of H5 appears denser. This change is attributed to the significant increase in energy density of the plasma jet with higher hydrogen flow. Under the propulsion of the plasma jet, molten droplets impact the substrate to form flattened nanoparticles with higher energy and velocity. Subsequently, those nanoparticles tightly connect to form a dense coating. These unique nanoporous structures offer abundant active sites and shorter diffusion distances, facilitating electron transport and diffusion of gas molecules, ultimately leading to higher response and shorter response time [19-21].

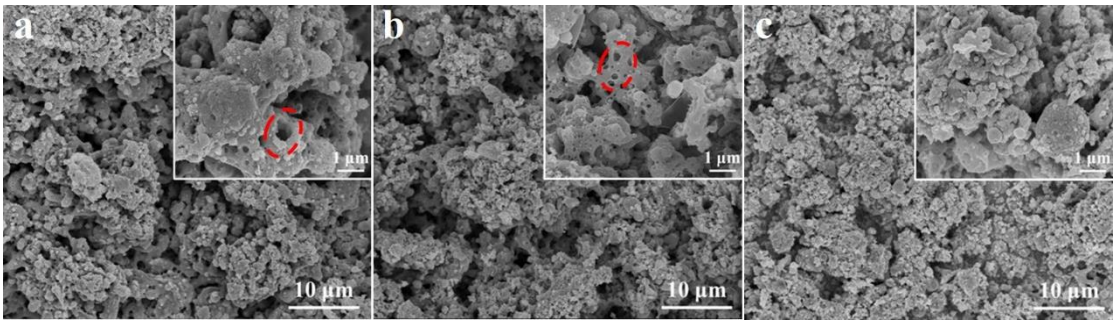

Fig. 5.4 FE-SEM images of H1, H3, and H5-based gas-sensing coatings.

The morphology and elemental distribution of the H3-based gas-sensing coating were further characterized by TEM, as evident in Fig. 5.5. The sample is composed of a variety of nanoparticles with an average size of 41.5 ± 9.4 nm (Figs. 5.5a and 5.5b), which is in agreement with the results obtained from FE-SEM observations. In addition, in Figs. 5.5d-5.5f, the EDS elemental mapping distributions reveal that the sample consists of Zn, Sn, and O, with all elements uniformly scattered along the contour of the sample. This confirms that the gas-sensing coatings are successfully deposited by SPPS.

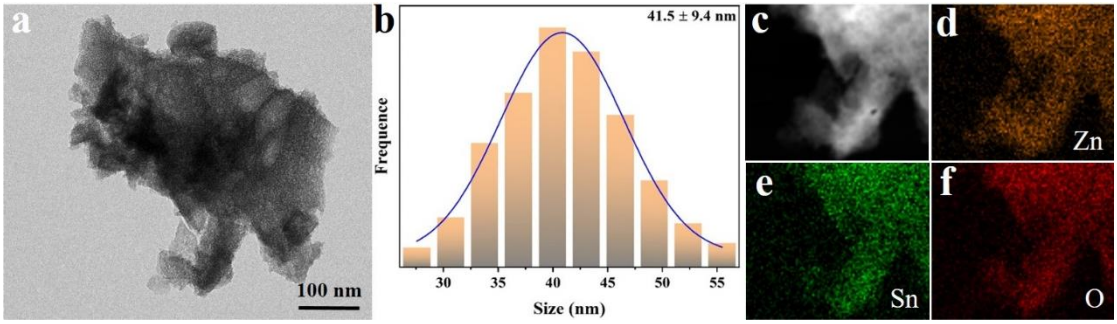

Fig. 5.5 (a) TEM image and (b) size distribution of H3, (c) high-angle annular dark-field scanning transmission electron microscope image, and (d-f) corresponding elemental mappings of H3.

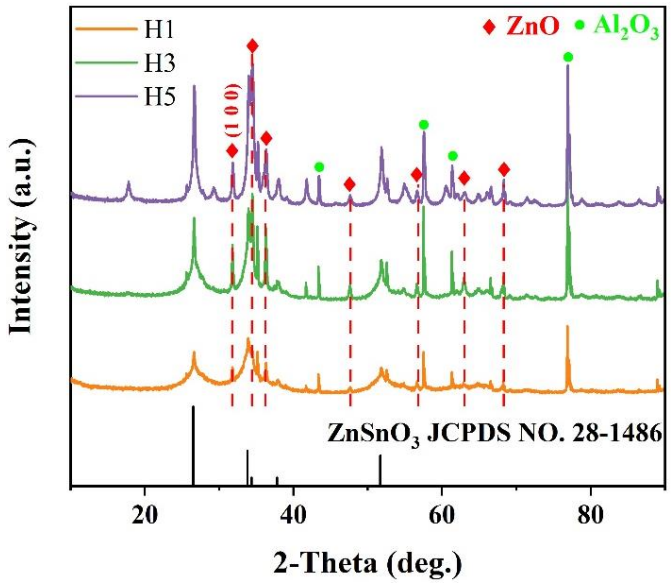

Fig. 5.6 (a) XRD patterns of H1, H3, and H5-based gas-sensing coatings, local enlargement of (a) in XRD.

Tab. 5.3 Average crystallite sizes of H1, H3, and H5-based gas-sensing coatings.

Sample	H1	H3	H5
Size/nm	7.53	10.36	14.43

XRD analysis of H1, H3, and H5 (Fig. 5.6) reveals characteristic peaks matching well with the standard card of $ZnSnO_3$ (JCPDS No. 28-1486), with distinct peaks centered at 26.50°, 33.79°, and 51.59° corresponding to the (0 1 2), (1 1 0), and (1 1 8) crystal planes, respectively [13]. These positions of the diffraction peaks remain consistent across all samples. Besides, several characteristic peaks at 2θ values of 31.76º, 34.42º, 36.25º, 47.53º, 56.60º, 62.86°, and 67.96°correspond to the (1 0 0), (0 0 2), (1 0 1), (1 0 2), (1 1 0), (1 0 3), and (1 1 2) planes, respectively, of hexagonal wurtzite structured ZnO (JCPDS No. 36-1451) [22]. This confirms that all samples consist of a mixture of ZnO and $ZnSnO_3$ phases, indicating the formation of heterojunctions during the one-step deposition process. In addition, as shown in Tab. 5.3, the average crystallite sizes of H1, H3, and H5 are determined to be 7.53, 10.36, and 14.43, respectively. This increase in crystallite size is attributed to the elevated hydrogen flow during the spraying process, affecting the recrystallization process of metal ions and leading to a deceleration in the migration of grain boundaries, resulting in larger crystallite sizes.

The high-resolution TEM image displayed in Fig. 5.7a illustrates an interplanar spacing of 0.281 nm, associated with the (1 0 0) crystal plane of ZnO. This further confirms the formation of heterojunctions at the interfaces between ZnO and $ZnSnO_3$, likely due to the different volatilization rates of Zn and Sn atoms during spraying. SPPS has been proven to be a novel route for constructing heterostructures, particularly in ternary metal oxides. Additionally, circular dot arrays observed in the selected-area electron diffraction (SAED) pattern given in Fig. 5.7b demonstrate the polycrystalline nature of the gas-sensing coating deposited by SPPS, with the lattice distance on the diffraction ring corresponding to the XRD pattern. Most importantly, with increasing hydrogen flow, the intensity of the diffraction peak becomes stronger, indicating greater crystallization in H5.

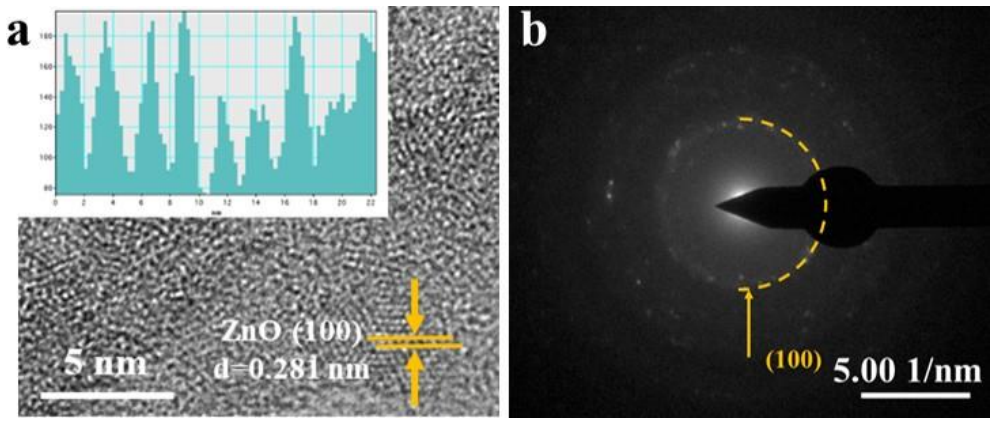

Fig. 5.7 (a) HRTEM image and (b) selected-area electron diffraction pattern of the H3-based gas-sensing coating.

To confirm the phenomenon concerning the formation of oxygen vacancies in the sample, Raman spectroscopy was utilized to inspect the occurrence of local structural changes in the samples and examine the oxygen vacancy caused by the loss of symmetry and reorientation. The Raman spectra provided in Fig. 5.8 illustrate four vibrational modes as E_2 (H), E_1 (L), A_{1g}, and B_{1g} at 439, 533, 635, and 669 cm^{-1}, respectively. More specifically, the E_2 (H) modes are characteristic of the hexagonal wurtzite crystal phase of ZnO nanostructures, associated with oxygen motion and sensitive to internal stress. The broad peaks at 635 and 669 cm^{-1} correspond to the characteristic Raman shift of $ZnSnO_3$, attributed to stretching vibrations of short Zn-O-Zn bonds [23, 24]. Notably, compared with H1, the peaks of H3 and H5 shift towards higher wavenumbers (Fig. 5.8b), suggesting an elevated relative concentration of oxygen vacancies [25]. These results consistently demonstrate that numerous oxygen vacancies are generated in the samples as the hydrogen flow changes.

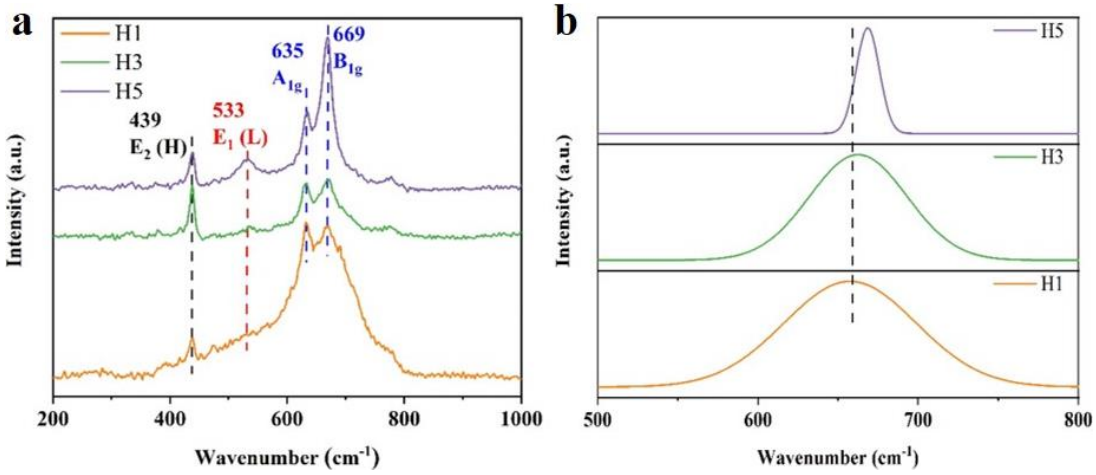

Fig. 5.8 (a) Raman spectra of H1, H3, and H5-based gas-sensing coatings, (b) local enlargement of the peak corresponding to B_{1g}.

To inspect the chemical states of different elements and the influence of cation substitution on oxygen adsorption in the three samples, XPS spectra were analyzed to reveal the core peaks of Zn 2p, Sn 3d, and O 1s. The survey spectra provided in Fig. 5.9a confirm the presence of Zn, Sn, and O, consistent with the EDS mapping shown in Figs. 5.5d-5.5f. Meanwhile, it can be observed from Fig. 5.9b that there are two characteristic peaks centered at 1044.8 and 1021.7 eV, corresponding to Zn $2p_{1/2}$ and Zn $2p_{3/2}$, respectively. The spin-orbit splitting of the two peaks is 23.1 eV, indicating a valence state of +2 for Zn ions [26]. Similarly, the Sn 3d spectra depicted in Fig. 5.9c show a split value of 8.4 eV between Sn $3d_{3/2}$ and Sn $3d_{5/2}$, demonstrating an oxidation state of +4 for Sn atoms [27]. Besides, the O 1s spectra depicted in Fig. 5.9d are split into peaks located at 529.6, 531.5, and 532.3 eV, which are assigned to lattice oxygen (O_L), chemisorbed oxygen (O_C), and oxygen vacancy (O_V), respectively [28].

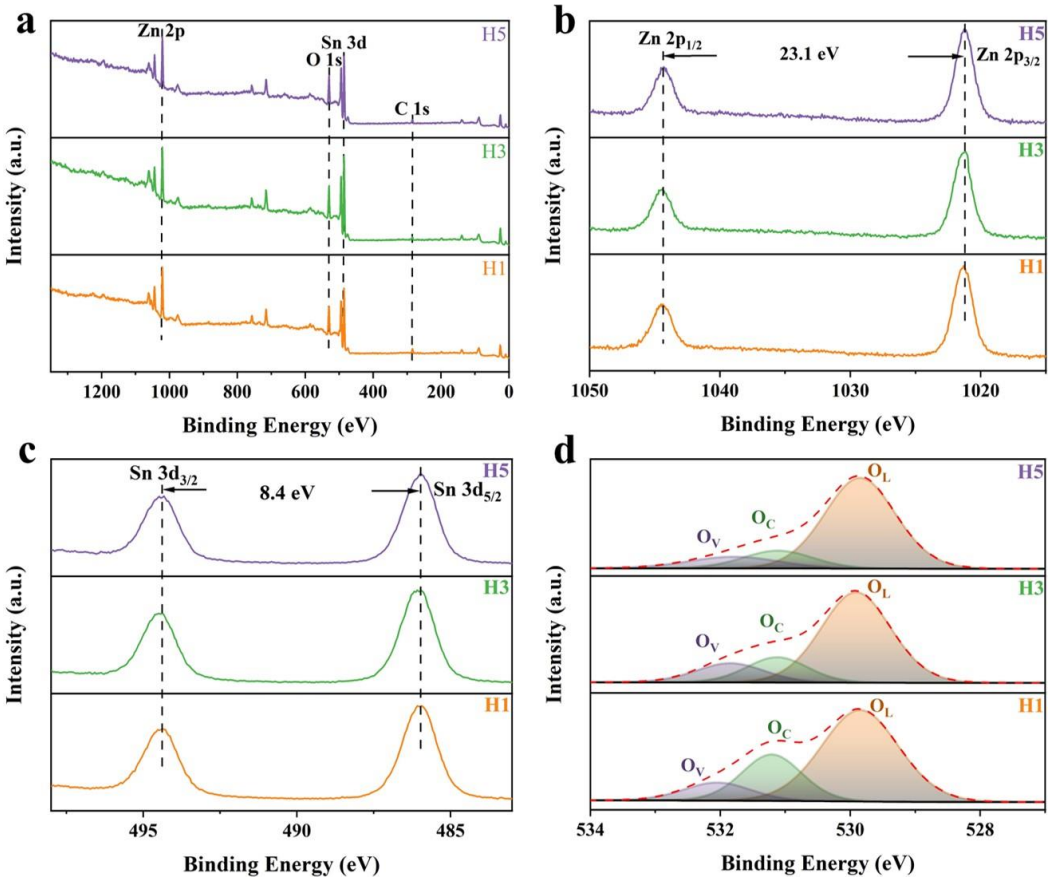

Fig. 5.9 High-resolution XPS analysis of the (a) survey spectra, (b) Zn 2p spectra, (c) Sn 3d spectra, and (d) O 1s spectra for H1, H3, and H5.

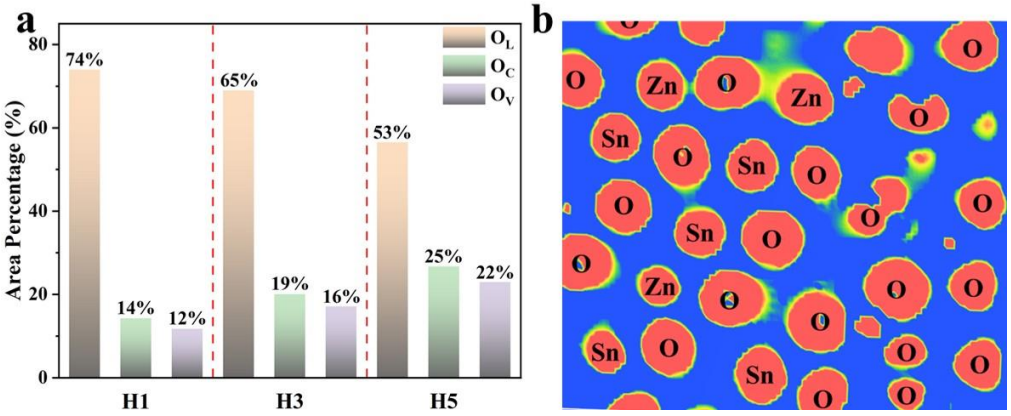

Fig. 5.10 (a) Results of the curve fitting of the O 1s spectra of the three samples, and (b) charge distributions of ZnO/$ZnSnO_3$ heterojunctions in a two-dimensional plane.

The quantification of the O 1s spectra in Fig. 5.10a reveals significant differences in the proportions of O_C and O_V components among the three samples. Specifically, the area percentages of O_C and O_V in H5 are higher than those in H1 and H3, likely due to the higher energy density of the plasma jet supported by a higher hydrogen flow. These oxygen species are crucial for the interaction of sensing materials with the target gas [29]. Moreover, the two-dimensional plane's charge density distribution analysis (Fig.

5.10b) was conducted to disclose the electronic configuration of $ZnO/ZnSnO_3$ heterojunctions [30]. This analysis indicates that the 1s orbitals from oxygen (O), 2p orbits from zinc (Zn), and 3d orbits from tin (Sn) significantly contribute to the valence and conduction bands, highlighting the heterojunctions' role in the gas-sensing mechanism.

The UV-Vis spectra displayed in Fig. 5.11a provide insights into the bandgap of $ZnO/ZnSnO_3$ heterojunctions and their potential for sensor operation at low temperatures. The absorption tails observed in the visible and near-infrared regions are associated with oxygen vacancy-induced polarons and free electrons [31]. The bandgap energy (E_g) of H1, H3, and H5, calculated using the Tauc formula by estimating the intercept of the tangent to the X axis, is determined to be 3.11, 2.99, and 2.95 eV, respectively, as shown in Fig. 5.11b. These results indicate that all samples belong to wide bandgap semiconductors, facilitating the construction of gas-sensing devices with enhanced response and selectivity at low working temperatures.

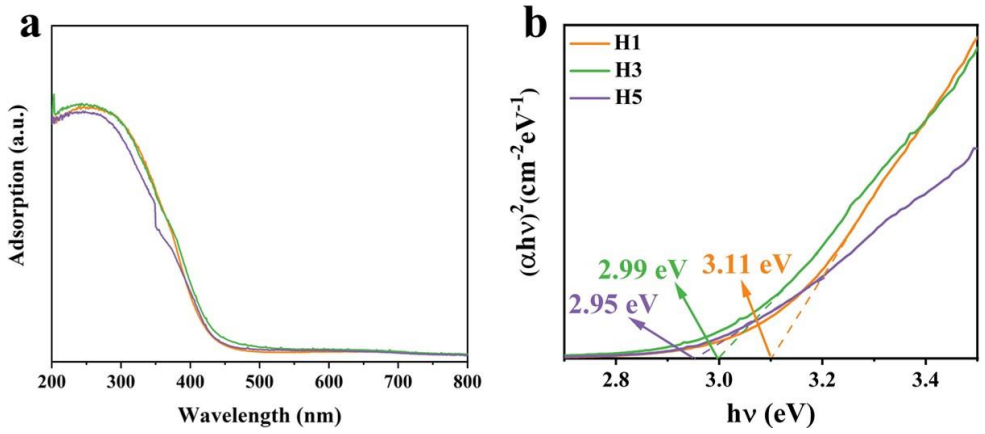

Fig. 5.11 (a) The UV-Vis spectra and (b) the corresponding Tauc curves of H1, H3, and H5-based gas sensing coatings.

The nitrogen adsorption-desorption isotherms and the pore size distributions shown in Fig. 5.12 reveal the dual-mesoporous structure of the materials (H1 and H3). In particular, apart from a uniform distribution of the main mesoporous at 3.9 nm, H1 has a secondary pore centered at 2.9 nm. This unique dual-mesoporous structure in metal oxides is advantageous for the subsequent gas-sensing process, providing abundant active sites and shorter diffusion distances for gas molecules. Tab. 5.4 summarizes the textural properties of all samples. As the hydrogen flow increases, the size distribution of the secondary pore decreases, indicating the significant impact of hydrogen flow on tuning the mesoporous structure of $ZnSnO_3$ during the deposition process.

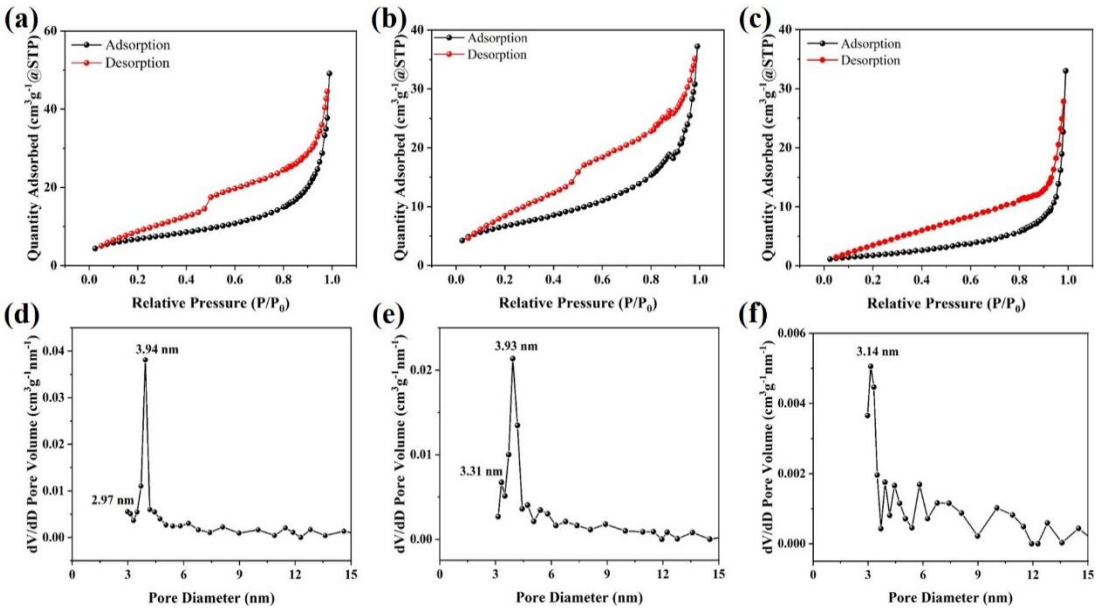

Fig. 5.12 Nitrogen adsorption-desorption isotherms and corresponding pore size distribution curves of (a, d) H1, (b, e) H3, and (c, f) H5.

Tab. 5. 4 Textural properties of the samples.

Sample	BET surface area/$m^2 \cdot g^{-1}$	Pore diameter/nm	Pore volume/$cm^3 \cdot g^{-1}$
H1	24.5	2.9, 3.9	0.07
H3	24.1	3.3, 3.9	0.06
H5	7.1	3.1	0.05

5.3.2 Gas-sensing performance investigation

To investigate the gas-sensing properties, the precursors were directly deposited onto the surface of ceramic plates with Pt electrodes to fabricate miniature side-heated semiconductor gas sensors. 2-Undecanone, as a reducing gas, is adsorbed on the gas-sensing materials, and further oxidized by the pre-adsorbed oxygen species with the electrons flowing from 2-undecanone to ZnO/$ZnSnO_3$ nanoscale heterojunctions. As mentioned above, the semiconductor characteristics and gas-sensing ability of heterojunctions can be achieved at low working temperatures under the influence of oxygen vacancies. Accordingly, the electrical and chemiresistive gas-sensing performance of the three samples were investigated at an ambient condition including the temperature of 25 ± 5 ℃ and the relative humidity (RH) of 30 ± 10%. The changes in resistance of all sensors towards 2-undecanone with different concentrations are depicted in Fig. 5.13. Initially, the resistance sharply increases when exposed to the purified air (79%N_2+21%O_2), reaching a high baseline resistance (R_a) ranging from 1 to 10 GΩ. Upon exposure to the target gas (2-undecanone), the resistance decreases, indicating the gas-sensing response of the sensors. When purified air is reintroduced,

the resistance returns to R_a, demonstrating the repeatability of the gas-sensing process.

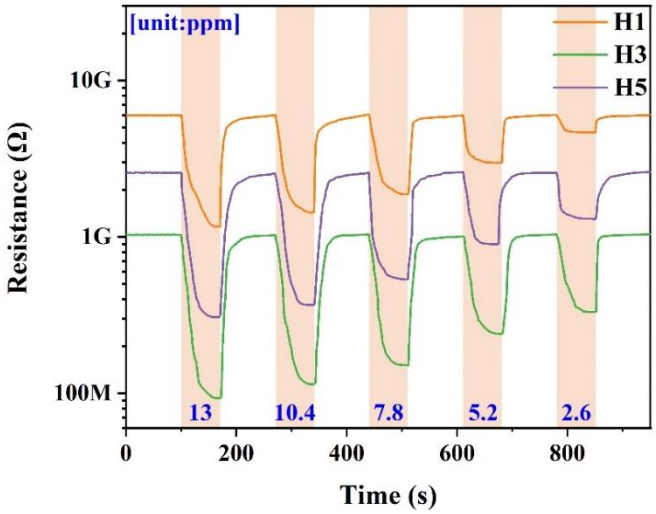

Fig. 5.13 Changes in the electrical resistance of H1, H3, and H5-based gas sensors towards 2-undecanone with concentrations ranging from 2.6 to 13 ppm.

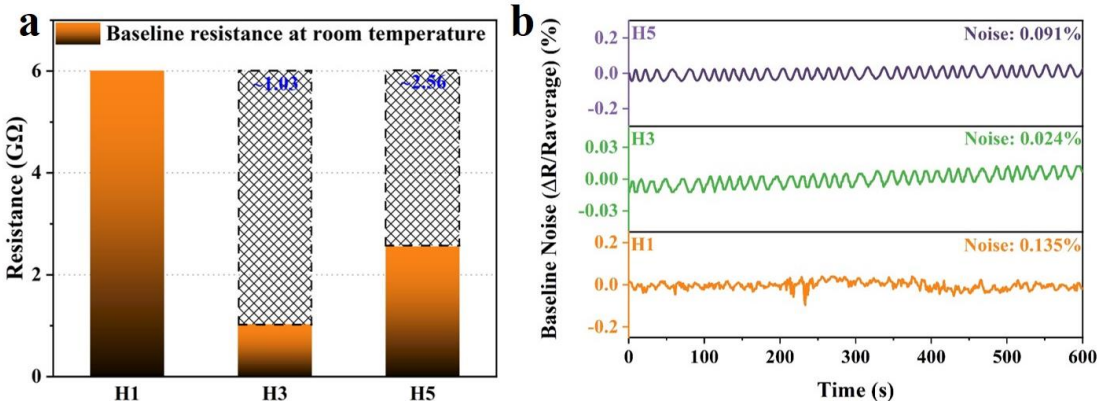

Fig. 5.14 (a) Baseline resistance and (b) electrical noise of H1, H3, and H5-based gas sensors towards the purified air.

In Fig, 5.14a, the baseline resistance (R_a) values of H1, H3, and H5-based gas sensors operating at room temperature are 6.01, 1.03, and 2.56 GΩ, respectively. The incorporation of a large number of oxygen vacancies contributes to a decrease in R_a followed by an increase when the hydrogen flow is set at 5 L/min. This behavior can be associated with the effects of oxygen vacancies, where the electrons trapped in the donor level can be directly excited into the conduction band of the semiconductor, increasing the carrier concentration and ultimately displaying a lower resistance (R_a) [32, 33]. Moreover, an increase in R_a of H5 may be due to a decrease in its film thickness (Fig. 5.3), which can decrease the grain size of the semiconductor, leading to an increase in the grain boundary [34, 35]. Additionally, the electrical noise of all sensors is initially determined by measuring the average resistance fluctuation during the introduction of

purified air. As provided in Fig. 5.14b, the calculated noise levels are approximately 0.135%, 0.024%, and 0.091% for H1, H3, and H5, respectively, with H3 exhibiting the lowest noise level. The low noise level may originate from the measuring range of the instrument utilized in this study [36].

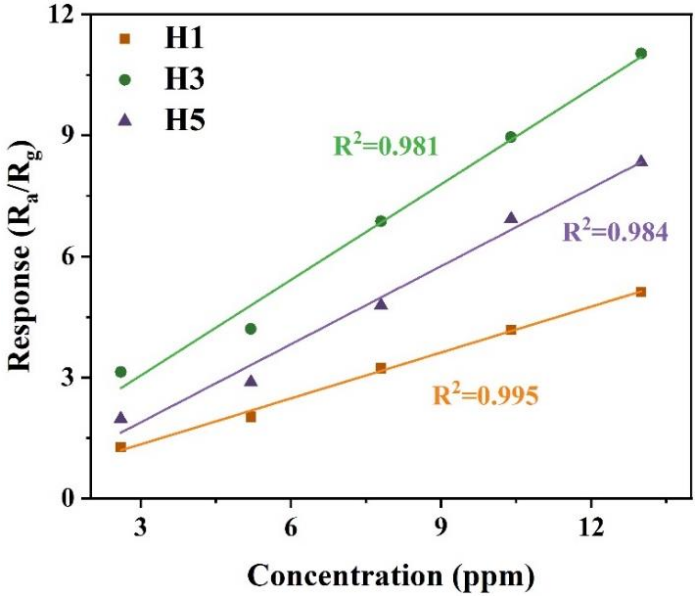

Fig. 5.15 Responses of H1, H3, and H5-based gas sensors versus gradient 2-undecanone concentrations.

Based on the variations in resistance shown in Fig, 5.13, the linear correlation between sensor response and gas concentration is revealed in Fig. 5.15. The response of all sensors elevates with an increase in gas concentration, showing a positive linear relationship. The slops (in 1/ppm) related to the response for H1, H3, and H5 are 0.38 (y=0.38x+0.21), 0.79 (y=0.79x+0.68), and 0.65 (y=0.65x-0.05), respectively, with corresponding linear fitting constants (R^2) of 0.995, 0.981, and 0.984. Among them, H3 displays the highest response of 11.03 towards 13 ppm 2-undecanone with a theoretical limit of detection (430 ppb) obtained via the equations provided in the reference [37]. The improvement in response is almost consistent with the order of the proportions of O_C and O_V measured by XPS, thus contributing to the enhanced response. Nevertheless, compared with H3, H5 displays a denser structure (Fig. 5.4), which does not provide plenty of pathways for the permeability of gas molecules, thereby decreasing the response. Consequently, apart from incorporating a large number of O_V, designing the heterojunction with a dual-mesoporous structure is considered to be the most effective strategy for improving the response of metal oxide-based gas sensors.

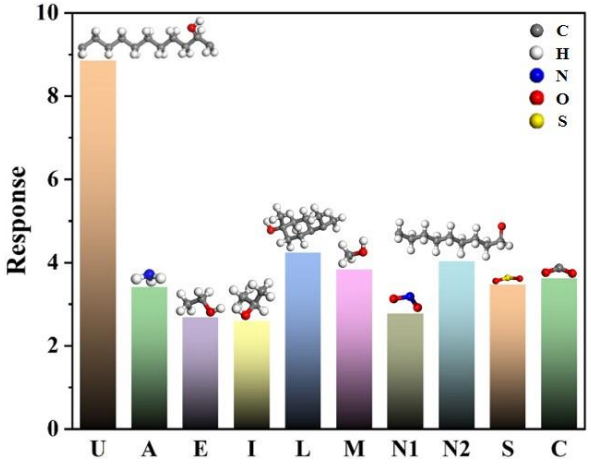

Fig. 5.16 Responses of the H3-based gas-sensing coating towards different kinds of interfering gases (U: 2-undecanone, A: ammonia, E: ethanol, I: isopropanol, L: linalool, M: methanol, N1: NO_2, N2: nonanal, S: SO_2 (100 ppm), C: CO_2 (400 ppm), all gas concentration are at 10 ppm excluding notation).

Selectivity, a crucial parameter for evaluating the performance of gas sensors, is pivotal for practical applications. It is influenced by the adsorption capacity and the reaction rate of the sensor, and intrinsic characteristics (i.e., oxidation/reduction, electronic structure, etc.) of gas molecules. Herein, nine varieties of gases including ammonia, ethanol, isopropanol, linalool, methanol, nonanal, NO_2, SO_2, and CO_2 are selected as interfering gases. In Fig. 5.16, the response of the H3-based gas sensor towards 2-undecanone is at least twice as high as that of other interfering gases. The superior selectivity can be attributed to the higher adsorption capacity and stronger reducibility of the target gas molecules on the surface of H3, facilitating faster reaction and electron transfer at room temperature compared to other interfering gases.

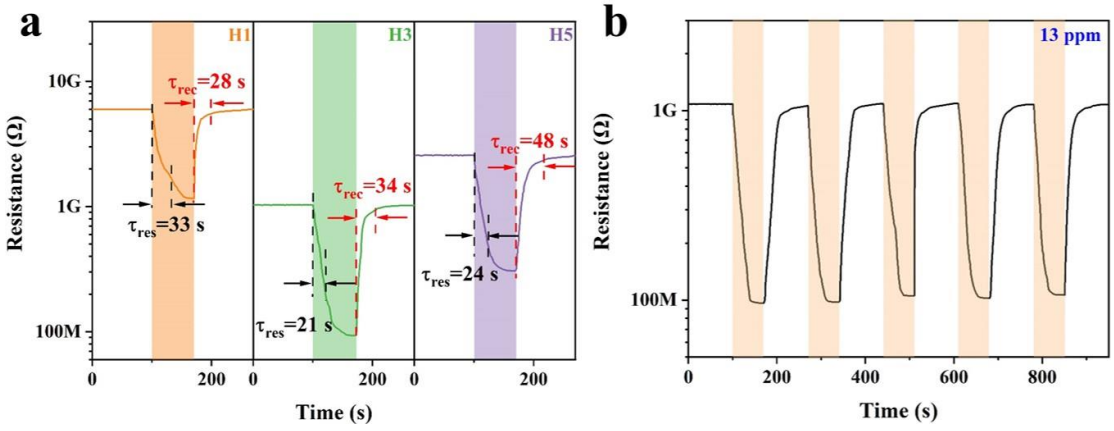

Fig. 5.17 (a) Response-recovery curves of H1, H3, and H5-based gas sensors towards 13 ppm 2-undecaone, and (b) repeated response-recovery curves of H3-based gas sensor towards 13 ppm 2-undecaone.

The response time (τ_{res}) and recovery time (τ_{rec}) of all sensors towards 13 ppm 2-undecanone at room temperature are also calculated, which is 33/28 s for H1, 21/34 s for H3, and 24/48 s for H5, respectively. These results indicate a rapid response/recovery speed of the gas sensors, as shown in Fig. 5.17a, owing to their nanoscale porous structures. Moreover, to verify the repeatability of the sensor, the response-recovery curve of H3 towards 13 ppm 2-undecanone within five cycles depicted in Fig. 5.17b is analyzed, and there are no huge degradations in both response and R_a, with a deviation of 10.7% and 2.8%, respectively, confirming an excellent repeatability in the analysis of the target gas at room temperature.

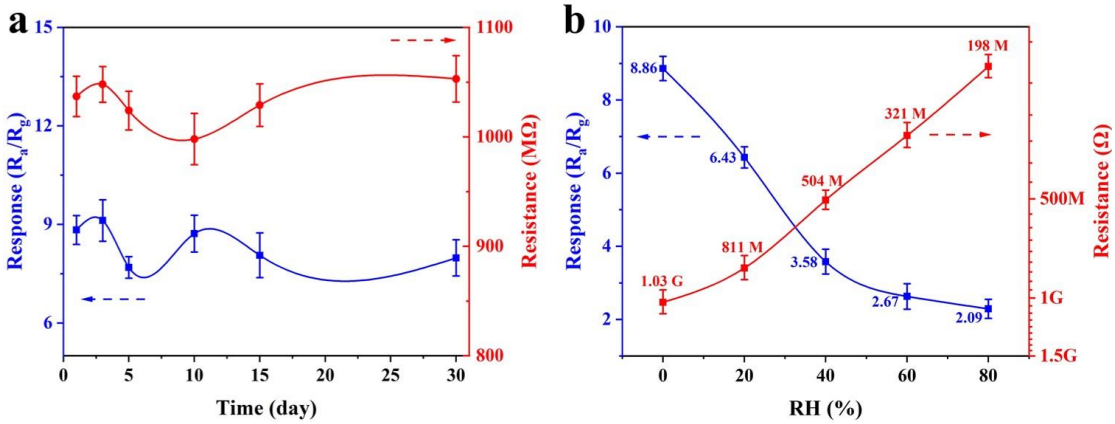

Fig. 5.18 (a) Long-term stability and (b) sensor responses and its corresponding baseline resistance of the H3-based gas sensor towards 10 ppm 2-undecanone under various relative humidity conditions.

The long-term stability investigations presented in Fig. 5.18a reveal that the H3-based gas sensor nearly retains its response over the 30-day testing period, experiencing only a minor decrease of around 9%. This indicates outstanding long-term stability, laying a strong foundation for practical applications and commercial promotion. Furthermore, the effects of humidity cannot be ignored with regard to the sensor's practical utilization. Hence, the response and R_a of the H3-based gas sensor towards 10 ppm 2-undecanone are measured under different RH conditions (20%, 40%, 60%, and 80%). It can be seen from Fig. 5.18b that the response and R_a decrease by 147% and 20%, respectively, with increasing RH from 0% to 40%. This decrease is attributed to the increased humidity, leading to the formation of inactive hydroxyl groups through the reaction between water molecules and adsorbed oxygen, hindering the sensing process between the target gas and adsorbed oxygen species [38, 39]. Moreover, the insolubility of 2-undecanone in water contributes to the reduction in response. Despite the decrease in response with increasing humidity, the sensor maintains substantial response (R_a/R_g=2.09) for 10 ppm 2-undecanone even in a highly humid atmosphere (80%RH). These findings indicate that the ZnO/$ZnSnO_3$ nanoscale heterojunction-

based gas sensor directly manufactured by SPPS is suitable for detecting ppm-level 2-undecanone under varying humidity conditions. In the future, further efforts, such as depositing a functional sensing layer onto the surface of the heterojunctions, chemically modulating the sensing materials, and constructing appropriate humidity compensation algorithms, should be taken to dramatically eliminate the negative influence of humidity on improving metal oxide-based gas sensors.

5.3.3 Gas-sensing mechanism

From the above gas-sensing performance investigations, ZnO/$ZnSnO_3$ n-n nanoscale heterojunctions exhibit excellent gas-sensing properties, represented by a high response, a rapid response time, and a low theoretical detection limit, towards 2-undecanone at room temperature. Currently, it is universally acknowledged that the gas-sensing mechanism of metal oxide semiconductors strongly involves three steps, namely absorption, interaction, and desorption [40, 41]. To further explore the gas-sensing mechanism of ZnO/$ZnSnO_3$ heterojunctions, the energy level structures of pure $ZnSnO_3$ and ZnO are calculated based on DFT calculations, as reflected in Figs. 5.19a and 5.19b. For the ZnO/$ZnSnO_3$ composites, due to different work functions and bandgaps of $ZnSnO_3$ and ZnO, the electrons can transfer from ZnO to $ZnSnO_3$, contributing to the shifting of the Fermi level towards a more negative potential until the two Femi levels (E_f) reach equilibrium. When purified air is introduced, oxygen captures free electrons from the conduction band, forming chemically adsorbed oxygen species (i.e., O_2^-, O^-, O^{2-}) based on the working temperature of the sensor [42]. In this work, the gas-sensing performance investigations are performed at room temperature, and O_2^- is the dominant absorption oxygen. Simultaneously, additional electron depletion and accumulation layers separately form on the surface of ZnO and $ZnSnO_3$, decreasing the number of grain boundary barriers. This process enhances the interaction between gas molecules and sensing materials, ultimately contributing to the room-temperature gas-sensing properties of ZnO/$ZnSnO_3$ heterojunctions. These interactions cannot be investigated under experimental conditions because of the limited conditions. However, they have been proposed by a few references [27, 31, 43-45]. Specifically, when the reducing gas (2-undecanone) is exposed, it is first transformed into the adsorbed gas molecules. Then the interaction between $C_{11}H_{22}O$ (ad) and O_2^- is undergone, generating $C_{11}H_{20}O$ (ad) (the loss of H), H_2O (g), and free electrons, as schematically illustrated in Figs. 5.19c and 5.19d. In the interaction between the target gas molecules and the sensing materials, the trapped electrons are released into the conduction band, thus decreasing the height of the potential barrier and the thickness of the depletion layer, ultimately resulting in a decrease in electrical resistance [46].

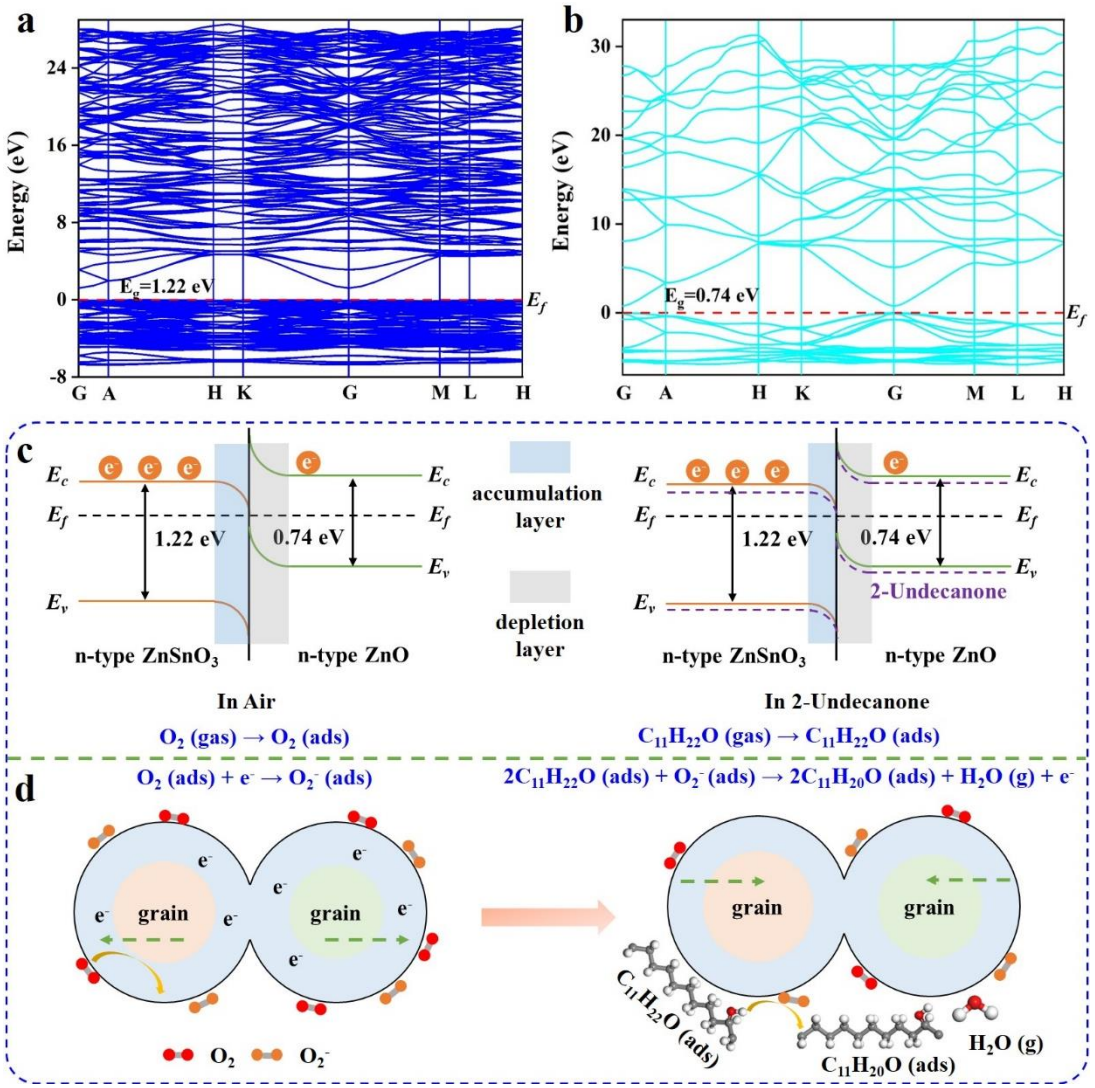

Fig. 5.19 Energy level diagrams of $ZnO/ZnSnO_3$ n-n nanoscale heterojunctions based on DFT calculation. The band structures of (a) $ZnSnO_3$ and (b) ZnO. (c, d) Schematic illustrations of the room-temperature gas-sensing mechanism of the heterojunctions towards ppm-level 2-undecanone (E_c: conduction band bottom; E_f: Fermi level; E_v: valence band top).

The enhanced gas-sensing properties of the H3-based gas sensor for room-temperature detection of 2-undecaone can be attributed to the synergic effects of its unique dual-mesoporous nanostructures with high specific surface areas and the increased relative proportions of O_C and O_V. This unique nanoporous structures provide numerous active sites and shorter diffusion distances for the absorption and desorption of the target gas, thereby elevating the gas-sensing properties, represented by the improvement of response and the reduction of response time. Nevertheless, as the hydrogen flow increases to 5 L/min, this unique dual-mesoporous structure gradually disappears, leading to a reduction in response. Moreover, the relative percentages of O_C and O_V in H3 and H5 measured by XPS are higher than that of H1. The increase in the relative proportions of O_C and O_V is beneficial to improve the adsorption capacity and

the reaction rate of 2-undecanone, then promote the electron transfer from the target gas to the surface of the sensor, thus contributing to the enhanced gas-sensing performance. Most importantly, an essential factor including the thickness and surface roughness of the deposited gas-sensing coatings cannot be ignored. Although H5 exhibits the highest relative proportions of O_C and O_V (Fig. 5.10a) and the narrowest bandgap (Fig. 5.11), its decreased thickness and surface uniformity (Fig. 5.3) may increase the contact resistance (Fig. 5.14a) and reduce the specific surface areas, thereby providing a limited number of active sites and pathways for the absorption and diffusion of the target gas. Accordingly, apart from precisely incorporating highly concentrated O_V and rationally designing mesoporous structures, the other above-stated aspects including the regulation of the thickness and the modulation of surface uniformity of ZnO/$ZnSnO_3$ n-n nanoscale heterojunction-based gas sensors also assist in enhancing the gas-sensing performance in the analysis of 2-undecanone at room temperature

5.3.4 Practical application of ZnO/$ZnSnO_3$-based gas sensors

To evaluate the potential application of the fabricated gas sensor in inspecting rice quality, the resistance changes of H3 towards volatile gases produced by the two varieties of rice stored for different periods (1, 3, 5, 7, 15, and 30 days) at room temperature were monitored (Fig. 5.20a). In Fig. 5.20b, the sensor response towards volatile compounds generated from japonica rice aging is 62.9, which is approximately 4.6 times higher than that of indica rice. This suggests that the sensor can serve as a detection unit in an E-nose for distinguishing japonica rice from indica rice. Additionally, based on the variations of resistance, the corresponding sensor response and baseline resistance (R_a) are obtained. It can be seen from Fig, 5.20c that there are no significant changes in both sensor response and R_a when the storage period is less than 10 days, which may be due to the slow aging process of japonica rice. Slight fluctuations may be attributed to testing conditions such as temperature, humidity, and pressure, which can exert a significant influence on the obtained results [1, 43, 47]. Nevertheless, a slight increase in sensor response is noted for storage periods exceeding 15 days, particularly reaching 30 days, demonstrating a gradual occurrence of the aging process in japonica rice. Overall, these findings indicate that the H3-based gas sensor holds promise for application in developing a high-performance E-nose for assessing rice quality during the aging process, particularly in identifying adulteration in other rice varieties.

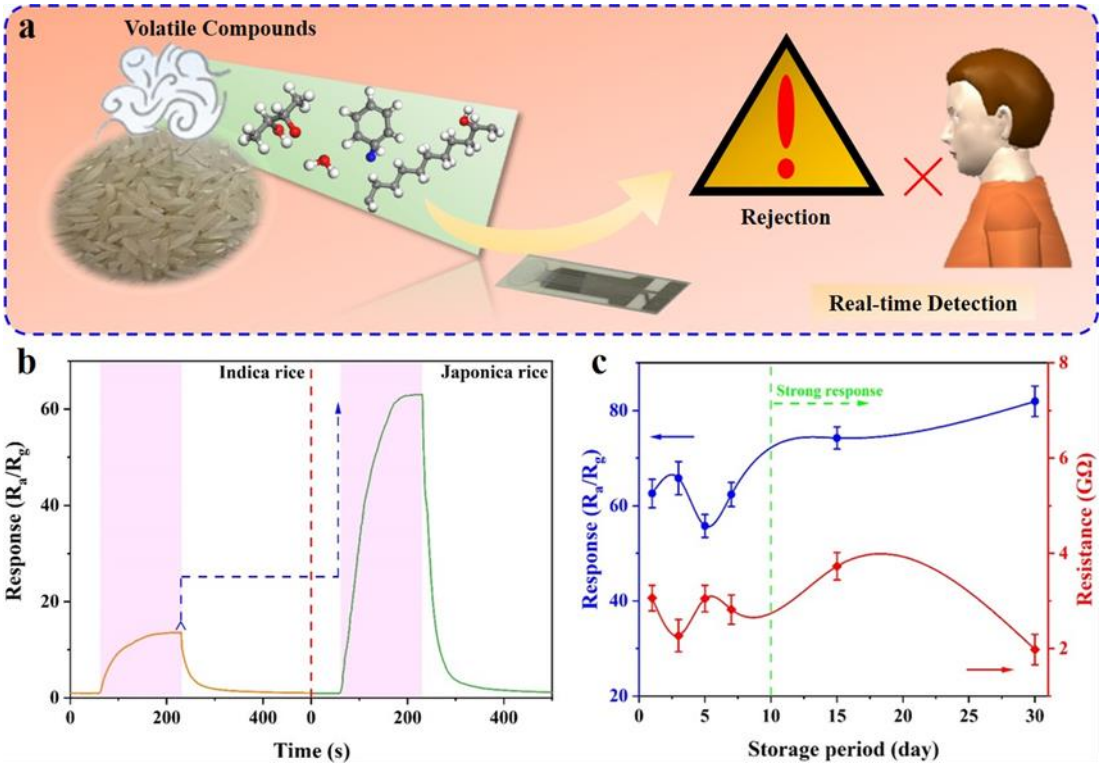

Fig. 5.20 (a) Schematic diagram of the sensor utilized in the real-time detection of volatile compounds generated from rice aging. (b) Responses measured under exposure to volatile gases generated from 30 g japonica and indica rice aging. (c) Response and baseline resistance of the sensor towards volatile compounds generated from japonica rice stored for different periods (1, 3, 5, 7, 15, and 30 days).

5.4 Conclusions

In this chapter, nanoscale ZnO/$ZnSnO_3$ heterojunctions with dual-mesoporous structures and varying concentrated oxygen vacancies are directly manufactured by solution precursor plasma spray (SPPS). By controlling the flow of hydrogen, the porous structures and oxygen vacancies in ZnO/$ZnSnO_3$-based gas-sensing materials are regulated, and they are used for room-temperature detection of ketones, characteristic biomarkers generated through the oxidation of fatty acids after rice aging. The structural characterizations and gas-sensing performance investigations are conducted to comprehensively investigate the influence of hydrogen flow on the enhanced gas-sensing mechanisms of the ZnO/$ZnSnO_3$-based gas sensor. The main conclusions drawn in this chapter are summarized as follows:

(1) Microstructural analyses of the three samples exhibit the formation of n-n heterojunctions at the interfaces between ZnO and $ZnSnO_3$ during the spraying utilizing the corresponding precursors with a molar ratio of 1:1. XRD analysis further confirms the formation of heterojunctions, with characteristic peaks becoming sharper and

stronger as the hydrogen flow increases, indicating a higher degree of crystallization.

(2) The formation process mainly involves the following steps, namely evaporation, precipitation, pyrolysis, and melting. Due to the different volatilization of Zn and Sn atoms during SPPS, heterojunctions are formed at the interfaces between ZnO and $ZnSnO_3$. It has been proven that SPPS is a novel route to construct heterostructures, especially in ternary metal oxides.

(3) The quantification of the O 1s spectra demonstrates that the area percentages of O_C and O_V in H5 are higher than that of the other two samples (H1 and H3), significantly increasing the number of active absorption sites for 2-undecanone. The gas-sensing coatings fabricated with a low hydrogen flow (H1 and H3) exhibit a dual-mesoporous structure, contributing to the improved gas-sensing performance in the analysis of VOCs.

(4) Room-temperature gas-sensing performance of all sensors towards 2-undecanone reveals that the H3-based gas sensor exhibits superior gas-sensing properties including a higher response of 11.03, a rapid response time of 21 s, and a low theoretical detection limit of 430 ppb towards 2-undecanone.

(4) The enhanced gas-sensing performance of the H3-based gas sensor can be attributed to its unique porous structures, and the elevated relative proportions of chemisorbed oxygen and oxygen vacancy components, as confirmed by SEM and XPS analysis. The mesoporous structures with a high surface-to-volume ratio provide a feasible pathway for the transmission and diffusion of the target gas. The higher relative proportion of oxygen vacancies in H3 measured by XPS contributes to increased availability of oxygen species for reaction with 2-undecanone.

(5) The practical experiments show that the response of the H3-based gas sensor towards VOCs in the aging of different varieties of rice (indica rice and japonica rice) at room temperature are significantly different, so the developed gas sensor can be used to distinguish japonica rice from indica rice. Meanwhile, with an increase in the storage period, the sensor response and baseline resistance (R_a) show only minor fluctuations, without significant attenuation. Accordingly, the regulation of porous structures and the concentration of oxygen vacancies in $ZnO/ZnSnO_3$ is an effective strategy for enhancing the room-temperature gas-sensing performance of MOS-based gas sensors. Collectively, this work holds promise for the development of a high-performance E-nose for evaluating rice quality during storage.

References

[1] J.Y. Xu, K.W. Liu, C. Zhang. Electronic nose for volatile organic compounds analysis in rice aging. Trends in Food Science & Technology, 109 (2021) 83-93. https://doi.org/10.1016/j.tifs.2021.01.027.

[2] Q. Wei, C. Ma, Y.J. Xu, T.L. Wang, Y.Y. Chen, J. Lü, L.L. Zhang, C.Z. Jiang, B. Hong, J.P. Gao. Control of chrysanthemum flowering through integration with an aging pathway. Nature Communications, 8 (2017) 829. https://doi.org/10.1038/s41467-017-00812-0.

[3] L.G. Dias, A. Hacke, S.F. Bergara, O.V. Villela, L.R.B. Mariutti, N. Bragagnolo. Identification of volatiles and odor-active compounds of aromatic rice by OSME analysis and SPME/GC-MS. Food Research International, 142 (2021) 110206. https://doi.org/10.1016/j.foodres.2021.110206.

[4] H.Y. Yu, T. Xie, J.R. Xie, L.Z. Ai, H.X. Tian. Characterization of key aroma compounds in Chinese rice wine using gas chromatography-mass spectrometry and gas chromatography-olfactometry. Food Chemistry, 293 (2019) 8-14. https://doi.org/10.1016/j.foodchem.2019.03.071.

[5] C.H. Lee, Y.Y. Lee, Y.C. Chang, W.L. Pon, S.P. Lee, N. Wali, T. Nakazawa, Y. Honda, J.J. Shie, Y.P. Hsueh. A carnivorous mushroom paralyzes and kills nematodes via a volatile ketone. Science Advances, 9 (2023) eade480. https://doi.org/10.1126/sciadv.ade4809.

[6] W.C. Kang, H. Lin, R.Q. Jiang, Y.Q. Yan, W. Ahmad, Q. Ouyang, Q.S. Chen. Emerging applications of nano-optical sensors combined with near-infrared spectroscopy for detecting tea extract fermentation aroma under ultrasound-assisted sonication. Ultrasonics Sonochemistry, 88 (2022) 106095. https://doi.org/10.1016/j.ultsonch.2022.106095.

[7] D.H. Kim, S. Chong, C. Park, J. Ahn, J.S. Jang, J. Kim, I.D. Kim. Oxide/ZIF-8 hybrid nanofiber yarns: Heightened surface activity for exceptional chemiresistive sensing. Advanced Materials, 34 (2022) 2105869. https://doi.org/10.1002/adma.202105869.

[8] S.Y. Jeong, Y.K. Moon, J. Wang, J.H. Lee. Exclusive detection of volatile aromatic hydrocarbons using bilayer oxide chemiresistors with catalytic overlayers. Nature Communications, 14 (2023) 233. https://doi.org/10.1038/s41467-023-35916-3.

[9] S. Ma, L.Y. Shen, S.H. Ma, J. Wen, J.Y. Xu. Emerging zinc stannate and its application in volatile organic compounds sensing. Coordination Chemistry Reviews, 490 (2023) 215217. https://doi.org/10.1016/j.ccr.2023.215217.

[10] H.T. Cao, Z.X. Hu, X.Y. Wei. H.R. Wang, X. Tian, S.J. Ding. Conductometric ethanol gas sensor based on a bilayer film consisting of SnO_2 film and

$SnO_2/ZnSnO_3$ porous film prepared by magnetron sputtering. Sensors and Actuators B: Chemical, 382 (2023) 133562. https://doi.org/10.1016/j.snb.2023.133562.

[11] J.H. Ma, Y.Y. Li, J.C. Li, X.Y. Yang, Y. Ren, A.A. Alghamdi, G.X. Song, K.P. Yuan, Y.H. Deng. Rationally designed dual-mesoporous transition metal oxides/noble metal nanocomposites for fabrication of gas sensors in real-time detection of 3-hydroxy-2-butanone biomarker. Advanced Functional Material, 32 (2022)2107439.

[12] X.Y. Wang, H. Li, X.T. Zhu, M.Z. Xia, T. Tao, B.X. Leng, W. Xu. Improving ethanol sensitivity of $ZnSnO_3$ sensor at low temperature with multi-measures: Mg doping, nano-TiO_2 decoration and UV radiation. Sensors and Actuators B: Chemical, 297 (2019) 126745. https://doi.org/10.1016/j.snb.2019.126745.

[13] Z.Y. Wang, J.Y. Miao, H.X. Zhang, D. Wang, J.B. Sun. Hollow cubic $ZnSnO_3$ with abundant oxygen vacancies for H_2S gas sensing. Journal of Hazardous Materials, 391 (2020) 122226. https://doi.org/10.1016/j.jhazmat.2020.122226.

[14] C. Zhang, G.F. Liu, K.W. Liu, K.D.Wu. ZnO_{1-x} coatings deposited by atmospheric plasma spraying for room temperature ppb-level NO_2 detection. Applied Surface Science, 528 (2020) 147041. https://doi.org/10.1016/j.apsusc.2020.147041.

[15] Z.X. Yu, H. Moussa, Y.Z. Ma, M.M. Liu, B. Chouchene, R. Schneider, M. Moliere, H.L. Liao. Oxygen-defective ZnO films with various nanostructures prepared via a rapid one-step process and corresponding photocatalytic degradation applications. Journal of Colloid and Interface Science, 534 (2019) 637-648. https://doi.org/10.1016/j.jcis.2018.09.067.

[16] H.Y. Yu, W.X. Wang, M.C. Liu, T.C. Zhao, R.F. Lin, M.M. Hou, Y.F. Kou, L. Chen, A.A. Elzatahry, F. Zhang, D.Y. Zhao, X.M. Li. Versatile synthesis of dendritic mesoporous rare earth-based nanoparticles. Science Advances, 8 (2022) eabq2356. https://doi.org/10.1126/sciadv.abq2356.

[17] K.Y. Chen, W.H. Xie, Y. Deng, J.T. Han, Y.H. Zhu, J.G. Sun, K.P. Yuan, L.M. Wu, Y.H. Deng. Alkaloid precipitant reaction inspired controllable synthesis of mesoporous tungsten oxide spheres for biomarker sensing. ACS Nano, 17 (2023) 15763-15775. https://doi.org/10.1021/acsnano.3c03549.

[18] B. Jiang, H.R. Xue, P. Wang, H.R. Du, Y.Q. Kang, J.J. Zhao, S.Y. Wang, W. Zhou, Z.F. Bian, H.X. Li, J. Henzie. Yamauchi, Y. Noble-metal-metalloid alloy architectures: Mesoporous amorphous iridium-tellurium alloy for electrochemical N_2 reduction. Journal of the American Chemical Society, 145 (2023) 6079-6086. https://doi.org/10.1021/jacs.2c10637.

[19] R. Kim, J.S. Jang, D.H. Kim, J.Y. Kang, H.J. Cho, Y.J. Jeong, I.D. Kim. A general synthesis of crumpled metal oxide nanosheets as superior chemiresistive sensing layers. Advanced Functional Materials, 29 (2019) 1903128. https://doi.org/10.1002/adfm.201903128.

[20] J. Ying, S. Lenaerts, M.D. Symes, X.Y. Yang. Hierarchical design in nanoporous metals. Advanced Science, 9 (2022) 2106117. https://doi.org/10.1002/advs.202106117.

[21] C.H. Huang, X.L. Shang, X.Y. Zhou, Z. Zhang, X. Huang, Y. Lu, M.C. Wang, M. Loffler, Z.Q. Liao, H.Y. Qi, U. Kaiser, D. Schwarz, A. Fery, T. Wang, S.C.B. Mannsfeld, G.Q. Hu, X.L. Feng, R.H. Dong. Hierarchical conductive metal-organic framework films enabling efficient interfacial mass transfer. Nature Communications, 14 (2023) 3850. https://doi.org/10.1038/s41467-023-39630-y.

[22] H.J. Han, G.R. Lee, Y.J. Xie, H. Jang, D.J. Hynek, E.N. Cho, Y.J. Kim, Y.S. Jung, J.J. Cha. Unconventional grain growth suppression in oxygen-rich metal oxide nanoribbons. Science Advances, 7 (2021) eabh2012. https://doi.org/10.1126/sciadv.abh2012.

[23] F.X. Ling, L.F. Wang, F.F. Liu, M.Z. Ma, S.P. Zhang, X.H. Rui, Y. Shao, Y.X. Yang, S.N. He, H.G. Pan, X.J. Wu, Y. Yao, Y. Yu. Multi-scale structure engineering of $ZnSnO_3$ for ultra-long-life aqueous zinc-metal batteries. Advanced Materials, 35 (2023) 2208764. https://doi.org/10.1002/adma.202208764.

[24] N. Mayedwa, N. Mongwaketsi, S. Khamlich, K. Kaviyarasu, N. Matinise, M. Maaza. Green synthesis of zin tin oxide ($ZnSnO_3$) nanoparticles using Aspalathus Linearis natural extracts: Structural, morphological, optical and electrochemistry study. Applied Surface Science, 446 (2018) 250-257. https://doi.org/10.1016/j.apsusc.2017.12.161.

[25] C.T. Altaf, N.S. Sahsuvar, N. Abdullayeva, O. Coskun, A. Kumtepe, E. Karagoz, M. Sankir, N.D. Sankir. Inverted configuration of $Cu(In,Ga)S_2/In_2S_3$ on 3D-$ZnO/ZnSnO_3$ bilayer system for highly efficient photoelectrochemical water splitting. ACS Sustainable Chemistry & Engineering, 8 (2020) 15209-15222. https://doi.org/10.1021/acssuschemeng.0c04846.

[26] R. Zhang, P.Y. Zang, D. Yang, J.H. Li, N. Hu, S.N. Qu, P.P. Yang. A phase engineering strategy of perovskite-type $ZnSnO_3$: Nd for boosting the sonodynamic therapy performance. Advanced Functional Materials, 33 (2023) 2300522. https://doi.org/10.1002/adfm.202300522.

[27] J.Y. Xu, H.L. Liao, C. Zhang. $ZnSnO_3$ based gas sensors for pyridine volatile marker detection in rice aging during storage. Food Chemistry, 408 (2023) 135204. https://doi.org/10.1016/j.foodchem.2022.135204.

[28] Y.C. Wang, J.M. Wu. Effect of controlled oxygen vacancy on H_2-production through the piezocatalysis and piezophototronics of ferroelectric R3C $ZnSnO_3$ nanowires. Advanced Functional Materials, 30 (2020) 1907619. https://doi.org/10.1002/adfm.201907619.

[29] H.H. Tsai, W.Y. Nie, J.C. Blancon, C.C.S. Toumpos, R. Asadpour, B. Harutyunyan, A.J. Neukirch, R. Verduzco, J.J. Crochet, S. Tretiak, L. Pedesseau, J. Even, M.A.

Alam, G. Gupta, J. Lou, P.M. Ajayan, M.J. Bedzyk, M.G. Kanatzidis, A.D. Mohite. High-efficiency two-dimensional Ruddlesden-Popper perovskite solar cells. Nature, 536 (2016) 312-316. https://doi.org/10.1038/nature18306.

[30] J. Wang, Y. Ren, H. Liu, Z.L. Li, X.Y. Liu, Y.H. Deng, X.S. Fang. Ultrathin 2D $NbWO_6$ perovskite semiconductor based gas sensors with ultrahigh selectivity under low working temperature. Advanced Materials, 34 (2022) 2104958. https://doi.org/10.1002/adma.202104958.

[31] J.Y. Xu, C. Zhang. Oxygen vacancy engineering on cerium oxide nanowires for room-temperature linalool detection in rice aging. Journal of Advanced Ceramics, 11 (2022) 1559-1570. https://doi.org/10.1007/s40145-022-0629-8.

[32] X.Y. Huang, K.Y. Chen, W.H. Xie, Y.Y. Li, F. Yang, Y. Deng, J.C. Li, F.L. Jiang, Y. Shu, L.M. Wu, W.F. Xie, Y.H. Deng. Chemiresistive gas sensors based on highly permeable Sn-doped bismuth subcarbonate microspheres: Facile synthesis, sensing performance, and mechanism study. Advanced Functional Materials, (2023) 2304718. https://doi.org/10.1002/adfm.202304718.

[33] P. Wang, S.S. Guo, Z.X. Hu, L.C. Zhou, T.K. Li, S.L. Pu, H. Mao, H. Cai, Z.F. Zhu, B.B. Chen, H.Y. Li, H. Liu. Single-atom Cu stabilized on ultrathin $WO_{2.72}$ nanowire for highly selective and ultrasensitive ppb-level toluene detection. Advanced Science, 10 (2023) 2302778. https://doi.org/10.1002/advs.202302778.

[34] A. Kumar, A. Sanger, A. Kumar, R. Chandra. Fast response ammonia sensors based on TiO_2 and NiO nanostructured bilayer thin films. RSC Advances, 6 (2016) 77636. https://doi.org/10.1039/c6ra14342c.

[35] X.Y. Kou, F.Q. Meng, K. Chen, T.S. Wang, P. Sun, F.M. Liu, X. Yan, Y.F. Sun, F.M. Liu, K. Shimanoe, G.Y. Lu. High-performance acetone gas sensor based on Ru-doped SnO_2 nanofibers. Sensors and Actuators B: Chemical, 320 (2020) 128292. https://doi.org/10.1016/j.snb.2020.128292.

[36] E.K. Alenezy, Y.M. Sabri, A.E. Kandjani, D. Korcoban, S.S.A.A.H. Rashid, S.J. Ippolito, S.K. Bhargava. Low-temperature hydrogen sensor: Enhanced performance enabled through photoactive Pd-decorated TiO_2 colloidal crystals. ACS Sensors, 5 (2020) 3902-3914. https://doi.org/10.1021/acssensors.0c01387.

[37] F.A.A. Nugroho, I. Darmadi, L. Cusinato, A. Susarrey-Arce, H. Schreuders, L.J. Bannenberg, A.B.D. Fanta, S. Kadkhodazadeh, J.B. Wagner, T.J. Antosiewicz, A. Hellman, V.P. Zhdanov, B. Dam, C. Langhammer. Metal-polymer hybrid nanomaterials for plasmonic ultrafast hydrogen detection. Nature Materials, 18 (2019) 489-495. https://doi.org/10.1038/s41563-019-0325-4.

[38] R.A. Potyrailo, S. Go, D. Sexton, X.X. Lie, N. Alkadi, A. Kolmakov, B. Amm, R. St-Pierre, B. Scherer, M. Nayeri, G. Wu, C. Collazo-Davil, D. Forman, C. Calvert, C. Mack, P. McConnell. Extraordinary performance of semiconducting metal oxide gas sensors using dielectric excitation. Nature Electronics, 3 (2020) 280-289.

https://doi.org/10.1038/s41928-020-0402-3.

[39] F.D. Qu, S.D. Zhang, C.Z. Huang, X.Y. Guo, Y. Zhu, T. Thomas, H.C. Guo, J.P. Attfield, M.H. Yang. Surface functionalized sensors for humidity-independent gas detection. Angewandte Chemie, 60 (2021) 6561-6566. https://doi.org/10.1002/anie.202015856.

[40] Y.Y. Li, K.Y. Chen, Y. Liu, J.H. Ma, Y.Z. Liao, H.T. Yang, J.S. Cheng, Q. Yue, K.P. Yuan, Y. Ren, Y.D. Zou, Y.H. Deng. Gadolinium-doped mesoporous tungsten oxides: Rational synthesis, gas sensing performance, and mechanism investigation. Nano Research, 16 (2023) 7527-7536. https://doi.org/10.1007/s12274-022-5274-6.

[41] C.Y. Yuan, J.H. Ma, Y.D. Zou, G.S. Li, H.L. Xu, V.V. Sysoev, X.W. Cheng, Y.H. Deng. Modeling interfacial interaction between gas molecules and semiconductor metal oxides: A new view angle on gas sensing. Advanced Science, 9 (2022) 2203594. https://doi.org/10.1002/advs.202203594.

[42] J.H. Ma, Y.Y. Li, J.C. Li, X.Y. Yang, Y. Ren, A.A. Alghamdi, G.X. Song, K.P. Yuan, Y.H. Deng. Rationally designed dual-mesoporous transition metal oxides/noble metal nanocomposites for fabrication of gas sensors in real-time detection of 3-hydroxy-2-butanone biomarker. Advanced Functional Materials, 32 (2022) 2107439. https://doi.org/10.1002/adfm.202107439.

[43] C. Zhang, J.Y. Xu, H.P. Li, H.L. Liao. Role of ruthenium incorporation on room-temperature nonanal sensing properties of Ru-loaded urchin-like $W_{18}O_{49}$ hierarchical nanostructure. Sensors and Actuators B: Chemical, 353 (2022) 131096. https://doi.org/10.1016/j.snb.2021.131096.

[44] D. Meena, B. Singh, A. Anand, M. Singh, M.C. Bhatnagar. Phase dependent selectivity shifting behavior of Cd_2SnO_4 nanoparticles based gas sensor towards volatile organic compounds (VOC) at low operating temperature. Journal of Alloys and Compounds, 820 (2020) 153117. https://doi.org/10.1016/j.jallcom.2019.153117.

[45] J.Y. Jeon, S.J. Park, T.J. Ha. Functionalization of zinc oxide nanoflowers with palladium nanoparticles via microwave absorption for room temperature-operating hydrogen gas sensors in the ppb level. ACS Applied Materials & Interfaces, 13 (2021) 25082-25091. https://doi.org/10.1021/acsami.1c03283.

[46] B.X. Feng, Y.Y. Feng, Y.X. Li, Y.Q. Su, Y.H. Deng, J. Wei. Synthesis of mesoporous Ag_2O/SnO_2 nanospheres for selective sensing of formaldehyde at a low working temperature. ACS Sensors, 7 (2022) 3963-3972. https://doi.org/10.1021/acssensors.2c02232.

[47] X.Q. Hu, L. Lu, Z.L. Guo, Z.W. Zhu. Volatile compounds, affecting factors and evaluation methods for rice aroma: A review. Trends in Food Science & Technology, 97 (2020) 136-146. https://doi.org/10.1016/j.tifs.2020.01.003.

Conclusions and Perspectives

Conclusions

To effectively solve bottlenecks such as high working temperature, insufficient detection limit, and low selectivity of E-nose, this thesis conducts in-depth research on the development of metal oxide-based gas sensors for the detection of biomarkers in rice aging. The following conclusions can be drawn.

(1) Non-stoichiometric $W_{18}O_{49}$ hierarchical nanostructures are synthesized through a simple hydrothermal method utilizing WCl_6 as the tungsten source and methanol as the solvent. Then noble metal (Ru) is incorporated to improve the gas-sensing performance of $W_{18}O_{49}$ in the analysis of aldehydes. Accordingly, pure and 0.5-2.0%Ru-loaded urchin-like $W_{18}O_{49}$-based gas-sensing materials are obtained through the calcination under an inert atmosphere (N_2). The experimental results suggest that the 1.0%Ru-loaded $W_{18}O_{49}$ exhibits excellent gas-sensing performance towards ppm-level nonanal, one of the medium-chain aldehydes derived from oxidation and hydrolysis of lipids in rice aging. The enhanced gas-sensing properties of 1.0%Ru-loaded $W_{18}O_{49}$ can be derived from (I) the urchin-like morphology provides large specific surface area (94.2 m^2/g), facilitating the adsorption of nonanal molecules; (II) sub-stoichiometric $W_{18}O_{49}$ possesses highly concentrated oxygen vacancies, enhancing oxygen adsorption and increasing the oxygen species available for reacting with nonanal; (III) incorporating an appropriate amount of Ru into $W_{18}O_{49}$ effectively inhibits grain growth and improves the catalytic oxidation of both Ru^{3+} and Ru^{4+}, contributing to an increase in specific surface area, the relative proportions of chemisorbed oxygen and oxygen vacancy components. Furthermore, practical experiments suggest that the fabricated sensor has the capability to distinguish indica rice from japonica rice. Consequently, the incorporation of Ru into non-stoichiometric $W_{18}O_{49}$ holds promise as a strategy for developing a high-performance E-nose system for inspecting rice quality during storage.

(2) Oxygen engineering on CeO_2 nanowires is developed through a simple hydrothermal method, utilizing $CeCl_3 \cdot 7H_2O$ as the cerium source and deionized water as the solvent, combined with calcination under different controlled atmospheres (air, Ar, and 5%H_2+95%Ar). The sample annealed under 5%H_2+95%Ar atmospheres (S3) exhibits outstanding gas-sensing properties towards ppm-level linalool, one of the alcohols generated via the further breakdown of aldehydes. The enhanced gas-sensing performance of the S3-based gas sensor can be ascribed to (I) the nanowire morphology with a high surface-to-volume ratio facilitates the transmission and diffusion of linalool;

(II) S3 displays a larger specific surface area of 83.9 m^2/g, providing adequate adsorption sites for linalool; (III) an increase in the relative concentrations of chemisorbed oxygen and oxygen vacancy components is accompanied by an increase of Ce^{3+} ions through annealing under the atmosphere (5%H_2+95%Ar) with strong reducibility, increasing the oxygen species available for reacting with linalool. In addition, practical experiments manifest that the S3-based gas sensor can distinguish indica rice from japonica rice, and monitor changes in rice quality during storage. Hence, the regulation of the electronic structures and surface chemical states in CeO_2 nanowires holds tremendous potential for the development of high-performance room-temperature E-nose equipment for large-scale inspections of rice quality during aging.

(3) Nanoscale ZnO/$ZnSnO_3$ heterojunctions with dual-mesoporous structures and varying concentrations of oxygen vacancies are directly manufactured by solution precursor plasma spray (SPPS). These heterojunctions are engineered to create high-performance and energy-efficient gas-sensing devices employed to detect the characteristic biomarkers in rice aging. Crystal structure characterization confirms the formation of n-n heterojunctions at the interfaces between ZnO and $ZnSnO_3$ during the spraying, utilizing the corresponding precursors with a molar ratio of 1:1. The microstructures of the gas-sensing coatings are rationally designed by controlling the key parameter (hydrogen flow). Notably, the sensor fabricated with a low hydrogen flow (1 and 3 L/min) exhibits a dual-mesoporous structure, while the sample fabricated with a hydrogen flow of 5 L/min (H5) displays a higher concentration of oxygen vacancies. When employed as a gas sensor, H3 demonstrates superior room-temperature gas-sensing properties towards 2-undecanone, one of the ketones derived from the oxidative degradation of unsaturated fatty acids in rice aging. The enhanced gas-sensing performance of the H3-based gas sensor can be attributed to its unique dual-mesoporous structures and high relative proportion of oxygen vacancies, as confirmed by SEM and XPS analysis. Furthermore, for potential application exploitation, the H3-based gas sensor was applied to analyze volatile compounds generated from rice aging. The gas sensor can be utilized as one of the detection units of the E-nose to distinguish japonica rice from indica rice. Accordingly, heterostructured ZnO/$ZnSnO_3$ nanostructures directly fabricated by SPPS hold promise for the development of a high-performance E-nose for evaluating the rice quality during storage.

Perspectives

In this thesis, due to limitations in my ability and scope of knowledge, there are still some limitations in the research and development of high-performance metal oxide-based gas sensors for the detection of biomarkers in rice aging. In perspective, several potential ideas can be highlighted based on this thesis for improving future research, which are listed below.

(1) The room-temperature gas-sensing mechanisms of metal oxides need to be further investigated. Currently, the gas-sensing mechanisms proposed in this thesis are mainly based on the relevant literature, and I infer that the interaction between target gas and metal oxides is dehydrogenation. In the future, a comprehensive approach involving advanced characterization techniques (i.e., gas chromatography), density functional theory calculations, and molecular dynamics simulations should be employed for a thorough validation of the gas-sensing mechanisms in metal oxide-based gas sensors operating at room temperature

(2) The gas-sensing performance of the developed gas sensors should be thoroughly validated under multiple environmental conditions. In practical scenarios, testing environments are notably more intricate than laboratory settings. Therefore, in the future, emphasis should be placed on investigating the influence of external environmental factors on the gas-sensing properties of the developed gas sensors, in preparation for the subsequent development of a rice quality inspection system.

(3) The number of metal oxide-based gas sensors needs to be further increased. Presently, the detection system only includes three sets of gas sensors, and there are more than 300 types of VOCs in rice aging, posing challenges to ensure adequate cross-selectivity of the sensors. Consequently, novel equipment, such as vacuum plasma spray, magnetron sputtering and so on, should be applied to fabricate metal oxide-based thin films for biomarker detection.

(4) The repeatability of the sensors requires further validation. Typically stored at room temperature for six months to a year, or at high temperatures for one to three months, rice undergoes an aging process that leads to a deterioration in its quality. In this thesis, the sensor’s repeatability investigation lasts for only 30 days. Accordingly, the duration of the long-term stability investigation should be significantly extended.

List of Publications

[1] **J.Y. Xu**, K.C. Xu, X.X. He, et al. Interface engineering of $ZnSnO_3$-based heterojunctions for room-temperature methanol monitoring. Rare Metals, 42 (2023) 4153-4166.

[2] **J.Y. Xu**, X.X. He, K.C. Xu, et al. Synthesis and optimization strategies of nanostructured metal oxides for chemiresistive methanol sensors. Ceramics International, 49 (2023) 21113-21132.

[3] **J.Y. Xu**, H.L. Liao, C. Zhang. $ZnSnO_3$ based gas sensors for pyridine volatile marker detection in rice aging during storage. Food Chemistry, 408 (2023) 135204.

[4] **J.Y. Xu**, C. Zhang. Oxygen vacancy engineering on cerium oxide nanowires for room-temperature linalool detection in rice aging. Journal of Advanced Ceramics, 11 (2022) 1559-1570.

[5] **J.Y. Xu**, K.W. Liu, C. Zhang. Electronic nose for volatile organic compounds analysis in rice aging. Trends in Food Science & Technology, 109 (2021) 83-93.

[6] C. Zhang, **J.Y. Xu**, H.P. Li, et al. Role of ruthenium incorporation on room-temperature nonanal sensing properties of Ru-loaded urchin-like $W_{18}O_{49}$ hierarchical nanostructure. Sensors and Actuators B: Chemical, 353 (2022) 131096.

[7] K.D. Wu, **J.Y. Xu**, M. Debliquy, et al. Synthesis and NH_3/TMA sensing properties of $CuFe_2O_4$ hollow microspheres at low working temperature. Rare Metals, 40 (2021) 1768-1777.

[8] S. Ma, **J.Y. Xu**. Nanostructured metal oxide heterojunctions for chemiresistive gas sensors. Journal of Materials Chemistry A, 11 (2023) 23742-23771.

[9] K.C. Xu, M.J. Han, **J.Y. Xu**, et al. Highly sensitive $LaFeO_3$ coatings deposited by solution precursor plasma spraying for isoamyl alcohol detection. Journal of Thermal Spray Technology, 2024.

[10] K.W. Liu, Z.C. Zheng, **J.Y. Xu**, et al. Enhanced visible light-excited $ZnSnO_3$ for room temperature ppm-level CO_2 detection. Journal of Alloys and Compounds, 907 (2022) 164440.

[11] K.W. Liu, C. Zhang, **J.Y. Xu**, et al. Research advance in gas detection of volatile organic compounds released in rice quality deterioration process. Comprehensive Reviews in Food Science and Food Safety, 20 (2021) 5802-5828.

Title: Development of metal oxide-based gas sensors for the detection of biomarkers in rice aging

Keywords: metal oxides; gas sensors; oxygen vacancies; biomarkers; rice aging

Abstract: This study aims to develop high-performance metal oxide-based gas sensors for room-temperature detection of biomarkers in rice aging by incorporating oxygen vacancies. Three metal oxides, namely $W_{18}O_{49}$, CeO_{2-x}, and $ZnO/ZnSnO_3$ are successfully fabricated through strategies that combined a simple hydrothermal method with different surface modifications including noble metal loading and structural regulation. The morphologies and phase compositions of the obtained metal oxides are investigated using a field emission-scanning electron microscope (FE-SEM), X-ray diffraction (XRD), high-resolution transmission electron microscopy (HRTEM), and X-ray photoelectron spectroscope (XPS). The room-temperature gas-sensing performance, including response, response/recovery time, selectivity, and stability, of these metal oxides in detecting biomarkers in rice aging, is comprehensively investigated to explore the influence of Ru loading, post-treatment, and hydrogen flow on the enhanced gas-sensing properties, represented by the reduction of working temperature and the improvement of response. The room-temperature gas-sensing mechanism in the analysis of the characteristic biomarker is proposed. Furthermore, the practicability of the developed gas sensors is verified by two varieties of rice (japonica rice and indica rice).

Material characterizations reveal that metal oxides with different morphologies and structures are successfully prepared by the hydrothermal and solution precursor plasma spray (SPPS) methods. Their microstructure evolutions are precisely manipulated by Ru incorporation, annealing under different atmospheres, and adjusting the flow of hydrogen, respectively. The gas-sensing performance investigations exhibit that the obtained metal oxides display excellent room-temperature gas-sensing properties, including high response, rapid response/recovery time, and low detection limit, towards the characteristic biomarkers such as nonanal, linalool, and 2-undecanone. The enhanced room-temperature gas-sensing performance is chiefly due to the synergistic effects of their unique structures, and the incorporation of oxygen vacancies. In addition, the experimental results show that Ru-loaded $W_{18}O_{49}$ and CeO_{2-x} annealed under the atmosphere ($5\%H_2+95\%Ar$) may be able to distinguish indica rice from japonica rice. Conversely, reversal conducting behaviors can be observed when $ZnO/ZnSnO_3$ fabricated with the hydrogen flow of 3 L/min is exposed to two varieties of rice. Most importantly, SPPS stands out in solving the limitations, such as slow particle growth and insufficient oxygen vacancies in crystals, which exist in the above-stated methods (noble metal loading and post-treatment). Because of its intrinsic characteristics, SPPS can effectively incorporate highly concentrated oxygen vacancies into metal oxides and also construct heterostructures due to the different volatilization rates of metal sources, especially in the fabrication of ternary metal oxides, collectively enhancing the gas-sensing properties of metal oxides.

Titre : Développement de capteur de gaz à base d'oxydes métalliques pour la détection de biomarqueurs de vieillissement du riz

Mots clés: Oxydes métalliques; Capteur de gaz; Espace vide d'oxygène; Biomarqueurs; Vieillissement du riz

Résumé: Cette étude vise à développer des capteurs de gaz à base d'oxydes métalliques en incorporant des lacunes d'oxygène de haute performance pour la détection à température ambiante des biomarqueurs du vieillissement du riz. Trois oxydes métalliques ayant des défauts structuraux tels que $W_{18}O_{49}$, CeO_{2-x} et $ZnO/ZnSnO_3$ ont été préparés avec succès grâce à une stratégie combinant une méthode hydrothermale simple avec différentes modifications de surface, y compris le dopage avec métaux précieux et le conditionnement structurel. La topographie et la composition de phase des oxydes métalliques obtenus ont été étudiées à l'aide de la microscopie électronique à balayage par émission de champ (FE-SEM), de la Diffraction des rayons X (DRX), de la microscopie électronique à transmission à haute résolution (HRTEM) et du spectromètre photo-électronique à rayons X (XPS). Les performances de détection des gaz à température ambiante, notamment la sensibilité, le temps de réponse/récupération, la sélectivité et la stabilité de ces oxydes métalliques dans la détection des biomarqueurs générés lors du vieillissement du riz, ont été étudiées profondément afin d'explorer l'influence du dopage en Ru, du post-traitement et du débit d'hydrogène sur les propriétés de détection de gaz, se traduisant par la réduction de la température de fonctionnement et l'amélioration de la sensibilité.

La caractérisation des matériaus a montré que des oxydes métalliques de morphologie et de structure différentes ont été préparés avec succès par hydrothermie et projection plasma de solution de précurseurs (SPPS). Leur évolution microstructurale est contrôlée avec précision respectivement par l'incorporation de Ru, le recuit sous différentes atmosphères et la régulation du débit d'hydrogène. L'étude des performances de détection de gaz a montré que les oxydes métalliques obtenus présentaient d'excellentes propriétés de détection de gaz à température ambiante pour des biomarqueurs caractéristiques tels que le nonaldéhyde, le Linalol et la 2-undécanone, incluant une sensibilité élevée, des temps de réponse/récupération rapides et une faible limite de détection. L'amélioration des propriétés de détection de gaz à température ambiante est principalement due à l'effet synergique de leur structure unique et à l'incorporation de défauts, y compris les lacunes en oxygène et les défauts cristallins. De plus, les résultats expérimentaux montrent que le recuit atmosphérique ($5\%H_2+95\%Ar$) du $W_{18}O_{49}$ et du CeO_2 dopé en Ru permet de différencier le riz Indica du riz Japonic. Alors que $ZnO/ZnSnO_3$, préparé avec un débit d'hydrogène de 3 L/min, est exposé aux deux variétés de riz, un comportement de conductivité inverse est observé. Plus important encore, la projection plasma de solution de précurseur (SPPS) se démarque en résolvant les limitations, telles que la croissance lente des particules et l'insuffisance des défauts dans le cristallin, qui existaient

dans les méthodes mentionnées ci-dessus (dopage de métaux nobles et post-traitement). Grâce à ses propriétés intrinsèques, le SPPS permet d'introduire efficacement des défauts très concentrés dans les oxydes métalliques, mais aussi de construire des hétérostructures grâce aux différents taux de volatilisation des sources métalliques, en particulier dans la fabrication d'oxydes métalliques ternaires, renforçant conjointement les propriétés de détection de gaz des oxydes métalliques.